

VIABILITY OF ACCELERATED SPIN ECHO SINGLE POINT
IMAGING FOR LIPID COMPOSITION MAPPING IN FATTY
LIVER DISEASE

by

Miriam Hewlett

Submitted in partial fulfillment of the requirements
for the degree of Master of Science

at

Dalhousie University
Halifax, Nova Scotia
August 2019

© Copyright by Miriam Hewlett, 2019

Table of Contents

List of Tables	iv
List of Figures	vii
Abstract	xi
List of Abbreviations and Symbols Used	xii
Acknowledgements	xv
Chapter 1 Introduction	1
1.1 Non-Alcoholic Fatty Liver Disease	1
1.2 Non-Invasive Diagnostics in NAFLD	2
1.2.1 Fat Composition in NAFLD	3
1.3 Lipid Composition Mapping in Fatty Liver Disease	5
1.4 Research Question and Hypotheses	6
Chapter 2 Background	8
2.1 Nuclear Magnetic Resonance	8
2.2 Spatial Encoding	13
2.2.1 Slice Selection	14
2.2.2 Phase and Frequency Encoding	15
2.3 Magnetic Resonance Spectroscopy	18
2.3.1 Magnetic Resonance Spectroscopic Imaging	22
2.4 K-space Undersampling for Accelerated MR Acquisition	24
2.4.1 Compressed Sensing	25
2.5 Hankel Singular Value Decomposition (HSVD)	30
Chapter 3 Acquisition and Processing Pipeline	32
3.1 Undersampling Pattern Generation	32
3.2 Respiratory Motion Correction	33
3.3 Spectral Processing	35

3.4	Methods	38
3.4.1	Phantom Design and Acquisition	38
3.4.2	Choice of Parameters: Spectral Analysis	40
3.4.3	Choice of Coil Combination Weightings	41
3.4.4	Choice of Parameters: Compressed Sensing Reconstruction	42
3.5	Results	44
3.5.1	Choice of Parameters: Spectral Analysis	44
3.5.2	Choice of Coil Combination Weightings	45
3.5.3	Choice of Parameters: Compressed Sensing	46
3.6	Discussion	58
3.6.1	Choice of Parameters: Spectral Analysis	58
3.6.2	Choice of Parameters: Compressed Sensing Reconstruction	59
Chapter 4	Phantom Validation	61
4.1	Methods	61
4.2	Results	62
4.3	Discussion	77
Chapter 5	<i>In vivo</i> Mouse Evaluation	82
5.1	Methods	82
5.1.1	Experimental Design	82
5.1.2	Lipid Composition Analysis	83
5.2	Results	85
5.3	Discussion	90
Chapter 6	Conclusions and Future Directions	94
Appendix A	Derivations	97
A.1	Fat Fraction Correction for TR (Equation 5.1)	97
Bibliography	98

List of Tables

Table 2.1	Gyromagnetic ratios, γ (MHz/T), for ^1H , ^{13}C , ^{19}F , ^{23}Na , and ^{31}P .	9
Table 2.2	Summary of fatty acid functional groups.	20
Table 3.1	Bins used in separating the fatty acid functional groups for phantom experiments.	37
Table 3.2	Summary of coil combination weightings investigated for clinical experiments.	41
Table 3.3	BCS parameters investigated, namely the numbers of iterations, n_{iter} , numbers of basis functions, r , regularization parameters, λ , and scaling factors, s	42
Table 3.4	BCS parameters, namely the number of iterations, n_{iter} , number of basis functions, r , regularization parameter, λ , and scaling factor, s , which minimized the MSE in relative fat peak amplitudes between the fully sampled preclinical 3D dataset and that retrospectively accelerated by a factor of $R = 5.5$	53
Table 4.1	Preclinical results of Welch’s t-test comparing the unsaturation indices (UI) of the various pure oil tubes, as measured using PRESS.	68
Table 4.2	Preclinical results of Welch’s t-test comparing the unsaturation indices (UI) of the various pure oil tubes, as measured using fully sampled SE-SPI.	68
Table 4.3	Preclinical results of Welch’s t-test comparing the unsaturation indices (UI) of the various pure oil tubes, as measured using retrospectively accelerated ($R = 5.5$) CS SE-SPI.	69
Table 4.4	Preclinical results of Welch’s t-test comparing the surrogate unsaturation indices (UIs) of the various pure oil tubes, as measured using PRESS.	69
Table 4.5	Preclinical results of Welch’s t-test comparing the surrogate unsaturation indices (UIs) of the various pure oil tubes, as measured using fully sampled SE-SPI.	69

Table 4.6	Preclinical results of Welch’s t-test comparing the surrogate unsaturation indices (UIs) of the various pure oil tubes, as measured using retrospectively accelerated ($R = 5.5$) CS SE-SPI.	70
Table 4.7	Preclinical results of Welch’s t-test comparing the polyunsaturation indices (PUI) of the various pure oil tubes, as measured using PRESS.	70
Table 4.8	Preclinical results of Welch’s t-test comparing the polyunsaturation indices (PUI) of the various pure oil tubes, as measured using fully sampled SE-SPI.	70
Table 4.9	Preclinical results of Welch’s t-test comparing the polyunsaturation indices (PUI) of the various pure oil tubes, as measured using retrospectively undersampled ($R = 5.5$) CS SE-SPI.	71
Table 4.10	Clinical results of Welch’s t-test comparing the unsaturation indices (UI) of the various pure oil tubes, as measured using PRESS.	74
Table 4.11	Clinical results of Welch’s t-test comparing the unsaturation indices (UI) of the various pure oil tubes, as measured using fully sampled SE-SPI.	74
Table 4.12	Clinical results of Welch’s t-test comparing the unsaturation indices (UI) of the various pure oil tubes, as measured using retrospectively accelerated ($R = 3$) CS SE-SPI.	75
Table 4.13	Clinical results of Welch’s t-test comparing the surrogate unsaturation indices (UIs) of the various pure oil tubes, as measured using PRESS.	75
Table 4.14	Clinical results of Welch’s t-test comparing the surrogate unsaturation indices (UIs) of the various pure oil tubes, as measured using fully sampled SE-SPI.	75
Table 4.15	Clinical results of Welch’s t-test comparing the surrogate unsaturation indices (UIs) of the various pure oil tubes, as measured using retrospectively accelerated ($R = 3$) CS SE-SPI.	76
Table 4.16	Clinical results of Welch’s t-test comparing the polyunsaturation indices (PUI) of the various pure oil tubes, as measured using PRESS.	76
Table 4.17	Clinical results of Welch’s t-test comparing the polyunsaturation indices (PUI) of the various pure oil tubes, as measured using fully sampled SE-SPI.	76

Table 4.18	Clinical results of Welch's t-test comparing the polyunsaturation indices (PUI) of the various pure oil tubes, as measured using retrospectively undersampled ($R = 3$) CS SE-SPI.	77
Table 5.1	Bins used in separating the fatty acid functional groups for pre-clinical mouse experiments.	83

List of Figures

Figure 2.1	Energy level diagram for a spin-1/2 particle in a uniform magnetic field.	8
Figure 2.2	Precession of the net magnetization vector, \vec{M} , about the longitudinal direction.	10
Figure 2.3	Real and imaginary components of the free induction decay.	11
Figure 2.4	Pulse sequence diagram for a simple spin echo sequence.	13
Figure 2.5	Pulse sequence diagram with axial slice selection for a spin echo sequence.	14
Figure 2.6	Phase encoding in 1D.	15
Figure 2.7	Pulse sequence diagram for a 2D phase encoded spin echo imaging sequence.	16
Figure 2.8	Reconstruction of a 2D image acquired with phase encoding.	17
Figure 2.9	K-space datasets (log-scaled to show detail in the periphery) along with their corresponding images.	18
Figure 2.10	FID produced by a sample containing both fat and water along with the spectrum resulting from the Fourier transform of this FID.	19
Figure 2.11	Pulse sequence diagram for a point resolved spectroscopy (PRESS) sequence.	22
Figure 2.12	K-space datasets (log-scaled to show detail in the periphery) along with their corresponding images.	25
Figure 2.13	Diagram demonstrating how a sparse signal can be reconstructed from randomly undersampled data.	27
Figure 2.14	K-space datasets (log-scaled to show detail in the periphery) along with their corresponding images.	28
Figure 3.1	(A) Square shells used for the 2D CIRCUS implementation. (B) Spherical shells (slice $Z = 8$) used for the 3D CIRCUS implementation. (C) 2D undersampling pattern ($R = 3$). (D) 3D undersampling pattern ($R = 5.5$, slice $Z = 8$).	32

Figure 3.2	(A) SE-SPI sequence diagram with navigators for retrospective motion correction. (B) Comparison of respiratory traces as measured using respiratory bellows and navigators in mice. Red points indicate navigator signals larger than one standard deviation of the average; such points were omitted prior to reconstruction.	34
Figure 3.3	Undersampling patterns generated with the modified CIRCUS algorithm.	34
Figure 3.4	Flowchart summarizing the identification of the water resonance.	35
Figure 3.5	Processing of a PRESS spectrum for a 20% soybean oil tube. .	36
Figure 3.6	Diagram demonstrating the calculation of MSE used in order to assess the quality of BCS reconstructions with varying reconstruction parameters.	43
Figure 3.7	Squared differences between fat peak amplitudes measured by each preclinical PRESS pair as a function of assumed spectral components, N	44
Figure 3.8	Squared differences between fat peak amplitudes measured by each clinical PRESS pair as a function of assumed spectral components, N	45
Figure 3.9	Unsaturation (UI), surrogate unsaturation (UIs), and polyunsaturation (PUI) indices as measured using CS SE-SPI on the clinical system with the single and multichannel head coils. . .	46
Figure 3.10	Fully sampled preclinical 3D SE-SPI of the soybean oil phantoms used to investigate the impact of changing BCS reconstruction parameters on fat composition quantification.	48
Figure 3.11	Maps of relative peak amplitudes from the fully sampled preclinical 3D SE-SPI (top row), as well as those calculated from retrospectively accelerated scans ($R = 5.5$) with varying numbers of iterations.	49
Figure 3.12	Maps of relative peak amplitudes from the fully sampled preclinical 3D SE-SPI (top row), as well as those calculated from retrospectively accelerated scans ($R = 5.5$) with varying numbers of basis functions.	50
Figure 3.13	Maps of relative peak amplitudes from the fully sampled preclinical 3D SE-SPI (top row), as well as those calculated from retrospectively accelerated scans ($R = 5.5$) with varying regularization parameters.	51

Figure 3.14	Maps (slice $Z = 12$) of relative peak amplitudes from the fully sampled preclinical 3D SE-SPI (top row), as well as those calculated from retrospectively accelerated scans ($R = 5.5$) with varying scaling factors.	52
Figure 3.15	Maps of relative peak amplitudes in the safflower tube from the fully sampled clinical 2D SE-SPI (top row), as well as those calculated from retrospectively accelerated scans ($R = 3$) with varying numbers of iterations.	54
Figure 3.16	Maps of relative peak amplitudes in the safflower tube from the fully sampled clinical 2D SE-SPI (top row), as well as those calculated from retrospectively accelerated scans ($R = 3$) with varying numbers of basis functions.	55
Figure 3.17	Maps of relative peak amplitudes in the safflower tube from the fully sampled clinical 2D SE-SPI (top row), as well as those calculated from retrospectively accelerated scans ($R = 3$) with varying regularization parameters.	56
Figure 3.18	Maps of relative peak amplitudes in the safflower tube from the fully sampled clinical 2D SE-SPI (top row), as well as those calculated from retrospectively accelerated scans ($R = 3$) with varying scaling factors.	57
Figure 4.1	Fat fractions (mean \pm 95% CI over five scans) for the 5%, 10%, 15%, 20%, and 100% soybean oil tubes as measured using PRESS, fully sampled SE-SPI, and retrospectively accelerated ($R = 5.5$) CS SE-SPI on the preclinical system.	62
Figure 4.2	100% soybean spectra along with relative peak amplitudes for the five soybean oil tubes of varying fat fraction, as measured with the preclinical system.	64
Figure 4.3	Unsaturation (UI), surrogate unsaturation (UIs), and polyunsaturation (PUI) indices for the soybean oil tubes of varying fat fraction, as measured with the preclinical system.	65
Figure 4.4	Unsaturation (UI), surrogate unsaturation (UIs), and polyunsaturation (PUI) indices of the pure oil tubes, as measured using the preclinical scanner.	66
Figure 4.5	100% soybean spectra along with relative peak amplitudes for the five pure oil tubes, as measured with the preclinical scanner.	67
Figure 4.6	100% soybean spectra along with relative peak amplitudes for the five pure oil tubes, as measured with the clinical scanner.	72

Figure 4.7	Unsaturations (UI), surrogate unsaturations (UIs), and polyunsaturations (PUI) indices of the pure oil tubes, as measured using the clinical scanner.	73
Figure 4.8	Comparison of unsaturations (UI), surrogate unsaturations (UIs), and polyunsaturations (PUI) indices obtained with the clinical and preclinical scanners.	81
Figure 5.1	Sagittal slice of the bSSFP anatomical. The larger white outline indicates the SE-SPI volume, and the smaller outline the PRESS voxel. The liver contour is shown in red. Shown in green is the ROI used for SE-SPI analysis; i.e. liver tissue having adequate SE-SPI signal intensity.	84
Figure 5.2	Fat fraction results from the <i>in vivo</i> mouse study.	85
Figure 5.3	Unsaturations (UI), surrogate unsaturations (UIs), and polyunsaturations (PUI) indices as calculated from <i>in vivo</i> PRESS spectra.	86
Figure 5.4	Unsaturations (UI), surrogate unsaturations (UIs), and polyunsaturations (PUI) indices as calculated from <i>ex vivo</i> PRESS spectra.	87
Figure 5.5	Raw spectra, shown for <i>in vivo</i> PRESS, <i>ex vivo</i> PRESS, and CS SE-SPI, alongside anatomical images with liver outlined in red.	88
Figure 5.6	Unsaturations (UI), surrogate unsaturations (UIs), and polyunsaturations (PUI) indices as calculated from <i>in vivo</i> CS SE-SPI	89
Figure 5.7	Maps of fat fraction (<i>TR</i> corrected) and surrogate unsaturation index (UIs) for an MCD mouse.	90
Figure 5.8	Raw spectra for a single <i>in vivo</i> CS SE-SPI voxel, as well as those averaged over 3x3x3 and 10x10x10 sub-volumes. An <i>ex vivo</i> PRESS spectrum is also shown for comparison.	91

Abstract

Lipid composition may have the potential to predict disease progression in non-alcoholic fatty liver disease (NAFLD). Magnetic resonance spectroscopy (MRS) studies can provide this lipid composition information but single voxel techniques have limited spatial coverage. Spectroscopic imaging techniques provide improved spatial coverage, but are inherently slow. This thesis uses spin echo single point imaging (SE-SPI), accelerated with compressed sensing (CS), for lipid composition mapping. Oil phantom studies using preclinical and clinical systems showed similar trends in lipid composition when comparing CS SE-SPI to conventional MRS, although clinical SE-SPI scans showed increased variability in lipid composition measurements. In a mouse model of NAFLD, CS SE-SPI showed changes in lipid composition in agreement with literature results. This work demonstrates the viability of CS SE-SPI in measuring lipid composition. Future implementation of CS SE-SPI in clinical cases will permit a more thorough investigation of lipid composition as a biomarker of NAFLD progression.

List of Abbreviations and Symbols Used

BW	BandWidth
FOV	Field Of View
G	Magnetic field gradient
M_0	Equilibrium magnetization
M_z	Longitudinal component of net magnetization
TE	Echo Time
TR	Repetition Time
T_1	Longitudinal relaxation time
T_2	Transverse relaxation time
T_2^*	Observed transverse relaxation time
α	Flip angle
γ	Gyromagnetic ratio
λ	Regularization parameter weighting sparsity versus data consistency in CS reconstruction
ν_L	Larmor frequency
\vec{B}_0	Homogeneous magnetic field defining the longitudinal axis
\vec{M}	Bulk magnetization vector
a_i	Relative amplitudes of different frequency components in an MRS signal
n_{iter}	Number of iterations used for BCS reconstruction
r	Number of temporal basis functions used for BCS reconstruction
s	Scaling factor applied to undersampled k-space data prior to BCS reconstruction
BCS	Blind Compressed Sensing
bSSFP	Balanced Steady-State Free Precession
CIRCUS	CIRcular Cartesian UnderSampling

CNN	Convolutional Neural Network
CS	Compressed Sensing
EPI	Echo-Planar Imaging
EPSI	Echo-Planar Spectroscopic Imaging
FID	Free Induction Decay
FSE	Fast Spin Echo
GRAPPA	GeneRALized Autocalibrating Partial Parallel Acquisition
HSVD	Hankel Singular Value Decomposition
MCD	Methionine Choline Deficient
MR	Magnetic Resonance
MRE	Magnetic Resonance Elastography
MRI	Magnetic Resonance Imaging
MRS	Magnetic Resonance Spectroscopy
MRSI	Magnetic Resonance Spectroscopic Imaging
MSE	Mean Squared Error
MUFAs	MonoUnsaturated Fatty Acids
NAFLD	Non-Alcoholic Fatty Liver Disease
NASH	Non-Alcoholic SteatoHepatitis
NMR	Nuclear Magnetic Resonance
PDFF	Proton Density Fat Fraction
PRESS	Point RESolved Spectroscopy
PSF	Point Spread Function

PUFAs	PolyUnsaturated Fatty Acids
PUI	PolyUnsaturation Index
RF	RadioFrequency
ROI	Region of Interest
SE-SPI	Spin Echo Single Point Imaging
SENSE	SENSitivity Encoding
SFAs	Saturated Fatty Acids
SNR	Signal to Noise Ratio
SPIO	SuperParamagnetic Iron Oxide
SVS	Single Voxel Spectroscopy
TSI	Turbo Spectroscopic Imaging
UFAs	Unsaturated Fatty Acids
UI	Unsaturation Index
UIs	Surrogate Unsaturation Index

Acknowledgements

To begin, I'd like to thank my supervisors, Steven Beyea and James Rioux. I really appreciate the time you spent discussing all of my questions, and I am very grateful for your guidance over the past two years.

I'd also like to thank my committee members Kim Brewer and Sharon Clarke, along with many others at BIOTIC, for their valuable feedback and interest in this work; a particular thanks to Dave McAllindon and Christa Davis for their contributions to the project.

Thanks to my friends and classmates Mary, Jenny, Allister, Anna, Matthew, and others in the Medical Physics program, who really made these past two years a positive experience.

Lastly, thank you to my friends and family, for always supporting me.

Chapter 1

Introduction

1.1 Non-Alcoholic Fatty Liver Disease

Non-alcoholic fatty liver disease (NAFLD), characterized by elevated levels of fat in the liver,¹ known as steatosis, is a common health concern. While the prevalences of NAFLD and its further complications are not well defined due to variation in populations and diagnostic techniques, in developed countries it is estimated that 20-40% of the population have NAFLD, and it is expected that these numbers will rise with increasing rates of diabetes and obesity. Many patients with NAFLD are relatively unaffected by the disease. However, in 10% to 20% of cases NAFLD will progress to non-alcoholic steatohepatitis (NASH), characterized by inflammation and ballooning, or expansion, of the liver cells, the latter of which is associated with the accumulation of fat droplets in the cytoplasm, among other things [2]. A further subset of NASH patients will develop complications such as fibrosis and cirrhosis, leading to liver failure, and liver cancer [3, 4, 5, 6].

Notably, steatosis and inflammation are more easily reversed than fibrosis and further complications, typically treated with lifestyle changes or medication [1, 7]. Thus, early detection of disease is especially valuable, and knowing the extent of disease progression is important for clinical management [8]. However, the rate of progression varies among patients, and symptoms of liver damage often don't appear until later stages of the disease [9, 10]. Furthermore, the current gold standard for grading and staging of NASH and fibrosis is biopsy, which, being an invasive procedure, cannot be used for frequent follow up of at risk patients [1, 3, 4, 7]. A non-invasive diagnostic is preferred. Biopsy also suffers from limited spatial coverage, an important consideration as the accumulation of fat in the liver is not necessarily homogeneous. Liver tissue located near the central vein is more susceptible to steatosis than that located

¹Often defined as $> 5\%$ fat by weight, or accumulation of fat in $>5\%$ of liver cells [1], excluding those cases caused by excessive alcohol consumption.

at the periphery, particularly in early stages of disease progression. In later stages the distribution of fat in the liver is most often diffuse; however, heterogeneous cases do exist [11]. Additionally, heterogeneity in the inflammation and hepatocyte ballooning used for histological diagnosis of NASH is not uncommon. Grading and staging of NASH as determined from paired biopsy samples has been shown to disagree in approximately 40% of patients, a disagreement that cannot be entirely attributed to intraobserver variability [12].

1.2 Non-Invasive Diagnostics in NAFLD

Laboratory results, such as elevated levels of aspartate aminotransferase and/or alanine aminotransferase, may be used as indicators of NAFLD, but have poor specificity [1, 10]. Another option for non-invasive monitoring of disease progression is medical imaging. Steatosis, the initial accumulation of fat in the liver, is reliably detectable using magnetic resonance (MR) techniques such as MR spectroscopy (MRS) or MR fat fraction mapping, as well as ultrasound and, in some cases, CT. However, in most cases this steatosis is benign. Furthermore, earlier indicators of disease, including steatosis, inflammation, and ballooning, regress as fibrosis develops. Without some measure of fibrosis stage, fat fraction alone cannot be used to distinguish between early and later stages of disease [3, 9, 10]. Later stages of disease progression, such as advanced cirrhosis, may be diagnosed through combination of laboratory tests and imaging [13, 14]; however, at this point liver damage is much more difficult to treat.

The need for indicators of early NAFLD progression has led to an abundance of research using MR imaging (MRI), including perfusion and diffusion MRI [14, 15, 16, 17], to attempt a non-invasive grading and staging of NASH and fibrosis, with varying degrees of success. One technique shown to be relatively successful in this context is magnetic resonance elastography (MRE). MRE provides a non-invasive measurement of liver elasticity, or stiffness, which has been shown to increase with fibrosis stage, and has had some success distinguishing steatosis from NASH without fibrosis [8]. However, this measure of liver stiffness is not specific to NAFLD progression; other causes include acute inflammation and portal hypertension, as liver stiffness has also been associated with high blood pressure in the portal venous system [14, 18]. MRE scans may also be complicated by iron overload [19], which can occur in NAFLD [20],

although there are approaches attempting to overcome this issue [21]. Additionally, MRE requires specialized equipment that is not yet widely available [1]. Less accurate ultrasound elastography techniques can also be used to monitor fibrosis, but are limited by the depth of the tissue of interest, complicating liver stiffness measurements in obese patients [14].

1.2.1 Fat Composition in NAFLD

Perhaps more indicative of risk than fat fraction is the composition of the liver fat accumulated in NAFLD [22, 23, 24]. All fatty acids are composed of a carboxyl group and a hydrocarbon chain. For some of these fatty acids, the hydrocarbon chain consists solely of single bonds, denoted saturated fatty acids, or SFAs. Those fatty acids for which the hydrocarbon chain contains double bonds are referred to as unsaturated fatty acids, or UFAs. Furthermore, UFAs for which the hydrocarbon chain contains multiple double bonds are referred to as polyunsaturated fatty acids, or PUFAs, while those containing only one double bond are referred to as monounsaturated fatty acids, or MUFAs.

This fatty acid composition information, namely the relative amounts of SFAs, MUFAs, and PUFAs, in liver fat in NAFLD may have the potential to predict which patients are more at risk of developing NASH, before changes in liver stiffness, as can be observed by elastography, occur. It is hypothesized that a decrease in the relative concentration of PUFAs in the liver contributes to the development of NASH. More specifically, a decrease in omega-3 long chain PUFAs² appears to downregulate genes associated with the breakdown of fatty acids and upregulate genes associated with their synthesis, contributing to hepatic steatosis, with the secondary effect of inducing inflammation, together contributing to hepatic steatohepatitis [25, 26]. As such, much research has been done investigating these omega-3 PUFAs both as a treatment [27], and a biomarker of NAFLD. A study by Elizondo et al. using gas-liquid chromatography has shown liver fat in obese patients with NAFLD to have a higher concentration of SFAs and relatively fewer PUFAs, with no difference in MUFAs, as compared to a control group. This decrease in PUFAs corresponded to

²Omega-3 PUFAs are characterized by a double bond between the 3rd and 4th carbon atoms from the terminal methyl group in their hydrocarbon chain.

a decrease in omega-3 long chain PUFAs [22], as has also been observed in NASH patients when compared to a control group [25].

This fatty acid composition information can also be measured non-invasively, to an extent, using MRS techniques such as point resolved spectroscopy (PRESS). Hydrogen nuclei bonded to the carbon atoms forming double bonds present in UFAs will produce signal with slightly different frequency than those present in SFAs. The same may be said for hydrogen nuclei bonded to carbon atoms situated between two of these double bonds, as will occur in PUFAs. As such, the relative amplitudes of different frequency components of the signal can be used to measure the relative amounts of SFAs and PUFAs present, as quantified using unsaturation (UI) and polyunsaturation (PUI) indices, respectively (see Section 2.3 for more details). One study by Johnson et al. using these metrics, as well as a surrogate unsaturation index (UIs) in order to facilitate analysis in the presence of a water signal, has shown a similar increase in the relative amount of SFAs and decrease in that of PUFAs in obese patients with fatty livers as compared to controls. However, these metrics cannot distinguish contributions of omega-3 long chain PUFAs, as was the case for the above-mentioned gas-liquid chromatography studies. The trends in relative contribution of SFAs and PUFAs appeared consistent when comparing obese NAFLD patients to obese controls with normal liver fat content, but only the change in PUFAs was significant. Notably, differences in diet leading up to the MRS studies did not lead to significant differences in fatty acid composition measurements [23].

Changes in fatty acid composition can also be observed in animal models of NAFLD, often induced through a methionine and choline deficient (MCD) diet [28, 29, 30, 31]. This methionine choline deficiency leads to a sequestration of fat in the liver, as well as progressive liver injury that may accompany human NAFLD. Mice fed an MCD diet will develop NASH after 10 days, and fibrosis after about 10 weeks. However, the metabolic changes that occur with MCD diets are not representative of those which occur in human NAFLD; notably, mice on MCD diets undergo considerable weight loss [32]. While animal models of NAFLD are ideally designed to model the histological results of human NAFLD, including steatosis, inflammation, ballooning, etc., along with the accompanying metabolic changes, no such ideal model exists. Fundamental anatomical and physiological differences between humans and animals used to

model human disease will always be a limitation, and the complexity of NAFLD, along with our incomplete understanding of the disease, further complicates the design of such a model [33]. Nonetheless, these models are still very useful in studying disease, as long as the limitations are considered in the context of the research question at hand.

1.3 Lipid Composition Mapping in Fatty Liver Disease

As discussed above, lipid composition information has potential as a biomarker in NAFLD. MRS techniques can provide this lipid composition information non-invasively; however, like biopsy, these techniques provide poor spatial coverage, whereas accumulation of fat in the liver may be heterogeneous. On the other hand, magnetic resonance spectroscopic imaging (MRSI) techniques can provide this fatty acid composition information with improved spatial coverage, but are limited in terms of their clinical application by lengthy acquisition times. Spectroscopic imaging sequences based on turbo spectroscopic imaging (TSI) and echo-planar spectroscopic imaging (EPSI) techniques can be used to accelerate scans in some cases. However, the application of TSI is limited by quick signal decay inherent to the fatty acids of interest to this work [34], and EPSI is especially sensitive to magnetic field inhomogeneities, which may be exaggerated by the iron overload that can accompany NAFLD [35, 36]. As such, this work makes use of a simple single point imaging technique using spin echoes to reverse signal decay that may result from these high iron concentrations, denoted spin echo single point imaging, or SE-SPI. While single point imaging techniques are inherently slow, scans can be accelerated using compressed sensing (CS).

CS reduces scan times by undersampling the data. While this undersampling produces noise-like artefacts in the resulting images, this noise can be removed during the reconstruction process using a sparse representation³ of the data. Essentially, in this sparse representation the true signal can be more easily separated from the noise-like artefacts. As spectroscopic imaging techniques are often limited in terms of acquisition time, CS has been previously applied to a number of MRSI applications, including ^{13}C [37] and ^{19}F imaging [38]. Application of CS to ^1H metabolic imaging at 3T in the brain and prostate has shown that scan times can be reduced by as much

³A sparse representation will describe the signal with only a few non-zero values.

as 80% with no significant change in clinically relevant biomarkers [39].

1.4 Research Question and Hypotheses

Given the potential for lipid composition information as a biomarker of NAFLD, and that of SE-SPI in providing a more complete measure of this information compared to single voxel spectroscopy (SVS) techniques, this work addresses the following research question: Can SE-SPI, specifically that accelerated with compressed sensing, provide an accurate measure of lipid composition? This question is addressed by both oil phantom experiments and a mouse model of NAFLD, hypothesizing:

Hypothesis A: **In oil phantoms** Fat composition as measured using SE-SPI, fully sampled and accelerated, will show differences (significance determined using Welch’s t-test, $p < 0.05$ considered significant) in UI, UIs, and PUI for different oils in agreement with those found using PRESS.

Hypothesis B: **In mice** CS SE-SPI will allow *in vivo* measurement of lipid composition in a mouse model of NAFLD consistent with literature results, showing an increase in the relative concentration of SFAs in mice fed an MCD diet compared to controls [29].

The MCD diet used in this study has been shown to result in a higher concentration of SFAs with no significant change in the relative amount of MUFAs [29], implying a decrease in the relative amount of PUFAs. These trends do follow those observed in the human studies discussed in Section 1.2.1, although it should be noted that the degree of change in fatty acid composition will not necessarily follow that occurring in human NAFLD. In fact, changes in fatty acid composition are not always consistent between animal studies, likely in part due to differences in diet formulation which have been shown to affect fatty acid composition measurements [30].

While the degree of change in fatty acid composition, both in the phantoms and the *in vivo* model of NAFLD used for this work, may not accurately model those observed in human cases of NAFLD, such studies are still useful in assessing the potential of CS SE-SPI to monitor changes in fatty acid composition in comparison

to accepted techniques. For phantom studies, PRESS was chosen as the gold standard as opposed to theoretical or literature values since calculations in the latter case would require corrections for signal decay, dependant on the acquisition parameters and MR properties of the fatty acids. For the *in vivo* model of NAFLD, the poor quality of PRESS data prompted comparison with literature results.

Additional background information on the relevant MR theory and analysis techniques is given in Chapter 2. The acquisition and post processing pipeline, including choice of post processing parameters, is discussed in Chapter 3. The phantom and *in vivo* experiments addressing Hypotheses A and B are given in Sections 4 and 5, respectively. Conclusions and future directions are summarized in Chapter 6.

Chapter 2

Background

2.1 Nuclear Magnetic Resonance

Atomic nuclei possess an intrinsic quantum property known as spin, somewhat analogous to the classical concept of angular momentum. When nuclei with non-zero spin are exposed to a uniform magnetic field, B_0 , different spin states become separated by an energy gap as described by the Zeeman effect. At finite temperatures, spin-1/2 nuclei such as ^1H have two such states, orienting themselves such that their spins are either parallel or antiparallel to this magnetic field¹, as shown in Figure 2.1.

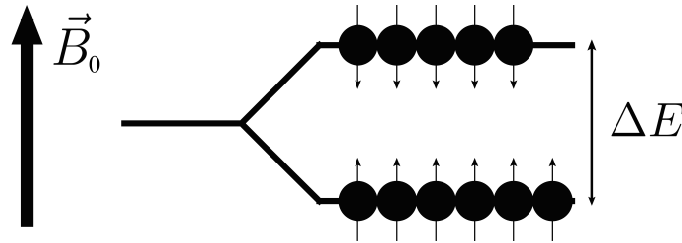


Figure 2.1: Energy level diagram for a spin-1/2 particle in a uniform magnetic field.

The energy separation between these two orientations is given by:

$$\Delta E = \gamma \hbar B_0 \quad (2.1)$$

where γ is the gyromagnetic ratio, given for some particular nuclei in Table 2.1, and \hbar the Planck constant. Thus, transitions between these two spin states will occur through absorption or emission of energy $\Delta E = \hbar\nu$, where:

$$\nu_L = \gamma B_0 \quad (2.2)$$

This frequency, ν_L , is known as the Larmor frequency [40]. For medical imaging applications, these frequencies are typically in the radiofrequency (RF) range.

¹This statement is not completely correct. In a true quantum mechanical description, the spin state of an atomic nucleus may very well be described as a superposition of the two energy states. However, any direct measurement will indicate either parallel or antiparallel orientation.

Table 2.1: Gyromagnetic ratios, γ (MHz/T), for ^1H , ^{13}C , ^{19}F , ^{23}Na , and ^{31}P .

Nucleus	γ (MHz/T)
^1H	42.58
^{13}C	10.71
^{19}F	40.05
^{23}Na	11.26
^{31}P	17.24

For a system at absolute zero, all nuclei would orient themselves in the lower energy state. However, due to the thermal energy present, there exists only a slight imbalance favouring this case. This slight excess, the source of signal in nuclear magnetic resonance (NMR) experiments, is given by the Boltzmann distribution:

$$\frac{N_{\text{parallel}}}{N_{\text{antiparallel}}} = \exp \left[\frac{\Delta E}{k_B T} \right] \quad (2.3)$$

where ΔE is the energy separation defined in Equation 2.1, k_B the Boltzmann constant, and T the temperature of the sample. For example, ^1H nuclei ($\gamma = 42.58$) at body temperature ($T = 37^\circ\text{C}$) in a 3T MRI will be distributed such that $N_{\text{parallel}}/N_{\text{antiparallel}} \approx 1.000003$. Although this excess represents a tiny fraction of nuclei, given the large number of hydrogen atoms in the human body their signal production can be described classically.²

A particle with non-zero spin will have an associated magnetic moment, μ , the net sum of which (for an ensemble of nuclei) is referred to as the bulk magnetization vector, \vec{M} . When exposed to a homogeneous field, B_0 , along the longitudinal axis, \vec{z} , spins will gradually orient themselves with slight preference for the low energy state as described in Equation 2.3, producing a net \vec{M} along the same direction as B_0 , denoted as the equilibrium magnetization, M_0 . If disturbed from this equilibrium position, the interaction between net magnetization and the homogeneous field will produce a torque causing \vec{M} to precess about the longitudinal axis with angular frequency ω_L ,³ as depicted in Figure 2.2.

²More specifically, for uncoupled spins, the results of this classical treatment are identical to those of a quantum mechanical description [41]. While spin coupling is known to result in peak splitting in some MRS experiments, it is not considered for this work as the relatively large linewidths obscure any effect.

³Angular frequency is given by: $\omega_L = 2\pi\nu_L$

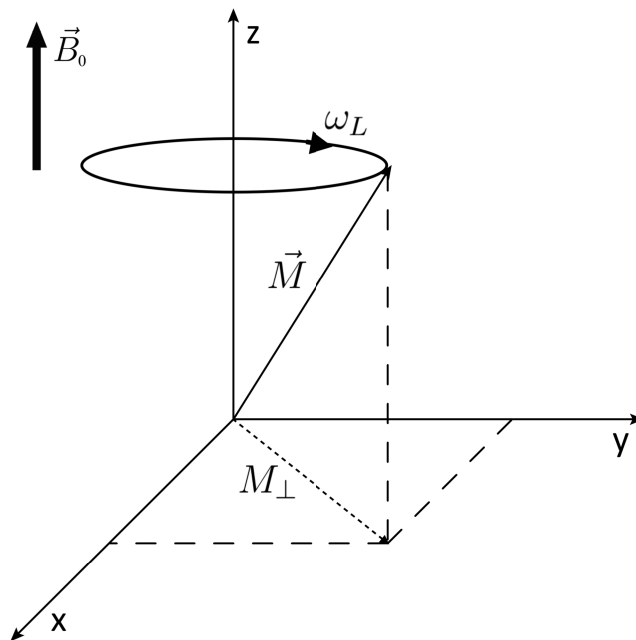


Figure 2.2: Precession of the net magnetization vector, \vec{M} , about the longitudinal direction. Signal detected is the current induced by the perpendicular component, M_{\perp} . As \vec{M} realigns itself with the applied magnetic field, \vec{B}_0 , the magnitude of M_{\perp} will decrease.

In MRI, \vec{M} is disturbed from equilibrium through application of an RF pulse, oriented such that it generates a magnetic field perpendicular to B_0 , denoted B_1 , oscillating at the Larmor frequency, ν_L . Just as the interaction between \vec{M} and B_0 causes \vec{M} to precess about the longitudinal direction, the interaction between \vec{M} and B_1 during the RF pulse will rotate \vec{M} away from the longitudinal axis. The degree of rotation is proportional to B_1 , as well as the duration of the RF pulse, and is described by the flip angle, α . For example, an RF pulse with $\alpha = 90^\circ$ would displace \vec{M} from the longitudinal axis to the transverse xy-plane.

Once displaced from the longitudinal axis, \vec{M} will have some non-zero transverse component, denoted M_{\perp} , as shown in Figure 2.2. As \vec{M} precesses about \vec{z} , its x and y components, $M_{\perp,x}$ and $M_{\perp,y}$, respectively, will oscillate at the Larmor frequency. If a coil of wire is oriented such that its axis aligns with the x-axis in Figure 2.2, the oscillation of $M_{\perp,x}$ will induce an oscillating current in the wire with the same frequency. The same may be said for a coil of wire aligned along the y-axis. This

oscillating current is the source of signal in an NMR experiment. In quadrature detection, the currents induced by $M_{\perp,x}$ and $M_{\perp,y}$ are detected simultaneously, represented as a complex signal $S(t) = S_x + iS_y$. In time, the magnitude of these oscillations will decrease, as shown in Figure 2.3; this process is known as relaxation. The signal produced is thus referred to as the free induction decay (FID) [41]:

$$S(t) = S_0 \exp(i\phi) \exp(i\omega_L t) \exp(-t/T_2^*) \quad (2.4)$$

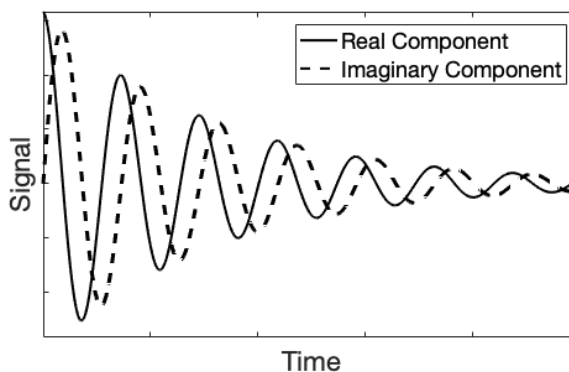


Figure 2.3: Real and imaginary components of the free induction decay, derived from components of M_{\perp} as it rotates about the longitudinal axis.

where S_0 is the signal amplitude and ϕ the initial phase offset. The exponential decay enveloping the oscillation of signal at Larmor frequency, ω_L , is characterized by time constant T_2^* , known as the observed transverse relaxation time. There are multiple factors that contribute to this signal decay, namely the recovery of equilibrium magnetization and dephasing of signal in the transverse xy-plane.

Molecular motion in the sample will cause nuclei to experience magnetic field fluctuations. If such fluctuations occur at the Larmor frequency, these nuclei can transition between the spin states shown in Figure 2.1, with slight preference for the lower energy state. In the classical picture, this loss of energy from the spins to their environment causes the net magnetization vector, \vec{M} , to return to its equilibrium value. The recovery of the longitudinal component of magnetization, M_z , is exponential, characterized by time constant T_1 . For an initial 90° RF pulse, such that M_z is initially zero:

$$M_z = M_0[1 - \exp(-t/T_1)] \quad (2.5)$$

Samples with more molecular motion at the Larmor frequency will have shorter T_1 relaxation times. However, this recovery process is not directly observed with NMR experiments, as measured signal is always generated by the transverse component of magnetization, M_\perp , and there are additional dephasing effects influencing this signal.

Local B_0 fluctuations experienced by small groups of spins, known as spin packets, cause their magnetization vectors to precess in the transverse plane at slightly different frequencies. While a 90° RF pulse, applied to spins aligned along the longitudinal axis, will rotate their combined \vec{M} such that those spins are still aligned in the transverse plane, slight differences in precession frequency between spin packets will result in a dephasing of the individual magnetization vectors over time, diminishing their combined signal, M_\perp . Factors influencing the magnetic field variations experienced by a these spins are typically broken up into two categories, smaller scale molecular field variations and larger scale B_0 inhomogeneities.

Dephasing resulting from the smaller scale molecular field variations, along with signal loss due to T_1 recovery processes, is characterized by transverse relaxation time, T_2 , sometimes referred to as the ‘true’ transverse relaxation time. For an initial 90° RF pulse, such that the transverse magnetization, M_\perp , is initially the size of the equilibrium magnetization, M_0 :

$$M_\perp = M_0 \exp(-t/T_2) \quad (2.6)$$

Given that T_2 encompasses dephasing due to these molecular field variations in addition to that resulting from T_1 recovery processes, $T_2 \leq T_1$. Furthermore, as high frequency molecular motions produce magnetic field fluctuations that are more likely to cancel out over time, T_2 relaxation times are shorter in samples with restricted molecular motion.

The additional dephasing processes resulting from larger scale B_0 inhomogeneities causes the observed signal to decay more quickly than that expected from T_2 , and is characterized by time constant T_2^* :

$$\frac{1}{T_2^*} = \frac{1}{T_2} + \frac{1}{T_{2,\text{inhomogeneity}}} \quad (2.7)$$

Of particular relevance to this work, the ‘true’ T_2 governed signal decay described in Equation 2.6, independent of that due to large scale B_0 inhomogeneities, can be observed using a basic spin echo sequence. With smaller scale molecular field variations, the field experienced by a single spin will be constantly changing due to molecular motions, whereas larger scale B_0 inhomogeneities, while spatially dependant, will be consistent for individual spins. As such, application of a second 180° RF pulse will cause a refocusing of spins dephased due to large scale B_0 inhomogeneities still experiencing the same field. The time delay between the initial RF pulse and the echo produced is denoted as the echo time, TE , and is twice as long as the time delay between the initial RF pulse and the later 180° pulse, as shown in Figure 2.4.

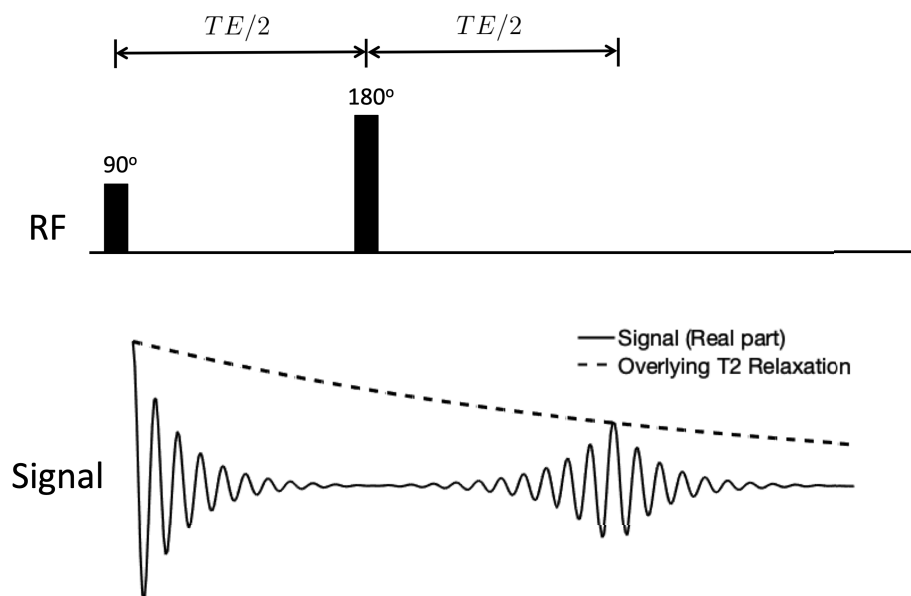


Figure 2.4: Pulse sequence diagram for a simple spin echo sequence.

2.2 Spatial Encoding

The simple spin echo sequence given in Figure 2.4 would generate a signal originating from any ^1H nuclei located in the magnet. While this is adequate for NMR experiments analyzing homogenous samples, for *in vivo* applications we are typically interested in limiting signal generation to some spatial region and, in the case of MRI, spatially resolving the signal. This can be done using magnetic field gradients, which introduce a spatial dependence to the precession frequency of nuclei:

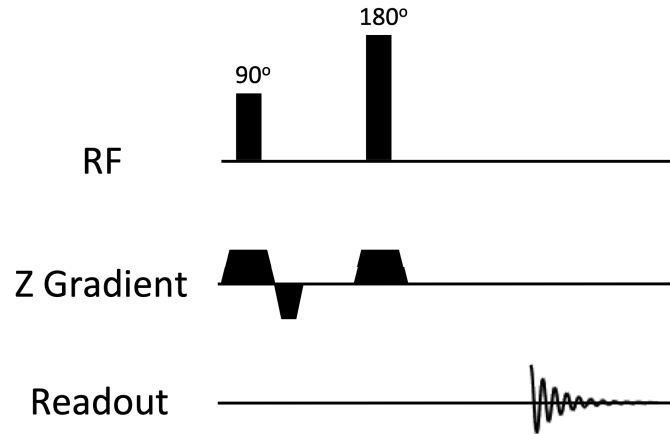


Figure 2.5: Pulse sequence diagram with axial slice selection for a spin echo sequence.

$$\nu(z) = \gamma(B_0 + G_z z) \quad (2.8)$$

where G_z describes the change in magnetic field from B_0 along the z -dimension (the same may be said for the x - and y - dimensions).

2.2.1 Slice Selection

MR signal generation can be limited to a single slice using slice selection. RF pulses will only affect spin packets whose magnetization vectors precess within some range of frequencies, denoted the transmit bandwidth (BW). Thus, while a gradient is applied, the spin packets affected by the RF pulse will be limited to a slice in space:

$$BW = \gamma G_z \Delta z \quad (2.9)$$

where Δz is the slice thickness. A pulse sequence diagram with axial slice selection for a spin echo sequence is given in Figure 2.5. Turning on a gradient along the longitudinal axis, \vec{z} , during the initial 90° RF pulse will limit signal generation to an axial slice. However, as this gradient introduces differences in precession frequency for different spin packets within the slice, dephasing of their magnetization vectors will reduce the signal the transverse plane. As such, a second rephasing gradient is applied following the RF pulse to reverse this effect. For the second, 180° re-focusing RF pulse, the effects of this dephasing cancel out.

2.2.2 Phase and Frequency Encoding

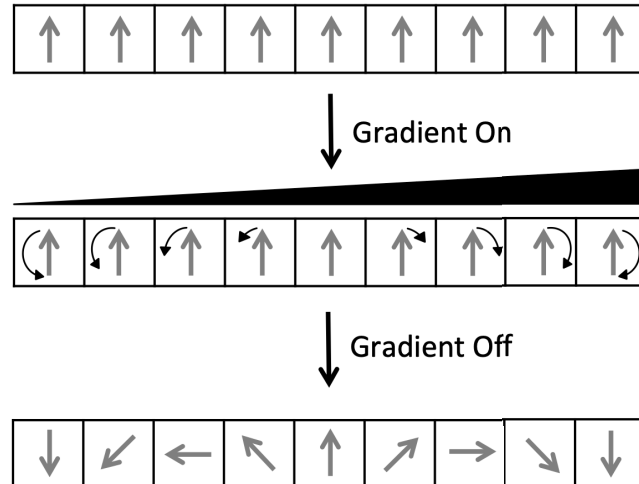


Figure 2.6: Phase encoding in 1D. Net magnetization vectors, \vec{M} , are displayed in a rotating xy-frame, such that rotation at the Larmor frequency is stationary.

Following slice selection, signal within a slice can be spatially resolved using phase and/or frequency encoding. In the former case, magnetic field gradients are applied (in two directions for a 2D acquisition, or in all three dimensions for a 3D acquisition) in order to induce a spatial dependence in the phase of the net magnetization vector, \vec{M} . This phase encoding process is shown in 1D in Figure 2.6. Following application of the initial RF pulse, \vec{M} is aligned for each voxel. Turning on a magnetic field gradient introduces spatial dependence to the precession frequency. After the gradient is turned off, the phase of \vec{M} is spatially dependent. As a result, signal generated by spin packets in different locations within the slice will undergo constructive or deconstructive interference. For example, the signal produced by the centre voxel in Figure 2.6 will destructively interfere with that produced by the first and last voxels. Thus, the measured signal is essentially that of the object, I , multiplied by a sine function characterized by wavenumber k [42], integrated over space:

$$S(t) = \int I(\vec{x}) \exp(-i2\pi\vec{k} \cdot \vec{x}) dx \quad (2.10)$$

where k is proportional to the gradient area:

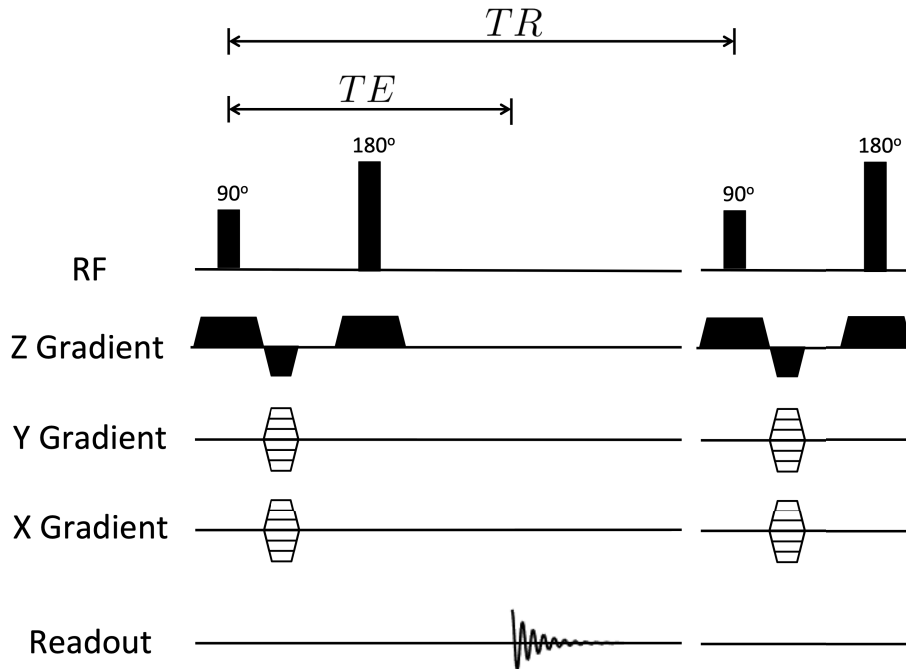


Figure 2.7: Pulse sequence diagram for a 2D phase encoded spin echo sequence.

$$k_x = \frac{\gamma}{2\pi} \int G_x(t) dt \quad (2.11)$$

Repeating this phase encoding process with different gradient areas, using a pulse sequence diagram like that given in Figure 2.7, each phase encoding step separated by repetition time, TR , will sample the image with sinusoids of varying k_x and k_y .⁴ As such, we say that MR data is acquired in k-space. This k-space data is essentially a Fourier transform [43], and the image, I , weighted by ^1H , or proton density, as well as relaxation parameters (e.g. T_1 , depending on TR), can be obtained through an inverse Fourier transform, as depicted in Figure 2.8.

In the case of frequency encoding, the gradients remain turned on during signal readout, such that a continual evolution of phase as described in Figure 2.6 can be used to acquire a whole line of k-space for each TR , as opposed to a single k-space point.

⁴While, as discussed in Section 2.1, the longitudinal component of magnetization is not measured directly, incomplete recovery of M_z prior to these repeated excitations will reduce the signal measured in the transverse plane.

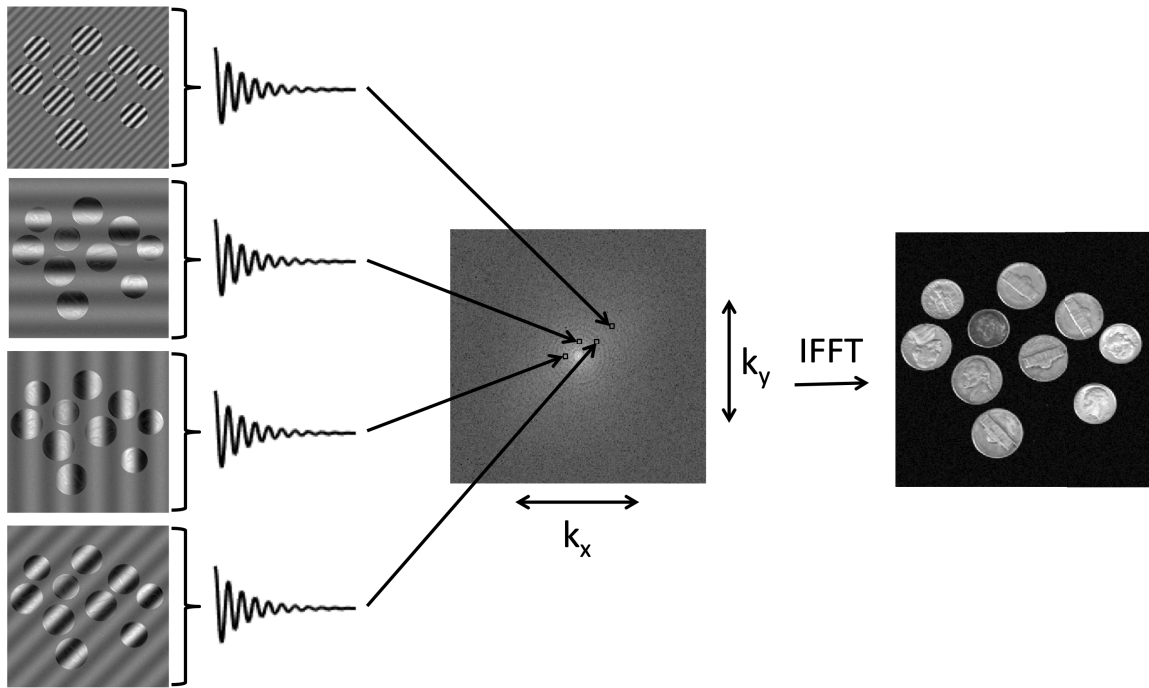


Figure 2.8: Reconstruction of a 2D image acquired with phase encoding. Acquiring FIDs while incrementally changing the phase encoding gradients produces will sample the image with sinusoids of varying wavenumber, k_x and k_y . This data is stored in k-space (log-scaled to show detail in the periphery), and the desired image in physical space obtained through a 2D inverse Fourier transform.

In understanding MRI acquisition, particularly undersampling as will be discussed in Section 2.4, it is useful to understand how different k-space regions contribute to the resulting image. Shown in Figure 2.9A is a fully sampled k-space dataset with its corresponding image. As discussed above, each point in k-space corresponds to the signal resulting from sampling the image with a 2D sine wave characterized by wavenumbers k_x and k_y . As such, points closer to the centre of k-space (small k_x and k_y) correspond to low spatial frequency components of the image, while points in the periphery correspond to high spatial frequency components. Shown in Figure 2.9B is the image produced from an inverse Fourier transform of the central region of k-space. Central k-space data contains the main contrast information of the image; however, the resulting image is blurred since fine detail information is described by the high spatial frequency components in the k-space periphery, as shown in Figure 2.9C.

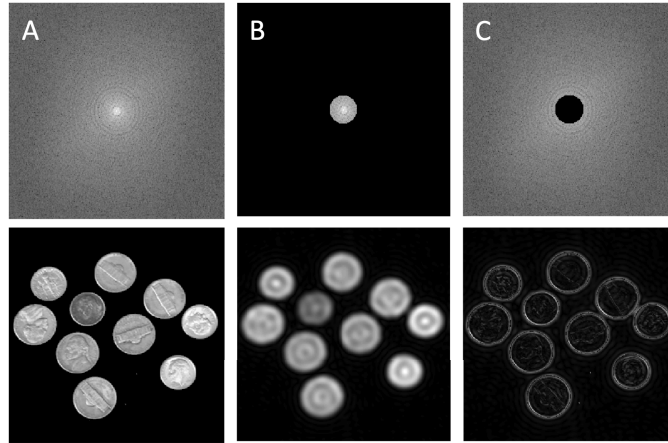


Figure 2.9: K-space datasets (log-scaled to show detail in the periphery) along with their corresponding images. (A) Fully sampled k-space dataset. (B) Central k-space data. (C) Peripheral k-space data.

2.3 Magnetic Resonance Spectroscopy

So far we have only considered spins precessing at or near the Larmor frequency. However, in addition to B_0 inhomogeneities and molecular field variations, the magnetic field experienced by these spins is also influenced by the chemical environment of the molecule. More specifically, differences in the electron clouds for different chemical environments will shield nuclei from B_0 to different degrees. Given the abundance of water in the human body, the majority of signal in conventional MRI images is generated by ^1H nuclei of water molecules, which all experience the same degree of shielding and precess, approximately, at the same Larmor frequency. However, in the presence of fat the FID will be composed of a number of different frequency components, corresponding to ^1H nuclei present in fatty acids, as shown in Figure 2.10A. From this representation it is difficult to visualize the presence of these different frequency components. As such, the signal is often portrayed as a spectrum in the frequency domain, obtained through a Fourier Transform, as shown in Figure 2.10B.

In this representation, T_2^* processes leading to signal decay described in Section 2.1 appear in the form of line broadening, with faster T_2^* decay resulting in broader spectral peaks. This effect is often described in the form of a damping factor, $d = 1/T_2^*$, such that larger damping factors correspond to broader spectral peaks, and vice versa. While decay due to T_2 and T_1 processes is out of our control, additional decay

due to B_0 inhomogeneities can be lessened by improved shimming of the field [44]. For a phased spectrum, whereby the initial phase offset for each frequency component of signal has been adjusted to $\phi = 0$, the signal magnitude of each component is given by the area under the real part of its corresponding peak.

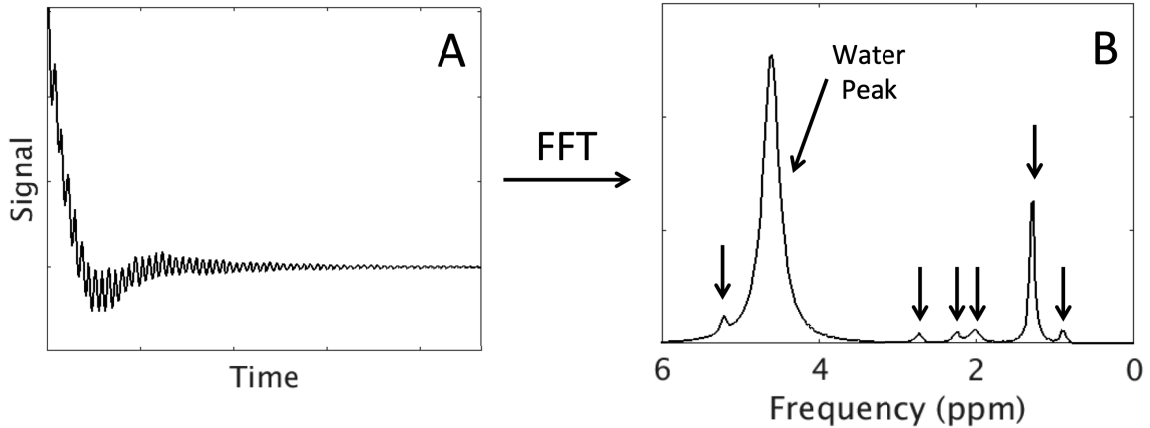


Figure 2.10: (A) FID (real part) produced by a sample containing both fat and water. (B) Spectrum (real part) resulting from the Fourier transform of this FID, showing the different frequency components of the signal. The water peak is located at approximately 4.7 ppm, while various fatty acid functional groups generate signal precessing at frequencies of about 5.3, 3.0, 2.3, 2.1, 1.3, and 0.9 ppm.

By convention, spectra in MRS are displayed with frequency increasing to the left, such that rightward peaks originate from spins experiencing a higher degree of shielding. The relative frequency difference between these peaks is known as chemical shift, δ , conventionally referred to in units of parts-per-million, or ppm, such that it is independent of field strength, B_0 :

$$\delta \text{ (ppm)} = \frac{\Delta\nu \text{ (Hz)}}{\gamma \text{ (MHz/T)} \times B_0 \text{ (T)}} \quad (2.12)$$

For the purpose of this thesis, six fat peaks are considered, as shown in Figure 2.10 and summarized in Table 2.2. Information about the relative proportions of SFAs, UFAs, and PUFAs, a potential biomarker for NAFLD progression as discussed in Section 1.2.1, can be derived from the relative amplitudes of these fat peaks (spectral processing is described further in Section 2.5) as follows.

SFAs will only contribute to Peaks 3, 5, and 6. UFAs contribute signal to all six of these peaks, but are unique to Peaks 1, 2, and 4. Furthermore, PUFAs are the

Table 2.2: Summary of fatty acid functional groups described in [23].

Peak Number	Name	Functional Group	Frequency Range (ppm)
1	Methene	$-\text{CH}=\text{CH}-$	5.2 – 5.4
2	Diallylic	$=\text{CH}-\text{CH}_2-\text{CH}=\text{CH}-$	2.8 – 3.1
3	α -Methylene to carboxyl	$\text{COO}-\text{CH}_2-\text{CH}_2-$	2.2 – 2.4
4	Allylic	$-\text{CH}_2-\text{CH}=\text{CH}-$	2.0 – 2.1
5	Methylene	$-\text{CH}_2-$	1.2 – 1.4
6	Methyl	$-\text{CH}_3$	0.8 – 1.0

sole contributor to the diallylic peak, Peak 2. Thus, Yeung et al. have proposed measuring the degree of unsaturation using the following unsaturation index, UI [45]:

$$UI = \frac{a_1}{a_1 + a_4 + a_5 + a_6} \quad (2.13)$$

where a_i are the relative amplitudes of the six fat peaks, as only Peaks 1, 4, 5, and 6 were considered in this case (the study was performed at 1.5 T) [45]. However, the close proximity of the methene peak (Peak 1) to the water peak introduces difficulties in calculating UI. Namely, application of a water suppression pulse may also impact the amplitude of the methene peak, but without water suppression (the case for this work) the methene peak can be hard to distinguish from the water resonance. As such, Johnson et al. proposed the following surrogate unsaturation index, UIs [23]:

$$UIs = \frac{a_2 + a_4}{a_2 + a_4 + a_5 + a_6} \quad (2.14)$$

Lastly, Johnson et al. also proposed measuring the relative amount of PUFAs using following polyunsaturation index, PUI, based on the diallylic peak (Peak 2) [23]:

$$PUI = \frac{a_2}{a_2 + a_4 + a_5 + a_6} \quad (2.15)$$

These three indices, given in Equations 2.13 to 2.15, are those considered for this work. While other metrics have been proposed [46, 24, 47, 48], UI, UIs, and PUI were consistent in our phantom studies, and have shown promise for characterizing NAFLD in clinical studies [23].

Point Resolved Spectroscopy

One method for obtaining these spectra is using point resolved spectroscopy, or PRESS. PRESS makes use of three slice selective RF pulses as shown in Figure 2.11. The first, 90° RF pulse selectively produces transverse magnetization in the xy-plane. The second, refocusing RF pulse only affects spin packets in a slice in the xz-plane, and the third only affects those in a slice in the yz-plane. As discussed earlier in this section, it should be noted that in MRS we are interested in signals from a range of ^1H nuclei with various chemical shifts. As a result, the slice of nuclei affected by each pulse will be slightly shifted relative to isocenter for each spectral peak. Nonetheless, limiting the excitation and two refocusing RF pulses in Figure 2.11 to three perpendicular, albeit potentially shifted, slices (in the xy, xz, and yz planes) will limit this refocusing effect to spin packets at the approximate intersection of those three slices, and magnetization outside the region of interest will continue to dephase due to T_2^* processes.

If magnetization outside this volume of interest has not completely dephased prior to readout, it will also contribute to the measured signal. Additionally, an imperfect 180° RF pulse may also generate transverse magnetization that can contribute to the FID following that pulse and future echoes. This unwanted signal is suppressed using crusher gradients appearing before and after each refocusing pulse. The second gradient completely dephases, or spoils the signal; however, it also affects the desired signal. Thus, a gradient of equal polarity and gradient area is applied prior to the refocusing pulse, pre-emptively nullifying the effect of the second gradient for spins located within the region of interest [49]. Choosing orthogonal crusher pairs for the two refocusing pulses prevents any unwanted rephasing effects [50, 44].

While PRESS and other spatially selective MRS methods allow for probing of specific volumes of interest, they are limited in terms of spatial coverage. Due to their slice selective nature, the edges of this volume cannot be curved, limiting voxel placement in non-rectangular regions of interest such as the liver. Furthermore, as the volume of tissue excited increases, B_0 within that volume will be less homogeneous, resulting in line broadening. However, based on the inhomogeneous nature of NAFLD, as discussed in Section 1.1, liver coverage is important for this work. This motivates the application of a spectroscopic imaging approach.

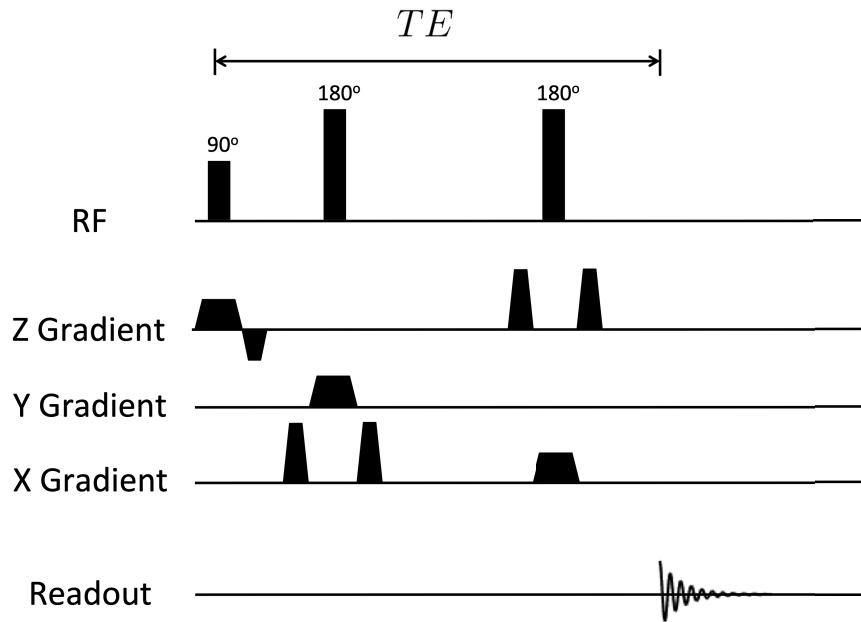


Figure 2.11: Pulse sequence diagram for a point resolved spectroscopy (PRESS) sequence [44].

2.3.1 Magnetic Resonance Spectroscopic Imaging

MR spectroscopic imaging, or MRSI, techniques acquire multivoxel MRS data, allowing for spatial mapping of each resonance. Compared to SVS techniques like PRESS, MRSI provides improved spatial coverage and spatial resolution, meaning partial volume effects can be more easily avoided. Although, given that this signal originates from a smaller region, the reduction in signal to noise ratio, or SNR, can adversely affect spectral quality. Additionally, the nature of the acquisition is prone to inter-voxel contamination, as described by the point spread function (PSF) [34]. The PSF of an imaging system describes its response to a point source, or Dirac delta function, $\delta(x)$:

$$\delta(x) = \begin{cases} 0 & \text{if } x \neq 0 \\ \text{undefined} & \text{otherwise} \end{cases}$$

where

$$\int_{-\infty}^{\infty} \delta(x) = 1 \quad (2.16)$$

Thus, the PSF of an ideal imaging system would also be a Dirac delta function, indicating no contribution from this point source to signal in other locations in the image. However, in MRI the truncation of data acquired in k-space produces rippling, or ringing, in the PSF. As such, image voxels may contain signal contributions from outside that voxel. The degree of this intervoxel contamination can be reduced by increasing the number of voxels acquired, but this requires a longer acquisition time. MRSIs are often spatially localized using phase encoding, as depicted in Figure 2.7 for a spin echo based sequence. As such, they require more time to be acquired than anatomical MRIs making use of frequency encoding,⁵ and are typically acquired with a lower resolution, amplifying this ringing effect.

Motivation for SE-SPI

Given the inherent scan time requirement for purely phase encoded imaging methods, there have been many approaches used in order to accelerate MRSI acquisitions for clinical use. As with conventional MRI applications, scans are typically accelerated in one of two ways - either by acquiring more k-space data per excitation, achieved by adjusting the pulse sequence used, or by reducing the number of total k-space points acquired. Additionally, a combination of these two methods may be used.

Two pulse-sequence based methods for accelerating MRSI acquisition are TSI and EPSI, based on the fast spin echo (FSE) imaging and echo-planar imaging (EPI) techniques used in conventional MRI applications, respectively. TSI makes use of multiple 180° refocusing RF pulses, each with unique phase encoding gradients, in order to cover multiple k-space points for each excitation. In this case, each echo will have a different T_2 weighting (the reconstructed image will be most influenced by the T_2 weighting for central k-space acquisitions). However, the application of TSI is limited by T_2 values of the nuclei of interest, as signal decay will limit the number of useful echoes that can be acquired [34]. TSI sequences for brain metabolite imaging, where T_2 relaxation times range between 100 – 400 ms [51], are limited to three or

⁵In the case of frequency encoding, a single resonance frequency is assumed and the chemical shift information of interest in MRSI is typically lost.

four echoes [34]. The T_2 relaxation times of the fatty acid groups relevant to this work, while variable, have been observed to be on the order of 50 ms for human liver scans [47].

On the other hand, EPSI makes use of oscillating gradients during readout, dephasing and rephasing spins to produce what are known as gradient echoes. As only spins that were dephased by these gradients are refocused, phase evolution resulting from chemical shifts can be used in order to encode spectral information, while frequency information can be used for spatial encoding. As such, each excitation, or TR , can be used to acquire a line of k-space as opposed to a single point. However, in this case the overlying exponential decay governing these echoes is characterized by time constant T_2^* as opposed to T_2 , as is the case for spin echo techniques. Thus, B_0 inhomogeneities shortening T_2^* , exacerbated by iron overload which may be present in cases of NAFLD [20], will result in spatial artefacts such as blurring in the resulting EPSIs as opposed to broadening of spectral lines.

Given the complications in applying these accelerated MRSI sequences for liver fat imaging, including the above-mentioned limitations as well as respiratory motion, this work makes use of a spin-echo based single point imaging technique, denoted SE-SPI, similar to that portrayed in Figure 2.7. While acquiring a single k-space point for each TR results in scan times which are too long for clinical application, SE-SPI acquisition can be accelerated by reducing the amount of k-space data acquired.

2.4 K-space Undersampling for Accelerated MR Acquisition

One method for accelerating MRSI is to exclude components of high spatial frequency in both the x and y directions, commonly done by limiting the acquisition of k-space data to a circular region, as shown in Figure 2.12A. However, while this undersampling has little impact on the resulting image, data reduction is typically no more than 40% [34], and the resulting acceleration factors are not high enough to achieve clinically feasible scan times for the purpose of this work.

Another method that makes use of k-space undersampling to accelerate MR acquisitions is parallel imaging. Parallel imaging reduces the number of phase encoding steps required by skipping entire k-space lines, shown in Figure 2.12B for the case of skipping every second line along the k_y direction. Reconstructing this k-space data

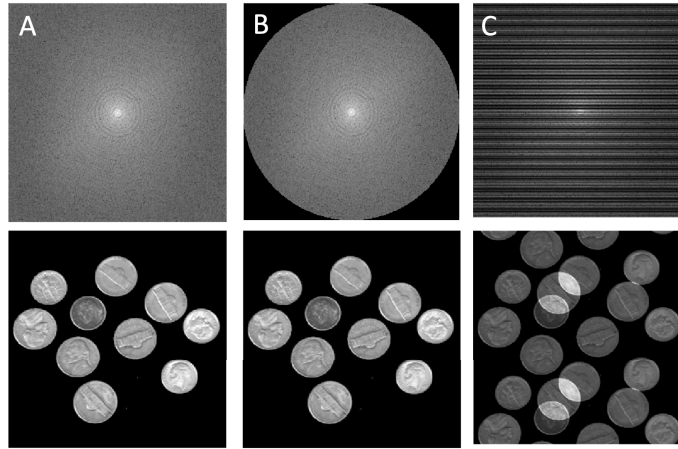


Figure 2.12: K-space datasets (log-scaled to show detail in the periphery) along with their corresponding images. (A) Fully sampled k-space dataset. (B) K-space dataset omitting points with high spatial frequencies in x and y . (C) K-space dataset omitting every second line along the k_y dimension.

directly results in aliasing in the corresponding image. This aliasing is a consequence of discrete sampling, described by separations Δk in the frequency domain.

In general, discrete sampling of k-space produces images appearing periodically in physical space, each image separated by a distance of $1/\Delta k$, known as the field of view (FOV). While Δk is typically chosen such that the FOV is large enough that these images do not overlap, in the case of parallel imaging this is not the case. However, the unaliased image can be obtained using data collected with multichannel receiver coils, as the spatial dependence of coil sensitivity for each channel introduces another degree of spatial encoding. This is either done by unwrapping signal in image domain, using sensitivity encoding (SENSE) [52], or filling in the missing k-space data in the frequency domain using generalized autocalibrating partial parallel acquisition (GRAPPA) [53]. High acceleration factors, e.g. $R = 4$, can be achieved using parallel imaging for MRSI, at the cost of SNR. While the application of parallel imaging requires multichannel coils, this is typically only a limitation in preclinical settings; the vast majority of clinical MR data is acquired using multichannel coils [54].

2.4.1 Compressed Sensing

While the two above-mentioned techniques accelerate MRSI acquisition by a regular undersampling of k-space, compressed sensing techniques make use of pseudorandom

undersampling. As was the case with parallel imaging, the main idea behind CS is to remove the resultant aliasing during reconstruction in order to obtain the true image. However, unlike parallel imaging this de-aliasing process is not done using additional information acquired during the scan, but rather by making an assumption about the nature of the data. Namely, that the data is well approximated by some sparse representation. Sparse representations of data make use of sparsifying transformations; i.e. the data is transformed to a basis in which it can be described by weighting a number of basis functions much smaller than the size of the signal itself. This concept is widely used in image compression applications, such as JPEG. The key to acceleration using CS is, having acquired undersampled data, to be able to recover the signal in its entirety using this sparsity assumption [55]. While MR data is not always sparse, it is often compressible, meaning it can be well approximated by a sparse representation [43, 55]. Although, the validity of this assumption relies on having chosen an appropriate sparsifying transform.

The way in which sparsity can be used to remove this aliasing can be understood as follows. Consider the time domain signal in Figure 2.13. The signal itself is sparse in the frequency domain; as shown by the fully sampled Fourier transform (Figure 2.13A). Randomly undersampling and zero filling this signal will produce random, incoherent aliasing in the frequency domain (Figure 2.13B); however, large components of signal are still visible. This incoherency is an important distinction from the coherent aliasing produced by equispaced undersampling in parallel imaging, whereby the aliased peaks would be indistinguishable from the underlying signal. By enforcing sparsity in the data (Figure 2.13C), we can pick out the largest peak component. Furthermore, knowing the undersampling pattern we can determine the contribution of this peak, with aliasing, to the total signal (Figure 2.13D). Subtracting this result from the total signal (2.13E) reveals another peak component. By iteratively repeating this process the underlying signal can be recovered (2.13F-J) [56].

Given the above-mentioned incoherency requirement, the design of the undersampling patterns used in CS applications is very important. Completely random undersampling produces random aliasing in the corresponding images, as shown in Figure 2.14B. However, as shown in Figure 2.14A, k-space data is typically distributed with the majority of signal attributed to the lower spatial frequency components. As

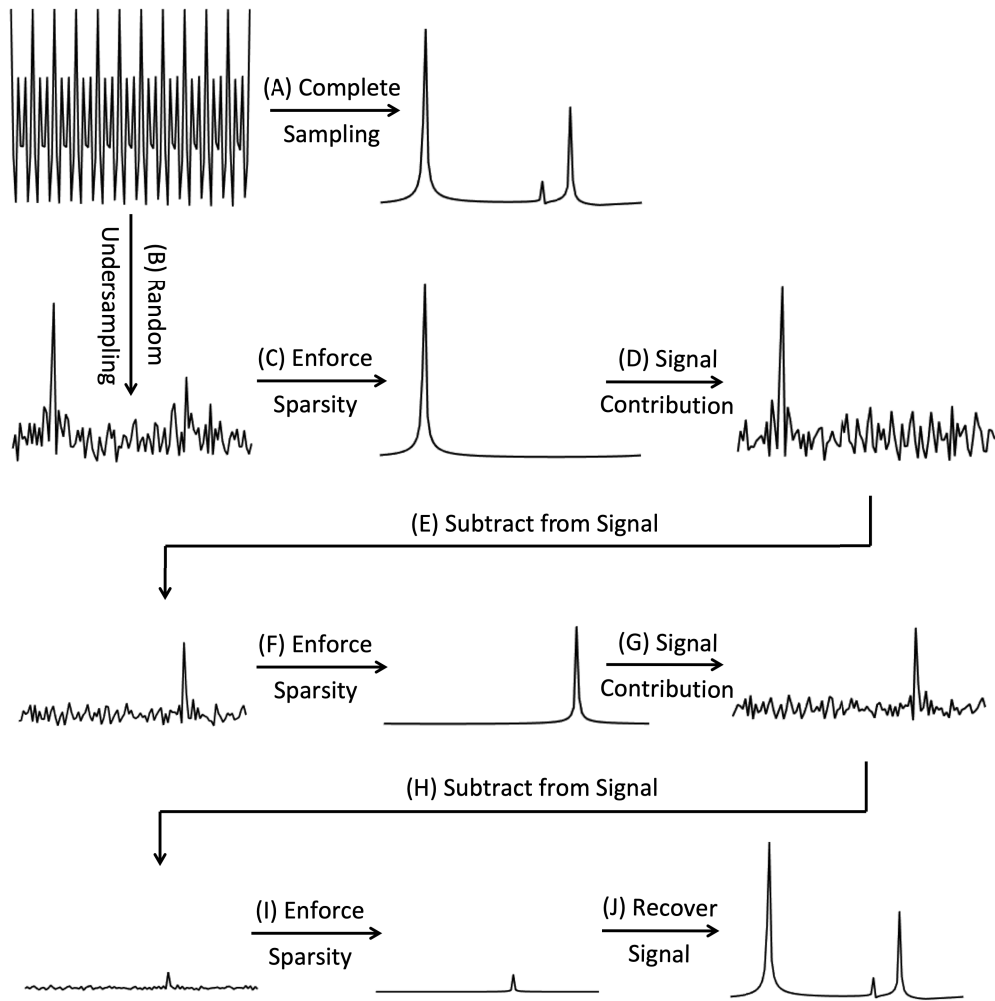


Figure 2.13: Diagram demonstrating how a sparse signal can be reconstructed from randomly undersampled data; based on [56].

shown in Figure 2.14C, preferentially sampling the centre of k-space retains the main features of the image, and the aliasing produced by undersampling is more noise-like. Thus, CS reconstructions of data acquired with this type of variable density undersampling, using a higher sampling density in the k-space centre as compared to the periphery, perform better than those generated with completely random, or uniform density undersampling [56].

While useful in demonstrating the main idea behind compressed sensing, the example illustrated in Figure 2.13 is limited in that the signal itself is truly sparse, and noise has been neglected. More formally, assume that in order to obtain a desired image, x , k-space is pseudorandomly undersampled, producing measurements, y [55]:

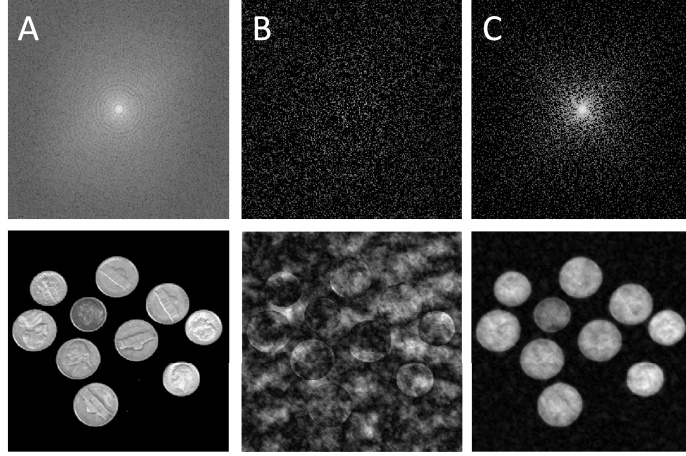


Figure 2.14: K-space datasets (log-scaled to show detail in the periphery) along with their corresponding images. (A) Fully sampled k-space dataset. (B) Undersampled k-space dataset generated with uniform density sampling. (C) Pseudorandomly undersampled k-space dataset drawn from variable density undersampling with the same undersampling factor.

$$y = Ax \quad (2.17)$$

where A summarizes the randomly undersampled Fourier transform. Assume that if x itself is not already sparse, it is well approximated by some sparse transformed representation, Φx . As long as the noise produced by undersampling is incoherent in the sparse representation, we can recover x by enforcing the sparsity of Φx . For example, quantifying sparsity using some l_p norm,⁶ commonly $p = 1$ or $p = 2$, x can be well approximated using the following optimization problem [55]:

$$x^* = \arg \min \|\Phi x\|_p \quad \text{s.t.} \quad \|Ax - y\|_2 \leq \epsilon \quad (2.18)$$

The first term ensures a sparse representation of image, x , and the second ensures that the recovered signal is consistent with the undersampled measurements, y , within some degree of noise, ϵ . Alternatively, the optimization problem formulated in Equation 2.18 can be written as follows [55]:

$$x^* = \arg \min \|Ax - y\|_2^2 + \lambda \|\Phi x\|_p \quad (2.19)$$

⁶The l_p norm of vector, b is given by $\|b\|_p = \sum_{i=1}^n (|b_i|^p)^{1/p}$

where the minimization problem contains both the data consistency and sparsity enforcing terms, the latter weighted by some regularization parameter, λ . Larger regularization parameters place more weight on the sparsity of the signal as opposed to data consistency, and vice versa. Enforcing sparsity allows us to pick out the true underlying signal from the noise-like aliasing produced by random undersampling, reducing the degree of noise in the recovered image, x . However, as MRIs are often not truly sparse, but well approximated by some sparse representation, placing too large a weight on sparsity as opposed to data consistency results in the loss of low contrast features from the recovered data [57, 58].

Blind Compressed Sensing

Anatomical MRIs, much like natural images, are known to be sparse through transformations such as the wavelet and discrete cosine transforms [56]. However, for dynamic imaging applications, sparsifying transforms in the time dimension are not as well defined. This has led to the development of blind compressed sensing (BCS) [57]. As opposed to assuming some sparse representation of the data *a priori*, BCS learns the sparsifying transform from the data itself.

For a dynamic dataset with m voxels and n images acquired, the Casorati matrix⁷ of the MR image, X , is modelled as:

$$X_{m \times n} = U_{m \times r} V_{r \times n} \quad (2.20)$$

For spectroscopy applications, n is the number of timepoints acquired in encoding each spectrum. V is a dictionary of r temporal basis functions used to represent the data, and U a matrix of coefficients. As with typical CS implementations, this signal is recovered by enforcing sparsity in the data, in this case by constraining the coefficients, U , while maintaining data consistency. The distinction of BCS is that both the dictionary, V , and coefficients, U , in Equation 2.20 are estimated in the reconstruction process, as opposed to the coefficients alone, using an iterative optimization algorithm, such that [59]:

⁷The Casorati matrix, $X_{m \times n}$, contains the spatio-temporal MR signal from an image with m pixels and n timepoints.

$$\{U^*, V^*\} = \arg \min \|A(UV) - Y\|_F^2 + \lambda \|U\|_p \quad \text{s.t.} \quad \|V\|_F^2 \leq c \quad (2.21)$$

As before, $Y = AX$ represents the undersampled k-space data, now for all timepoints (and coils, for multichannel data), with A summarizing the undersampled Fourier transform (and coil sensitivities, if applicable) of the desired dynamic image set, X . The Frobenius norm⁸ restriction on the dictionary, V , is used to prevent upscaling of the temporal basis functions, allowing much smaller coefficients, U , and effectively reducing the weight of the sparsity enforcing term. Given its close relation to the regularization parameter, λ , c may be defined arbitrarily as $c = 1$; similar results can be achieved with a different value of c , as long as λ is changed accordingly [57].

2.5 Hankel Singular Value Decomposition (HSVD)

Given the reconstructed MRSI, the dynamic dataset for our purposes, the fatty acid composition information of interest to this work can be calculated as described in Section 2.3. However, an important step was omitted in this discussion, that being the extraction of the relative peak amplitudes used in Equations 2.13-2.15. Since a vast number of voxels are acquired in many MRSI applications, automated quantification of spectra is often necessary for any feasible clinical application. There are many approaches to this type of spectral analysis; it can be done in the time or frequency domains, and can require varying degrees of user input and prior knowledge of the signal [60, 61]. For this work, an approach requiring no user input and with limited prior knowledge of the signal was preferred. In the time domain, many such approaches make use of a singular value decomposition of data arranged in a Hankel matrix, denoted HSVD .

Given the signal equation in Equation 2.4, and the knowledge that MRS signals are composed of varying frequency components, the time domain signal of these spectra is often modelled as [62]:

$$S(t) = \sum_{n=1}^N a_n \exp(i\phi_n) \exp(i\omega_n t) \exp(-d_n t) \quad (2.22)$$

⁸The Frobenius norm of a matrix, $B_{n \times m}$, is given by $\|B\|_F = \sqrt{\sum_{i=1}^n \sum_{j=1}^m |B_{ij}|^2}$

where N is the number of frequency components, and a_n the amplitude, ϕ_n the phase, ω_n the angular frequency, and d_n the damping factor associated with each of these frequency components. Assume the signal consists of i timepoints. This data is arranged in a Hankel matrix, $H_{l \times m}$, as follows [63]:

$$H_{l \times m} = \begin{bmatrix} S_0 & S_1 & \cdots & S_{m-1} \\ S_1 & S_2 & \cdots & S_m \\ \vdots & \vdots & \ddots & \vdots \\ S_{l-1} & S_{l-2} & \cdots & S_{i-1} \end{bmatrix} \quad (2.23)$$

where $i = l + m - 1$, $m > N$, and $l > N$. Assuming the signal model in Equation 2.22, the rank of H , i.e. the maximum number of linearly independent rows, would be N . However, for MRS signals H is actually full rank, a result of noise. The singular value decomposition of this matrix factors it in the following form [63]:

$$H_{l \times m} = U_{l \times l} \Sigma_{l \times m} V_{m \times m}^* \quad (2.24)$$

where Σ is a diagonal matrix containing what are called the singular values of H (real and non-negative), and the columns of U and V (both unitary matrices) denoted the left and right singular vectors corresponding to those singular values, respectively. By convention, these singular values are arranged in descending order ($\sigma_{11} > \sigma_{22} > \sigma_{33} > \cdots$). Thus, assuming adequate SNR, the true signal components can be separated from the noise by truncating this signal representation in Equation 2.24 to rank N [62]:

$$H_{l \times m} = U_{l \times N} \Sigma_{N \times N} V_{N \times m}^* \quad (2.25)$$

This representation is similar in form to the Vandermonde decomposition, which represents the signal in terms of its amplitude, phase, frequency, and damping components. Knowing the transformation between these two representations, the parameters of interest, namely a_n , ϕ_n , ω_n , and d_n , can be extracted from the HSVD. [63].

Chapter 3

Acquisition and Processing Pipeline

3.1 Undersampling Pattern Generation

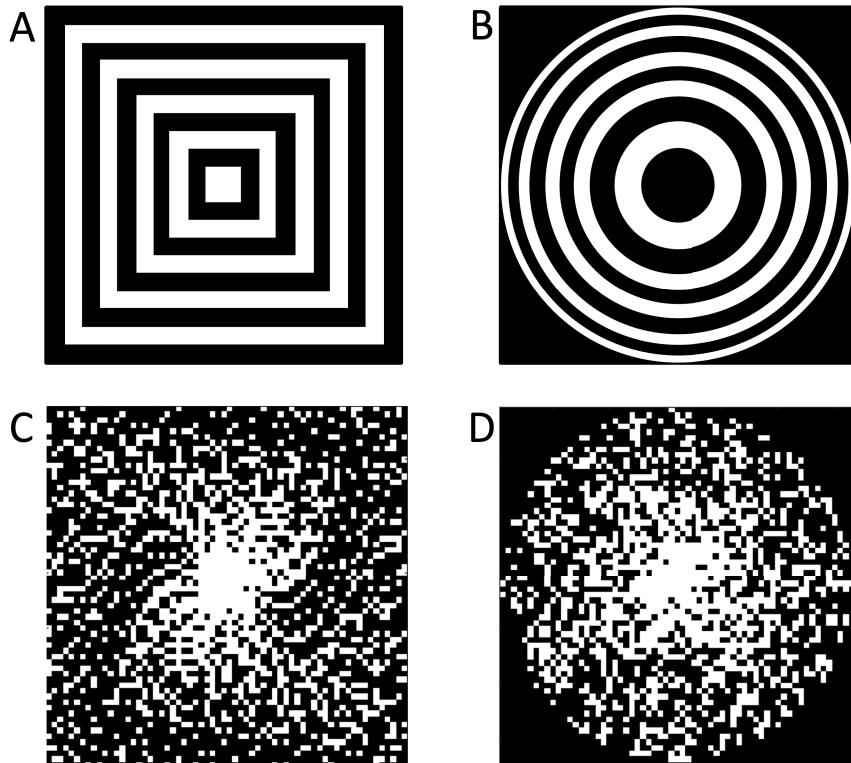


Figure 3.1: (A) Square shells used for the 2D CIRCUS implementation. (B) Spherical shells (slice $Z = 8$) used for the 3D CIRCUS implementation. (C) 2D undersampling pattern ($R = 3$). (D) 3D undersampling pattern ($R = 5.5$, slice $Z = 8$).

For this work, SE-SPI measures of fat composition were assessed both for fully sampled and accelerated scans. In the latter case, k-space undersampling patterns were generated using CIRCular Cartesian Undersampling (CIRCUS), which generates undersampling patterns by selecting points from a set of nested square shells [64]. For an $N \times N$ image there are $N/2$ such shells, of sizes ranging from 2×2 to $N \times N$. Selecting a constant number of points from each square shell results in a variable

density sampling pattern, with higher density sampling near the k-space center. The distribution of k-space sampling can be adjusted further by changing the number of points sampled for each shell. In either case, the points sampled are chosen based on a golden angle sampling strategy [65], ensuring a relatively uniform sampling distribution.

Since SE-SPI allows for undersampling in all spatial dimensions, the CIRCUS technique was modified to generate undersampling patterns in 3D. In this case, the undersampling patterns were generated by selecting points from a set of nested spherical shells, as pictured in Figure 3.1B, alongside the square shells used for the 2D implementation and corresponding undersampling patterns. Varying the incremental change in radius of these spherical shells ensured that the periphery of k-space was not too highly undersampled. The outer radius of the n^{th} shell, $n = 1 \dots N/2$, was calculated from [66]:

$$R_n = \sqrt{(n - 1) * N/2 + 9} \quad (3.1)$$

3.2 Respiratory Motion Correction

In addition to the long scan times associated with single point imaging techniques, *in vivo* spectroscopic imaging of the liver is complicated by respiratory motion. Motion corrupted points can be removed retrospectively using respiratory bellows or navigators, the latter of which track motion using additional RF pulses during the imaging sequence. Respiratory motion in the SE-SPIs used for this work was corrected retrospectively based on navigator signal, acquired following slice selection and prior to phase encoding, as shown in Figure 3.2A. While many navigators for clinical application use readout gradients in order to obtain line profiles of the image, in this case the phase of the navigator signal alone was sufficient for motion correction. K-space points whose phase fell outside one standard deviation of the average (corrected for drift) corresponded well with periods of motion as measured using respiratory bellows, shown in Figure 3.2B, and were thus removed prior to reconstruction.

Using this type of retrospective motion correction there is no way of knowing which points will be removed before the scan. This poses an issue for CS applications, as an appropriate pseudorandom undersampling pattern is vital to the quality

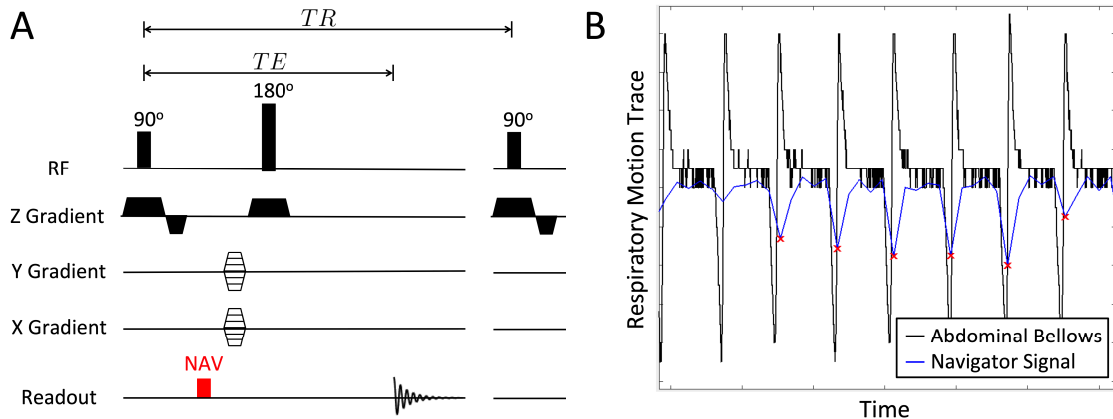


Figure 3.2: (A) SE-SPI sequence diagram with navigators for retrospective motion correction. (B) Comparison of mouse respiratory traces as measured using respiratory bellows and navigators in mice. Red points indicate navigator signals larger than one standard deviation of the average; such points were omitted prior to reconstruction. Reproduced from Rioux et al. [66]

of reconstruction. For this work, undersampling was based on CIRCUS [64]. Acquiring a number of undersampling patterns with golden angle strategy [65] ensured combination of multiple patterns with minimal overlap, as shown in Figure 3.3A. Disproportionately oversampling the k-space center ensured proper k-space sampling following retrospective motion correction, as shown in Figures 3.3B-C.

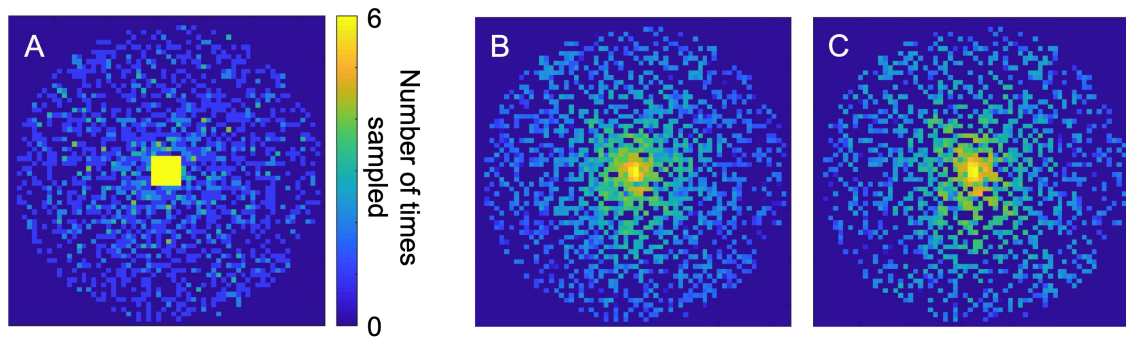


Figure 3.3: (A) Degree of sampling for each point in k-space (slice $Z = 8$) combining multiple 3D undersampling patterns. (B) K-space dataset acquired with the undersampling pattern given in (B), log-scaled to show detail in the periphery. (C) The same k-space dataset (also log-scaled) having removed motion-corrupted points.

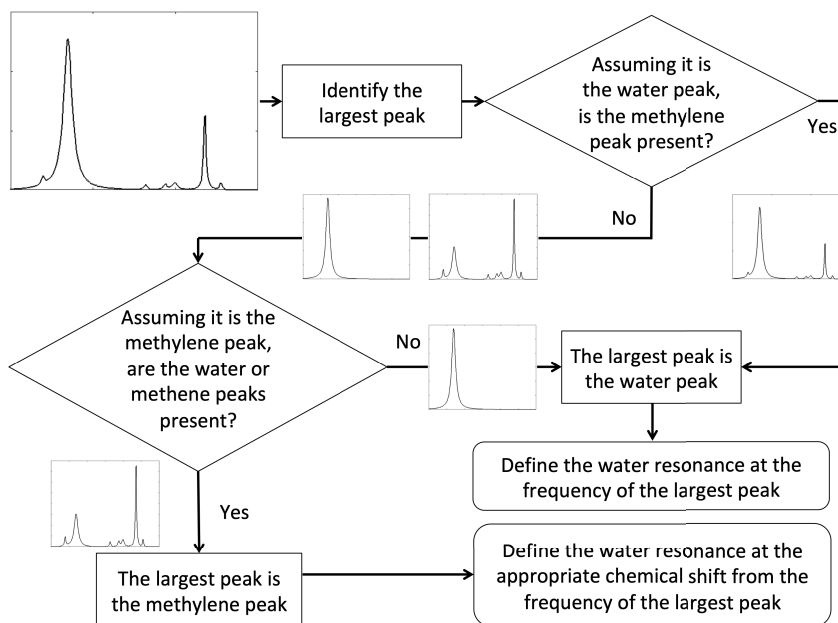


Figure 3.4: Flowchart summarizing the identification of the water resonance.

3.3 Spectral Processing

Undersampled data was reconstructed using BCS, as discussed in Section 2.4.1, using code provided by Bhave et al. [59]. Following reconstruction, spectra were processed using an HSVD-based binning algorithm that computed relative amplitudes of the six fat peaks and the water peak, as follows:

Step 1: Identification of the water peak The water resonance was identified as summarized in Figure 3.4. An initial HSVD was done assuming few frequency components (seven to nine). Assuming a smaller number of components, the HSVD process is less likely to fit single peaks with multiple components, as shown in Figure 3.5A, and less likely to pick out noise components. Baseline components were removed based on a damping (i.e. linewidth) constraint. Assuming the tallest peak was the water peak (4.9 ppm), components within the expected bin of the methylene peak (1.3 ppm) were identified (see Table 3.1). If present, the water peak was located at the frequency of the tallest peak. Else, assuming the methylene peak was the tallest peak, components of the water and methene peaks (5.3 ppm) were identified using the expected bins. If present, the methylene

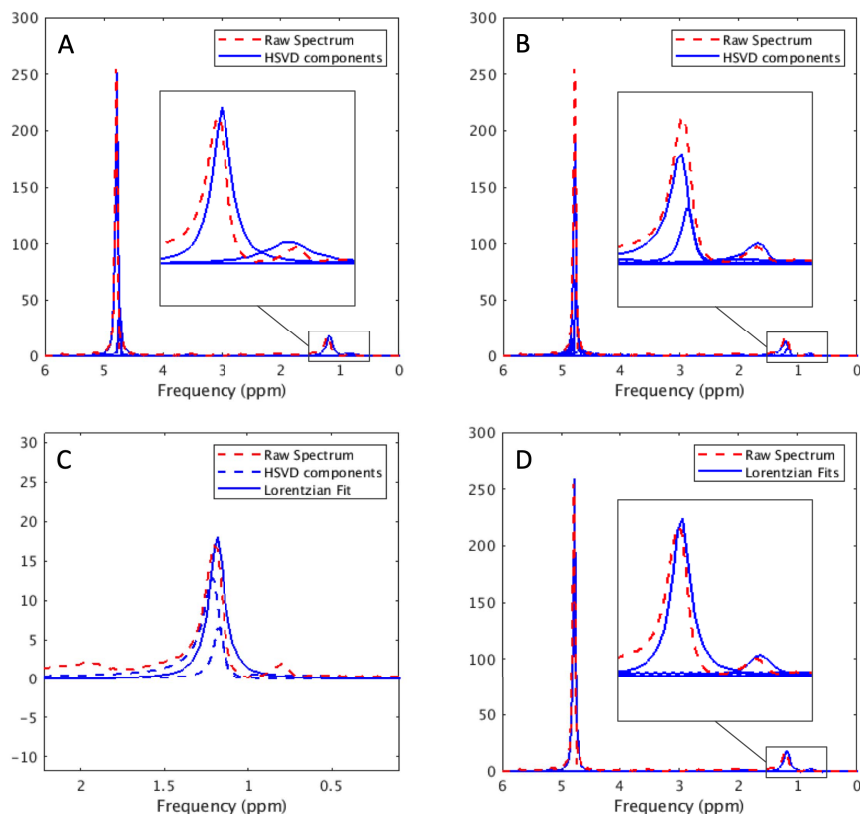


Figure 3.5: Processing of a PRESS spectrum for a 20% soybean oil tube. All spectra shown are unphased, absolute values displayed. (A) Initial HSVD assuming few components (seven), used in order to identify the water peak. (B) HSVD assuming more components (25), used in order to identify all peaks for binning purposes. (C) Lorentzian fit to two components falling within the bin for the methylene peak. (D) Lorentzian fits to all six fat peaks, as well as the water peak.

peak was labelled as the tallest peak, and the water peak located at the appropriate frequency shift. Else, water was defined at the frequency of the tallest peak, assuming the methylene peak was too small to be located.

Step 2: **HSVD to fit spectrum** The main HSVD was used to pull out important spectral components. This was done assuming more components ($N > 10$). While using more components is more likely to pick out noise in the spectrum, it provides a better fit to the data, especially for smaller peaks (see Figure 3.5B). Baseline components were again removed based on a linewidth constraint.

Table 3.1: Bins, based on those described in Johnson et al. [23], used in separating the fatty acid functional groups for phantom experiments. Bins were determined in reference to the water resonance, taken as 4.9 ppm, as expected for temperatures near 20°C [67]. Changes in the bin for the methyl peak for results of the clinical system were made based on visual assessment of PRESS spectra.

Peak	Frequency Bins (ppm)	
	Preclinical Experiments	Clinical Experiments
Methene (Peak 1)	5.15 – 5.45	5.15 – 5.45
Water	4.60 – 5.20	4.60 – 5.20
Diallylic (Peak 2)	2.65 – 2.95	2.65 – 2.95
α -Methylene to carboxyl (Peak 3)	2.15 – 2.45	2.15 – 2.45
Allylic (Peak 4)	1.83 – 2.13	1.83 – 2.13
Methylene (Peak 5)	1.15 – 1.45	1.15 – 1.45
Methyl (Peak 6)	0.61 – 0.91	0.73 – 1.03

Step 3: Binning of components Based on the expected peak locations relative to the water peak, HSVD components were binned in one of the six fat peaks or the water peak. Peaks outside of these bins were removed. If multiple components were assigned to a single peak, a complex Lorentzian was fitted to the sum of these components [68], as shown in Figure 3.5C. In general, no prior knowledge of relative peak amplitudes was used in this binning process. However, in order to prevent the assignment of water peak components to the methene peak, especially in cases of peak splitting for *in vivo* PRESS measurements, large components (defined relative to the amplitude of the methylene peak) within the methene bin were omitted in some cases.

Step 4: Computation of relative peak amplitudes Relative peak amplitudes were determined from the area under the Lorentzian fits, shown in Figure 3.5D. The fat fraction was calculated as follows:

$$FF = \frac{\sum_{n=1}^6 a_n}{a_w + \sum_{n=1}^6 a_n} \quad (3.2)$$

where a_1 to a_6 are the amplitudes of each fat peak and a_w that of the water peak. Given the relative amplitudes of each fat peak, UI , UIs , and PUI were calculated as described in Equations 2.13-2.14.

It is important to clarify that this spectral processing was performed for each individual SE-SPI voxel, as opposed to a sum of spectra within a region of interest (ROI). Summing spectra within an ROI would result in an improved SNR prior to the HSVD. However, since spectra were not phased prior to this decomposition, phase drifts across the ROI, observed to be on the order of π radians for the same fat peak in some cases, resulted in partial cancelation of peaks from voxel to voxel.

It is also important to distinguish the signal fat fraction given in Equation 3.2 from the proton density fat fraction (PDFF) often used in MRI applications for NAFLD. Calculation of the PDFF would require correcting for confounding factors such as T_1 saturation and T_2 relaxation, as differences in the T_1 and T_2 relaxation times of fat and water, in addition to their proton densities, will also affect their relative signal magnitudes [69]. While determining these T_1 and T_2 relaxation times would have enabled such a correction, this was not necessary for comparison of results acquired with matched TR/TE .

On a similar note, individual fat peaks have also been shown to have different relaxation properties [47, 70]. As such, the fat composition metrics, UI , UIs , and PUI , computed here should not be taken as proton density measures, but relative metrics, and are unlikely to equate with literature results acquired with different acquisition parameters (e.g. field strength, TR , TE).

3.4 Methods

3.4.1 Phantom Design and Acquisition

Prior to evaluating SE-SPI for lipid composition quantification, phantom studies were performed to inform the choice of post processing parameters. This was assessed on both preclinical and clinical imaging systems using a set of five 100% oil samples; namely flaxseed (Flora, unrefined from Organic Earth Market, Halifax, Canada), peanut (No Name from Atlantic Superstore, Halifax, Canada), safflower (Spectrum Naturals, refined, from Organic Earth Market, Halifax, Canada), sesame (Spectrum

Naturals, unrefined, from Organic Earth Market, Halifax, Canada), and soybean oils (Mazola Vegetable Oil from Atlantic Superstore, Halifax, Canada). For imaging with the preclinical system, these oils were contained in 10 mm diameter NMR tubes. For imaging with the clinical system, they were contained in 60 ml sample containers (diameter ≈ 4 cm). Another set of soybean oil tubes of varying fat fraction (20%, 15%, 10%, and 5%) were made up from dilutions of Intralipid, or intravenous (IV) fat emulsion (20% soybean oil, Fresenius Kabi, Bad Homburg, Germany). A Gadolinium contrast agent (Gadoteridol, Bracco Imaging, Milan, Italy) was added to these soybean oil emulsions in order to attain relevant water T_1 values ($T_1 \approx 1000$ ms, about 0.16 mM per volume of water). The results of imaging these tubes with the clinical system are omitted from this work due to coalescence of the soybean oil emulsions.

Lipid composition quantification was first assessed on the 3T preclinical MRI system, a product of Oxford Instruments (Concord, US), operated using a Varian (Palo Alto, US), later Agilent (Santa Clara, US) console. All preclinical data was acquired using a quadrature RF coil (Doty Scientific, Columbia, US) with an inner diameter of 30 mm. SE-SPI parameters were consistent for all preclinical experiments, including those given in Chapters 4 and 5, with $TR/TE = 200/13$ ms, receiver $BW = 3$ kHz, $FOV = 30 \times 30 \times 10$ mm, and 512 points acquired at each readout. 2D scans were acquired in a 64×64 matrix, and 3D scans in a $64 \times 64 \times 8$ matrix. For PRESS, acquisition parameters were matched to those of SE-SPI ($5 \times 5 \times 5$ mm voxel, 25 averages).

Having assessed the viability of SE-SPI in a preclinical setting, it was then evaluated on a 3T GE MR750 scanner (GE Healthcare, Waukesha, US). Data was acquired using both single channel and 32-channel head coils, as well as a 32-channel cardiac coil (GE Healthcare, Waukesha, US). For clinical PRESS acquisitions, TR/TE could not be matched to that intended for clinical SE-SPI scans due to limitations of the clinical system. Instead, PRESS voxels were acquired using $TR/TE = 250/29$ ms ($BW = 3$ kHz, $2 \times 2 \times 2$ cm voxel, 512 points acquired at each readout, 32 averages with the single channel coil, 16 averages with the multichannel coils). Individual tubes were shimmed with higher order shimming prior to all PRESS acquisitions. Coil combination for PRESS data was done using GE reconstruction software. Given the variety of coils and imaging parameters used for SE-SPI acquisitions, SE-SPI

parameters for clinical experiments will be stated separately in Sections 3.4.3, 3.4.4, and 4.1.

3.4.2 Choice of Parameters: Spectral Analysis

As briefly discussed earlier in Section 3.3, the number of frequency components assumed in the HSVD-based spectral decomposition can have an impact on quantification. Namely, assuming too few components will not accurately model the spectrum, while assuming too many components will result in an increased noise contribution. As such, the optimal number of frequency components was assessed prior to the direct assessment of fat composition quantification. Given the impact of MR acquisition parameters on lipid composition quantification, also discussed in Section 3.3, consistency was used as a measure of decomposition quality as opposed to agreement with a gold standard such as literature results. Furthermore, given inconsistencies in shimming the phantoms from session to session, intrasession reliability was preferred over intersession reliability.

With the preclinical imaging system, five pairs of PRESS voxels were acquired for each of the soybean oil tubes of varying fat fraction in order to assess this intrasession reliability. For comparison, a similar analysis was performed for a single session imaging the pure oil phantom (five pairs of PRESS voxels of varying pure oil samples). Tubes were rearranged and reshimmed for each session. With the clinical imaging system, six pairs of PRESS voxels were acquired for each pure oil tube; three pairs with the single channel head coil and three with the 32-channel head coil.

In both cases, the number of frequency components assumed in the spectral decomposition was determined from:

$$N = \arg \min \sum_{\text{tube}=1}^5 \sum_{\text{peak}=1}^6 \sum_{\text{session}} (A_1(N) - A_2(N))^2 \quad (3.3)$$

where A_1 and A_2 are the relative fat peak amplitudes determined from the first and second PRESS measurements within a single session, respectively, and N the number of components assumed in the HSVD. Numbers of components ranging from $10 \leq N \leq 30$ were considered. Assuming fewer than $N = 10$ components resulted in many of the smaller fat peaks being missed, even without the presence of a water

peak.

In order to ensure that assuming this number of components, N , given by Equation 3.3 was also appropriate for SE-SPI spectra, a similar analysis was performed with results from the preclinical system, comparing fat peaks amplitudes calculated from PRESS data to those calculated from an SE-SPI acquired in the same session.

3.4.3 Choice of Coil Combination Weightings

All preclinical experiments were performed with a single channel coil. However, for clinical implementation multichannel coils are preferred. Thus, a variety of coil combination methods were investigated for SE-SPI reconstruction prior to the assessment of fatty acid composition measurements. Three 2D fully sampled SE-SPIs were acquired with each head coil, using $TR/TE = 200/11$ ms, receiver $BW = 4$ kHz, $FOV = 20 \times 20 \times 1$ cm, a 64×64 matrix, and 512 points acquired at each readout. Single channel SE-SPI measurements were compared with those made with the multichannel head coil using a variety of coil combination weightings, following a 0th-order phase correction. In total, four coil weightings were investigated, as summarized in Table 3.2, based on those described by Hall et al. [71]. Noise was quantified in the frequency domain as the standard deviation in areas free of expected peaks [72, 73]. Weightings taking signal magnitude into account were tested using both the signal itself (quantified as the maximum magnitude of the FID) as well as coil sensitivities, obtained with GE’s ASSET calibration scan. Prior to the calculation of these coil sensitivities, multichannel data was compressed to 8 virtual channels using the BART toolbox [74].

Table 3.2: Summary of coil combination weightings investigated for clinical experiments. w indicates the weight applied to the signal of a single channel, S the relative signal magnitude measured with that channel, C a measure of coil sensitivity obtained using a calibration scan, and N a measure of noise of the channel.

Description	Weightings Used
Equal Weighting	$w = 1$
Signal Weighting	$w = S$ or $w = C$
SNR Weighting	$w = S/N$ or $w = C/N$
S/N^2 Weighting	$w = S/N^2$ or $w = C/N^2$

3.4.4 Choice of Parameters: Compressed Sensing Reconstruction

Having chosen the number components, N , to assume in spectral analysis, and coil combination weightings for clinical SE-SPI data, the next step was to determine what parameters to use for the BCS reconstruction, performed using code provided by Bhave et al. [59]. The quality of this reconstruction is dependant on a number of factors, including the regularization parameter, λ , the number of basis functions, r , and the number of iterations, n_{iter} used for reconstruction, as discussed in Section 2.4.1. Furthermore, the maximum signal magnitude of the undersampled k-space data, equivalently defined as the scaling factor, s , applied to data normalized to a maximum signal magnitude of one, was also observed to have an impact on the results of the BCS reconstruction. As such, a variety of combinations of reconstruction parameters were considered, as summarized in Table 3.3. Remaining reconstruction parameters were left unchanged.

Table 3.3: BCS parameters investigated, namely the numbers of iterations, n_{iter} , numbers of basis functions, r , regularization parameters, λ , and scaling factors, s .

Parameter	Value
n_{iter}	15, 30, 50
r	25, 30, 35, 40, 45
λ	0.0001, 0.001, 0.005, 0.01, 0.05
s	0.1, 0.5, 1, 2, 10

With the preclinical system, a fully sampled 3D scan of the soybean oil emulsions was acquired, taking 3.5 hours, and the effects of changing BCS reconstruction parameters assessed retrospectively. A 3D scan was used given that 3D SE-SPIs were acquired in the mouse study. Similarly, the retrospective undersampling factor used was $R = 5.5$ in order to match that observed in the mice; while mouse scans were prospectively accelerated by a factor of $R = 4$, retrospective motion correction resulted in an undersampling of k-space by a factor of $R \approx 5.5$.

With the clinical system, a fully sampled 2D SE-SPI was acquired using the cardiac coil with $TR/TE = 200/11$ ms, $BW = 4$ kHz, $FOV = 32 \times 32 \times 1$ cm, a 64×64 matrix, and 512 points acquired at each readout. This scan was then retrospectively undersampled by a factor of $R = 3$ and reconstructed with the BCS parameter

combinations summarized in Table 3.3. In this case, R was chosen based on that observed in preliminary quality assurance scans of the CS SE-SPI sequence, with human subjects, used in developing the clinical protocol. In order to achieve a 10 minute acquisition time, scans were prospectively accelerated by a factor of $R = 1.4$. Following motion correction, k-space was undersampled by a factor of $R \approx 3$.

In both cases, the quality of each reconstruction was quantified using the pixel-wise mean squared error (MSE) of each relative fat peak amplitude in each of the five oil tubes, relative to the fully sampled scan, as depicted in Figure 3.6 using a scan acquired with the preclinical system. A single MSE was determined for each set of BCS reconstruction parameters by averaging over the six fat peaks and five oil tubes:

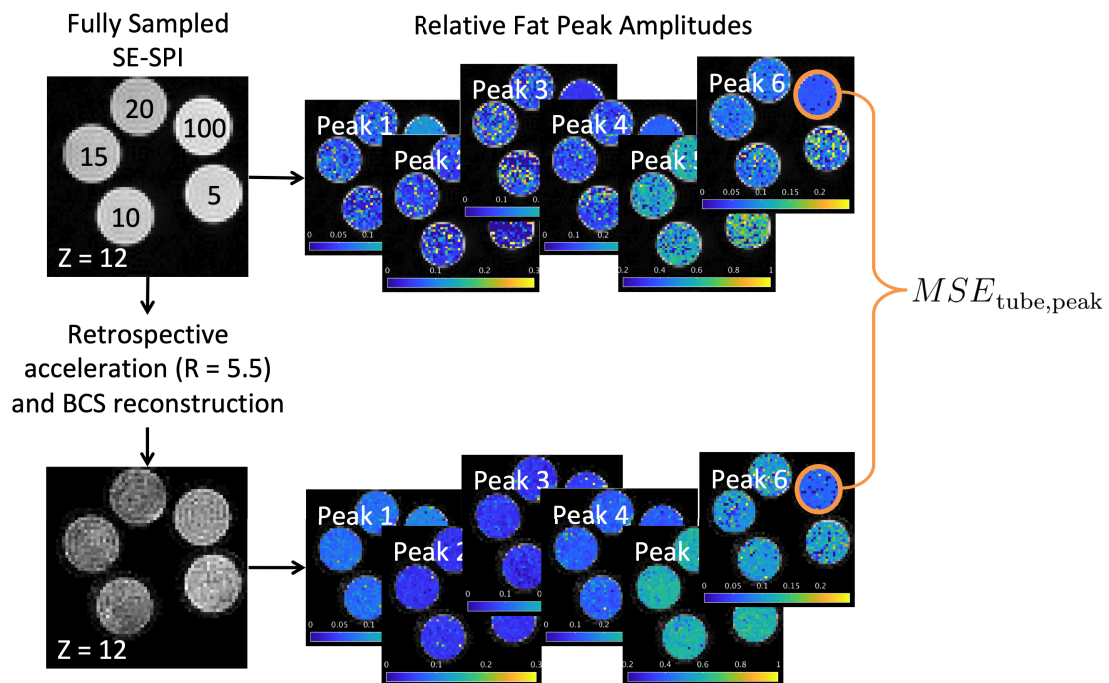


Figure 3.6: Diagram demonstrating the calculation of MSE used in order to assess the quality of BCS reconstructions with varying reconstruction parameters. For the preclinical system, a fully sampled 3D SE-SPI of five soybean oil tubes of varying fat fraction (100%, 20%, 15%, 10%, and 5%, as indicated) was retrospectively undersampled by a factor of $R = 5.5$, and reconstructed using BCS. Relative peak amplitudes for each of the six fat peaks were calculated for both the fully sampled and retrospectively accelerated scans. In order to limit computation time, only two of the 16 slices were considered; one central slice ($z = 8$, not shown) and one more peripheral slice ($z = 12$, as shown). The MSE between fully sampled and BCS reconstructed results were calculated individually for each fat peak and oil tube.

$$MSE(n_{iter}, r, \lambda, s) = \frac{1}{5} \sum_{\text{tube}=1}^5 \frac{1}{6} \sum_{\text{peak}=1}^6 MSE(n_{iter}, r, \lambda, s)_{\text{tube,peak}} \quad (3.4)$$

3.5 Results

3.5.1 Choice of Parameters: Spectral Analysis

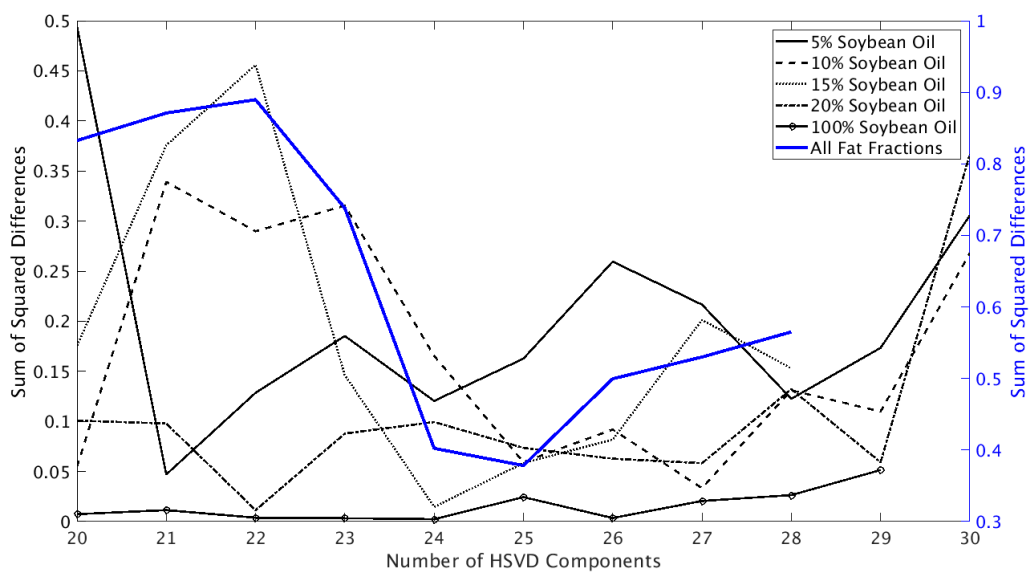


Figure 3.7: Squared differences between fat peak amplitudes measured by each pre-clinical PRESS pair, summed over the six fat peaks and five repetitions for each of the soybean oil tubes (in black), as well as that summed over the five fat fractions (in blue), as a function of assumed spectral components, N . Gaps in the plots indicate undefined results, either due to failed HSVD or failure to detect one or more of the fat peaks.

Using Equation 3.3, the preferred number of components to assume in analyzing the preclinical soybean oil emulsions was found to be $N = 25$. Plots of the total sum of squared differences and that for the individual tubes are given in Figure 3.7. Results are shown for numbers of components ranging from $20 \leq N \leq 30$, since using fewer than $N = 20$ components resulted in many of the smaller fat peaks going undetected by the HSVD. A similar check computing the difference between PRESS and SE-SPI measurements acquired within a single session indicated 24–25 components provided the best agreement (data not shown). As such, it was assumed that using $N = 25$

components would be appropriate for both techniques. Also using Equation 3.3, the optimal number of HSVD components to use when analyzing the preclinical pure oil tubes was found to be $N = 13$.

Similarly, the preferred number of HSVD components to use in analyzing the clinical pure oil tubes was found to be $N = 14$. Plots of the total sum of squared differences are given in Figure 3.8, showing an upward trend in intrasession variability with increasing numbers of HSVD components. Given that the trend in HSVD behaviour was not as smooth as that observed with the preclinical soybean oil tubes, shown in Figure 3.7, results are shown for a larger range of HSVD components ($N = 10$ to $N = 50$) to provide additional confidence in the validity of this trend.

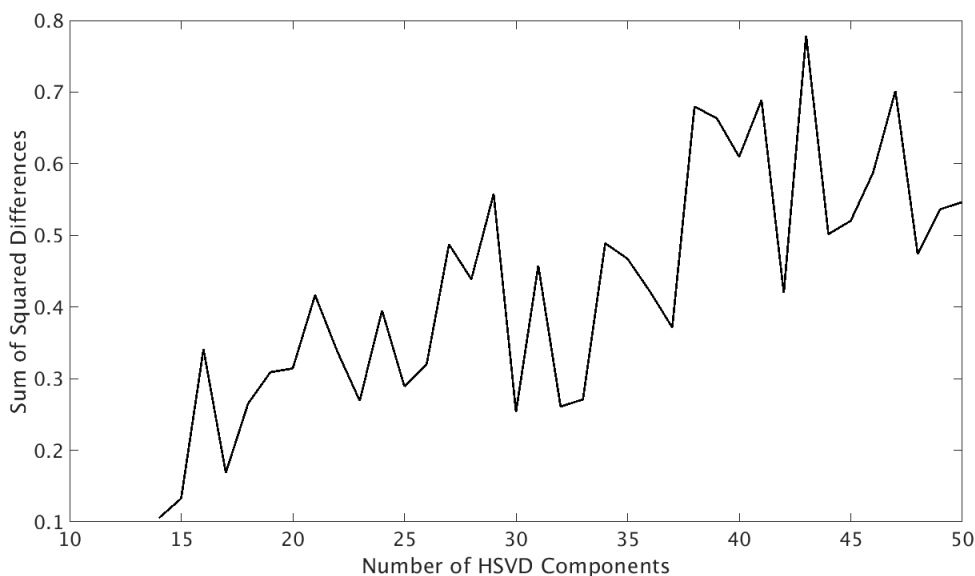


Figure 3.8: Squared differences between fat peak amplitudes measured by each clinical PRESS pair, summed over the six fat peaks, six repetitions, and five oil types, as a function of the assumed number of spectral components, N . For $N < 14$ some of the smaller fat peaks could not be detected.

3.5.2 Choice of Coil Combination Weightings

Given in Figure 3.9 are the fatty acid composition indices calculated from fully sampled SE-SPIs acquired using a single channel head coil, along with those calculated from scans acquired with the multichannel head coil using a variety of weighting factors for coil combination. In most cases, changing these weightings did not have a

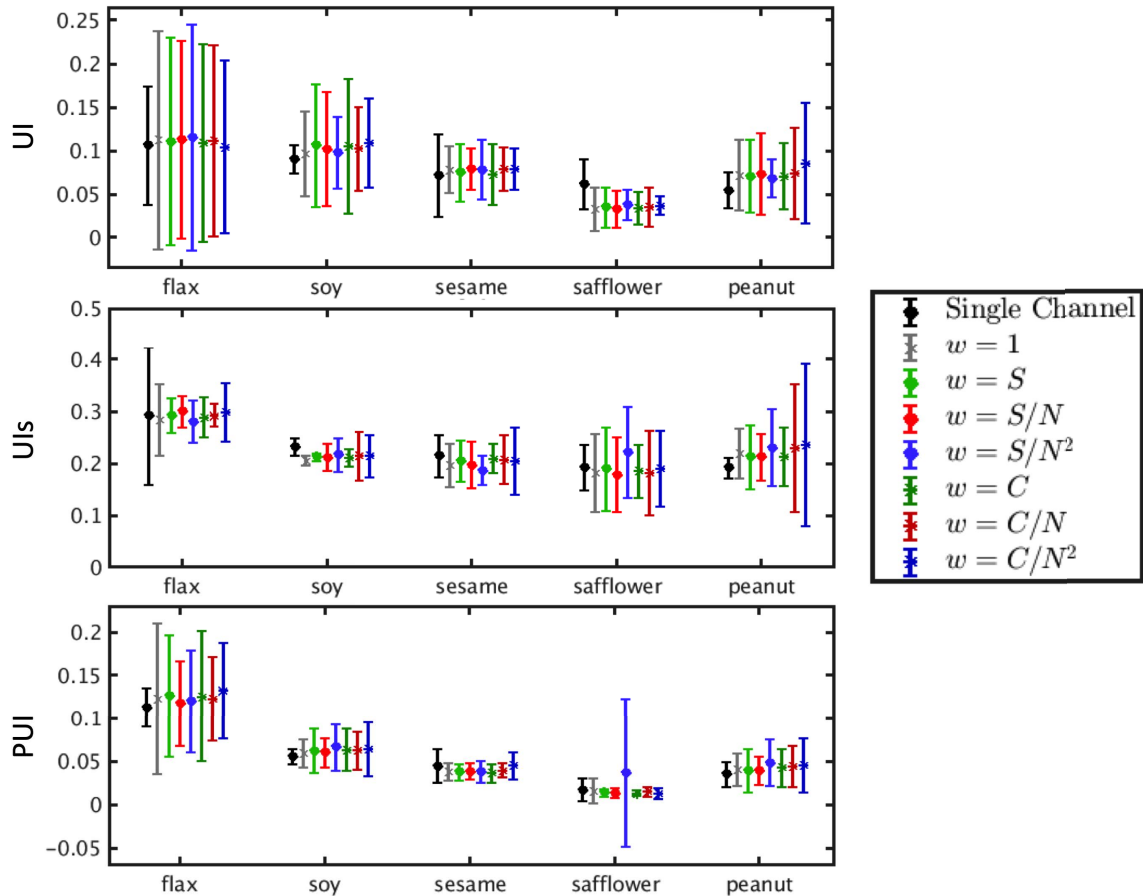


Figure 3.9: Unsaturation (UI), surrogate unsaturation (UIs), and polyunsaturation (PUI) indices (mean \pm 95% CI over 3 scans) for the flax, soybean, sesame, safflower, and peanut oil tubes as measured using the clinical system with the single and multichannel head coils. In the latter case, results are shown for a variety of coil combination weightings.

large impact on fatty acid quantification. As such, signal weightings using coil sensitivity ($w = C$) were chosen as this method was already implemented in the BCS code provided.

3.5.3 Choice of Parameters: Compressed Sensing

Shown in Figure 3.10 is the fully sampled 3D SE-SPI used to investigate the impact of changing BCS reconstruction parameters on fat composition quantification with the preclinical system. The SNR for central slices of the SE-SPI was much better than that for peripheral slices due to limitations of the preclinical RF pulses used for

slice selection.

The effect of varying BCS parameters on the relative fat peaks amplitudes can be seen from Figures 3.11-3.14. As shown in Figure 3.11, increasing the number of iterations used in the BCS reconstruction improved fatty acid quantification, although this effect was relatively small for the numbers of iterations considered in this work. Furthermore, reconstructions with 50 iterations encountered errors more frequently and required longer reconstruction times. Increasing the number of basis functions used in the BCS reconstruction from $r = 25$ to 45 also had little impact on fat quantification results, as shown in Figure 3.12.

Given in Figure 3.13 are the results of performing the BCS reconstruction while varying the reconstruction parameter, λ . Small values of λ resulted in reconstructions with a significant amount of residual noise-like aliasing. As λ was increased more of this noise-like aliasing was removed in the reconstruction.

Given in Figure 3.18 are the results of performing BCS reconstructions with varying scale, s . In this case, large scaling factors resulted in increased noise in the reconstruction, while reconstructions done with smaller scaling factors were less likely to pick out the small fat peaks. In the case of $s = 0.5$, the entirety of the fat signal was attributed to the largest fat peak (methylene, Peak 5), except in the case of the 100% soybean oil tube.

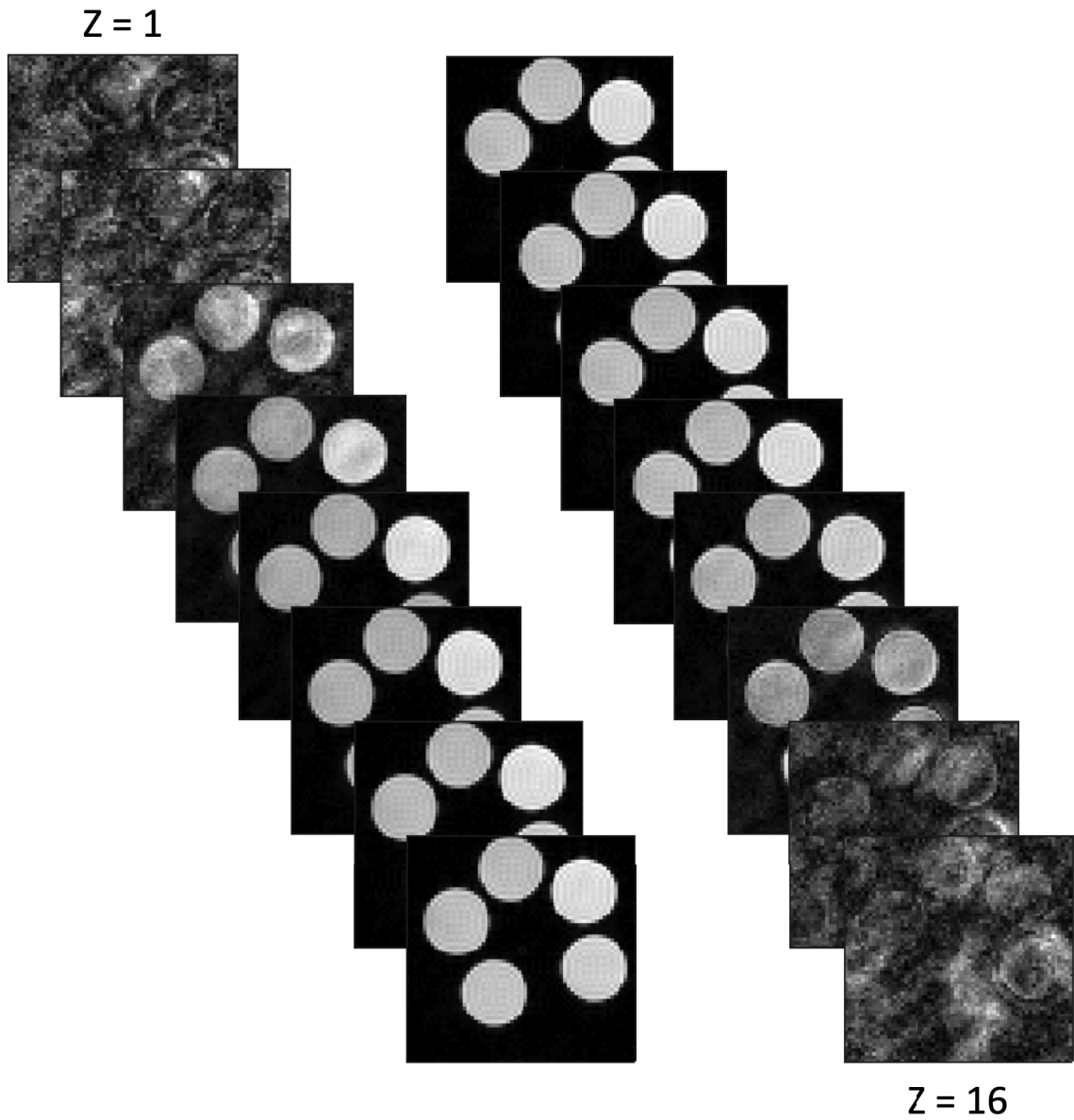


Figure 3.10: Slices ($Z = 1 \dots 16$) of the fully sampled preclinical 3D SE-SPI (one timepoint) of the soybean oil phantoms used to investigate the impact of changing BCS reconstruction parameters on fat composition quantification.

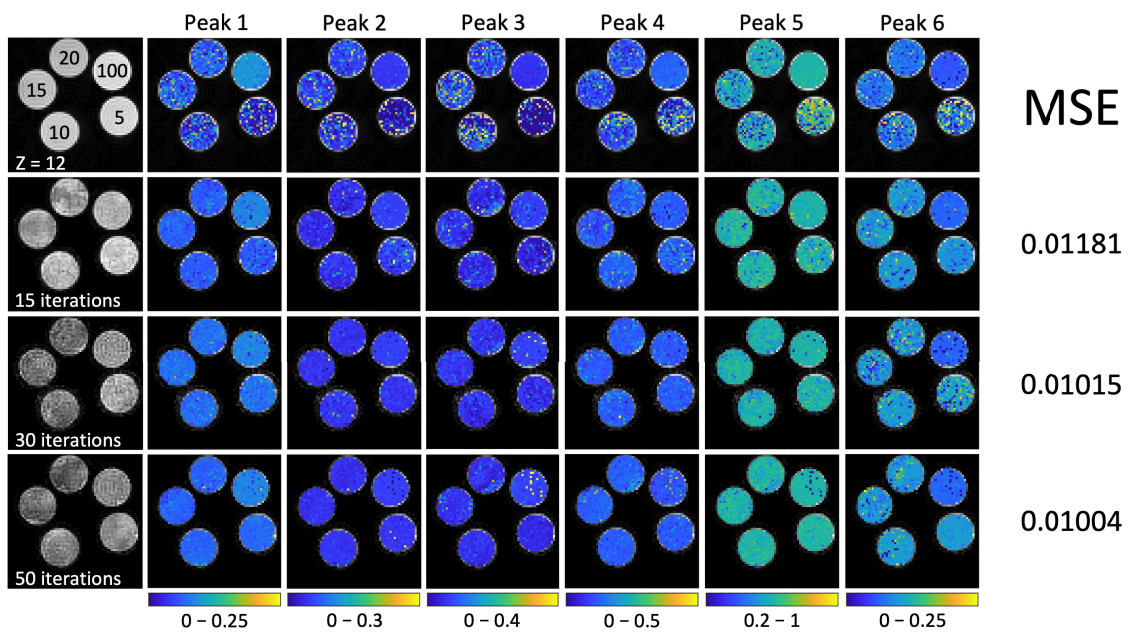


Figure 3.11: Maps (slice $Z = 12$) of relative peak amplitudes for fat peaks 1-6 as calculated from the 12th slice of the fully sampled preclinical 3D SE-SPI (top row), as well as those calculated from retrospectively accelerated scans ($R = 5.5$) with varying numbers of iterations ($n_{iter} = 15, 30, 50$). Remaining BCS parameters used are as given in Table 3.4.

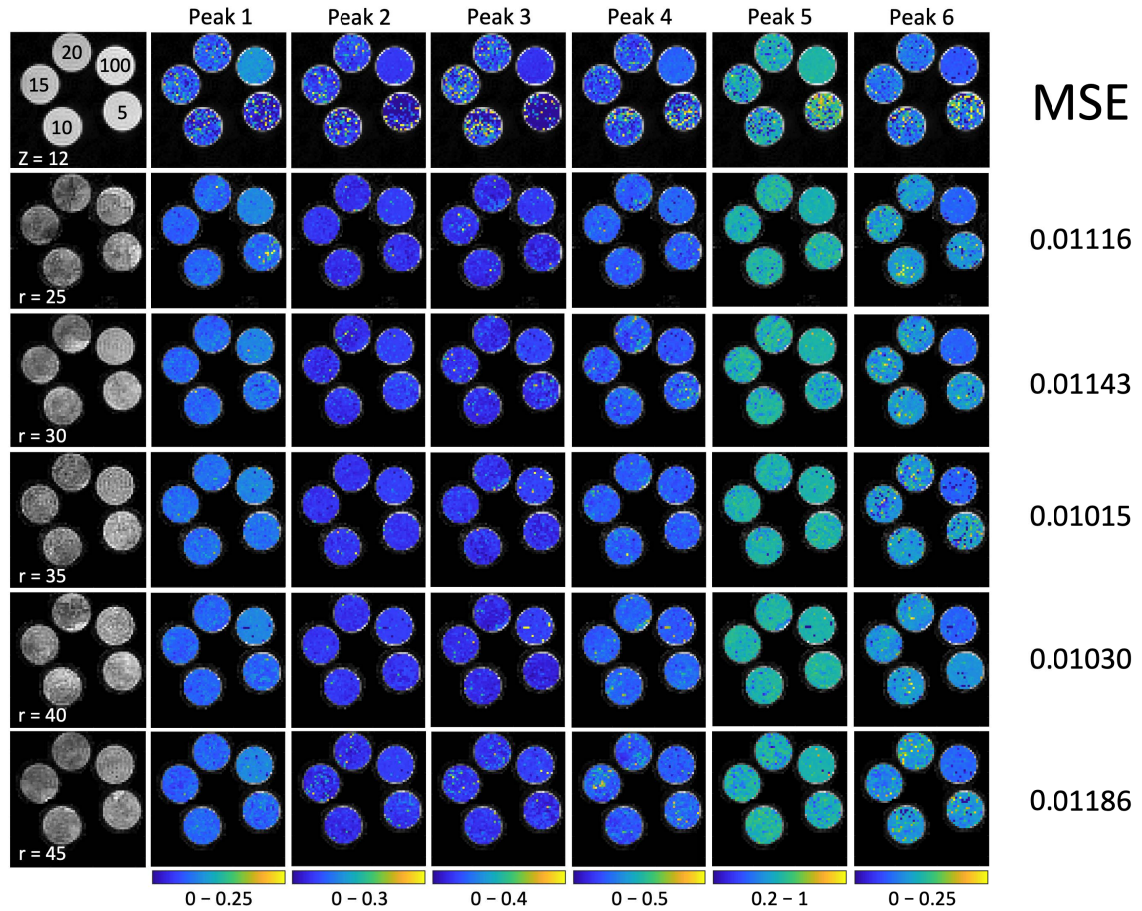


Figure 3.12: Maps (slice $Z = 12$) of relative peak amplitudes for fat peaks 1-6 as calculated from the 12th slice of the fully sampled preclinical 3D SE-SPI (top row), as well as those calculated from retrospectively accelerated scans ($R = 5.5$) with varying numbers of basis functions ($r = 25, 30, 35, 40, 45$). Remaining BCS parameters used are as given in Table 3.4.

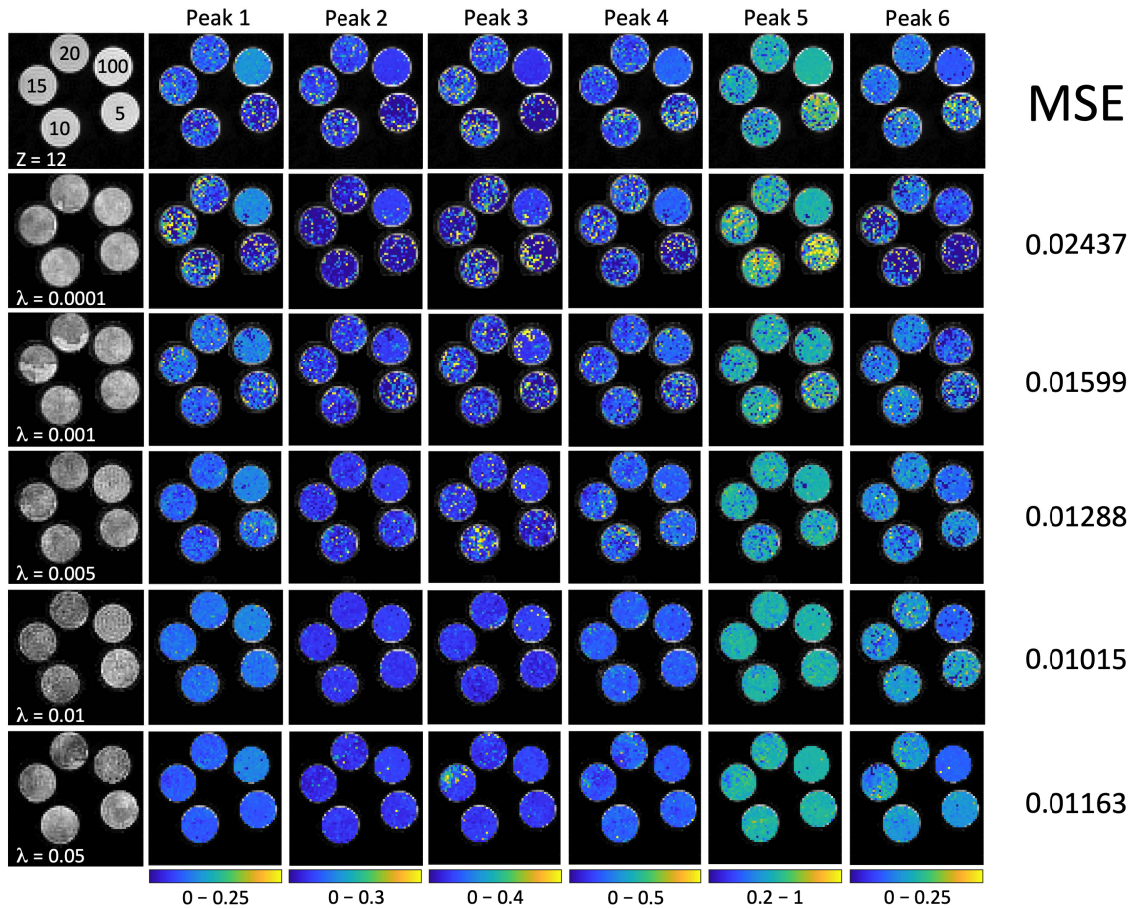


Figure 3.13: Maps (slice $Z = 12$) of relative peak amplitudes for fat peaks 1-6 as calculated from the 12th slice of the fully sampled preclinical 3D SE-SPI (top row), as well as those calculated from retrospectively accelerated scans ($R = 5.5$) with varying regularization parameters ($\lambda = 0.0001, 0.001, 0.005, 0.01, 0.05$). Remaining BCS parameters used are as given in Table 3.4.

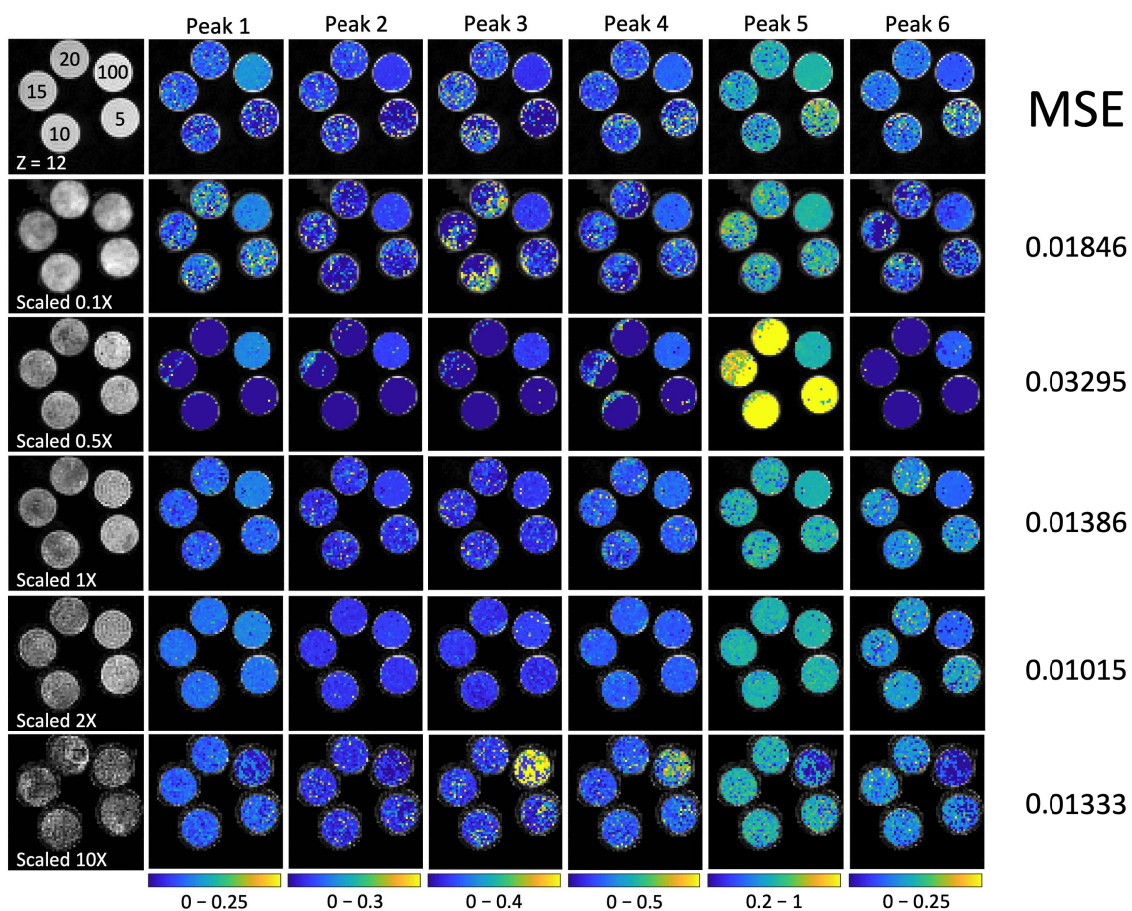


Figure 3.14: Maps of relative peak amplitudes for fat peaks 1-6 as calculated from the 12th slice of the fully sampled preclinical 3D SE-SPI (top row), as well as those calculated from retrospectively accelerated scans ($R = 5.5$) with varying scaling factors ($s = 0.1, 0.5, 1, 2, 10$). Remaining BCS parameters used are as given in Table 3.4.

Given the frequent occurrence of errors in BCS reconstructions done with 50 iterations, and the similarity in fat composition quantification to those done with 30 iterations, as shown in Figure 3.11, only those reconstructions done using $n_{iter} = 15, 30$ were considered. The combination of reconstruction parameters which minimized the MSE in relative fat peak amplitudes relative to the fully sampled scan, as measured using the preclinical system, are summarized in Table 3.4. This set of parameters was thus used for the analysis of all CS results in this work.

Table 3.4: BCS parameters, namely the number of iterations, n_{iter} , number of basis functions, r , regularization parameter, λ , and scaling factor, s , which minimized the MSE in relative fat peak amplitudes between the fully sampled preclinical 3D dataset and that retrospectively accelerated by a factor of $R = 5.5$.

Parameter	Value
n_{iter}	30
r	35
λ	0.01
s	2

Maps of relative fat peaks amplitudes, as measured with the clinical system, reconstructed with varying BCS parameters are given in Figures 3.15-3.18. As was the case with the preclinical data, BCS reconstructions done with 50 iterations commonly encountered errors during reconstruction. MSE results were, on average, smaller by one order of magnitude than those seen with the preclinical soybean oil tubes of varying fat fraction. For the most part, compared with preclinical results, varying these parameters did not produce a visible change in the resulting fat peak amplitudes. One exception to this rule is the reconstruction performed using a scaling factor of $s = 0.1$, shown in Figure 3.18. In this case, fat signal seems to have been misattributed to the methene peak (Peak 6). Nonetheless, as the results shown here do not suggest a preferred set of reconstruction parameters, those parameters given in Table 3.4 were also used for the clinical results of this work.

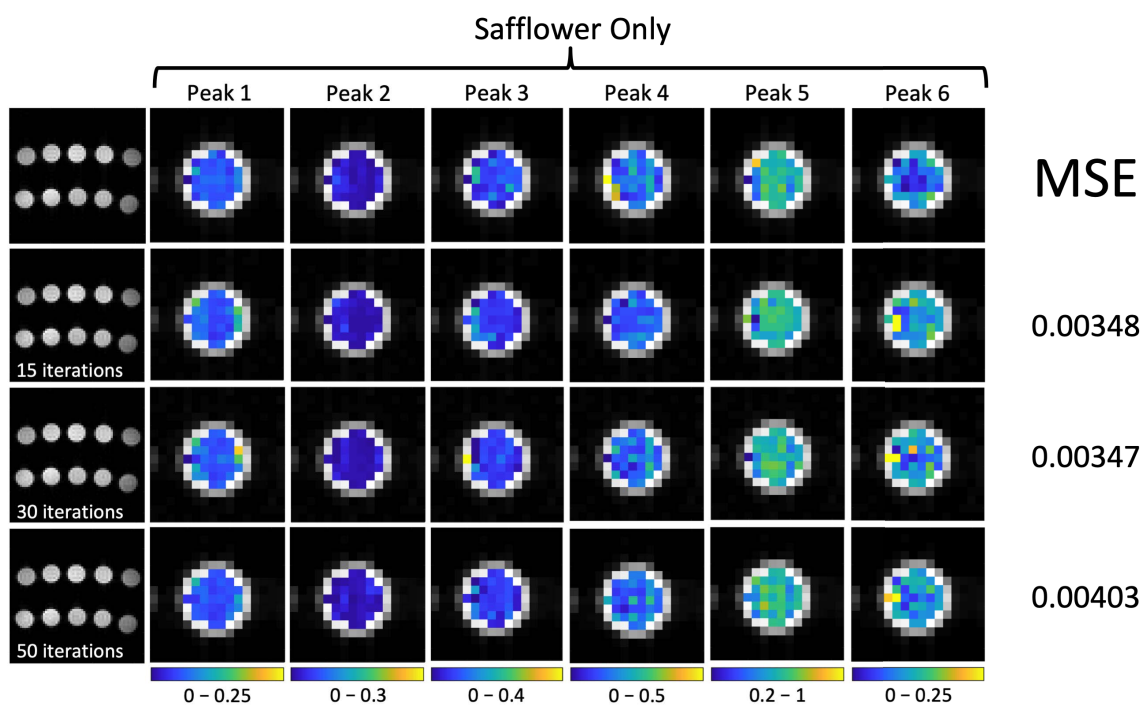


Figure 3.15: (Top) Fully sampled clinical 2D SE-SPI of the pure oil tubes (top row, from left to right are the soybean, sesame, safflower, peanut, and flax oil tubes) and soybean oil emulsions (bottom row, from left to right are 0%, 5%, 10%, 15%, and 20% soybean oil), along with maps of relative peak amplitudes for the safflower tube. Remaining rows are those generated from retrospectively accelerated scans ($R = 3$) with varying numbers of iterations ($n_{iter} = 15, 30, 50$). Remaining BCS parameters used are as given in Table 3.4.

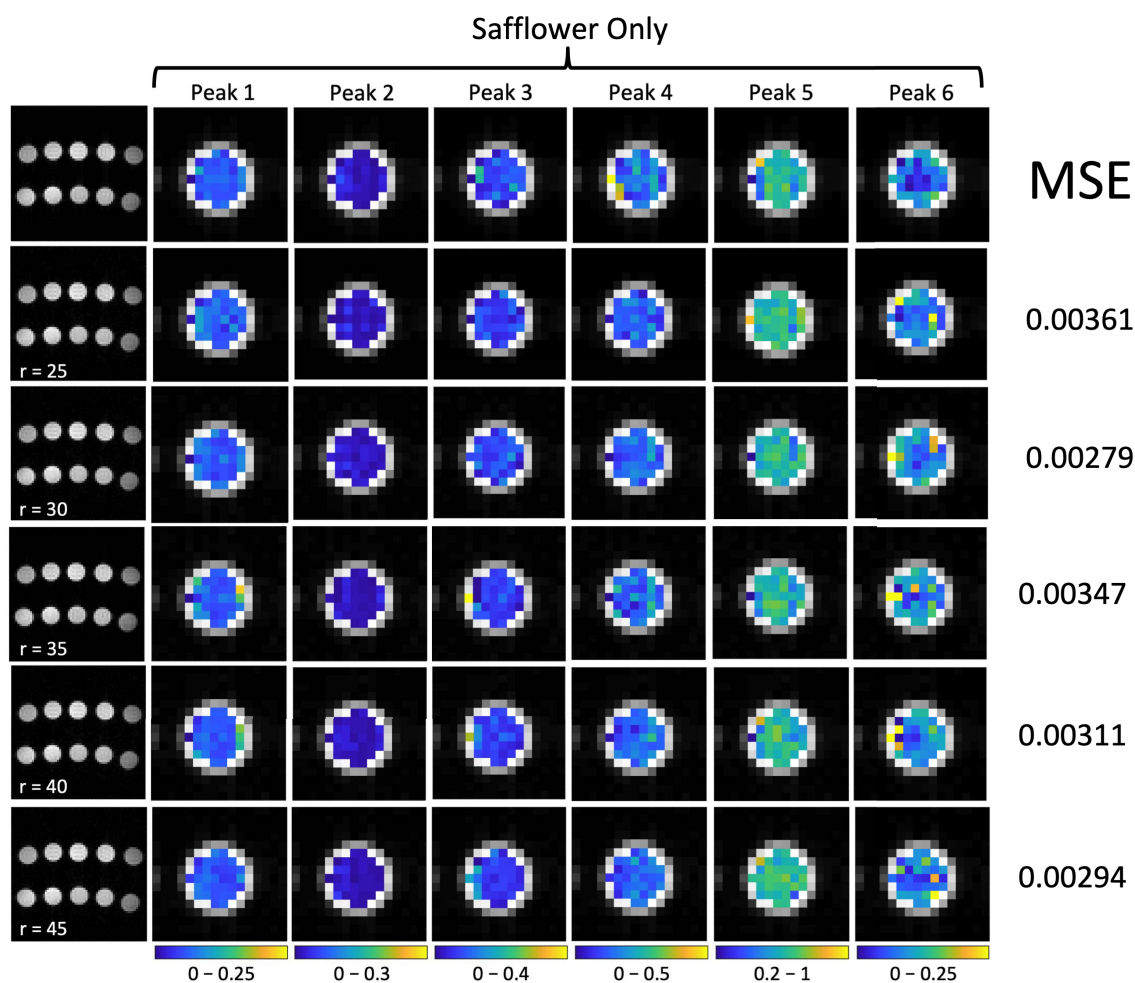


Figure 3.16: (Top) Fully sampled clinical 2D SE-SPI of the pure oil tubes (top row, from left to right are the soybean, sesame, safflower, peanut, and flax oil tubes) and soybean oil emulsions (bottom row, from left to right are 0%, 5%, 10%, 15%, and 20% soybean oil), along with maps of relative peak amplitudes for the safflower tube. Remaining rows are those generated from retrospectively accelerated scans ($R = 3$) with varying numbers of basis functions ($r = 25, 30, 35, 40, 45$). Remaining BCS parameters used are as given in Table 3.4.

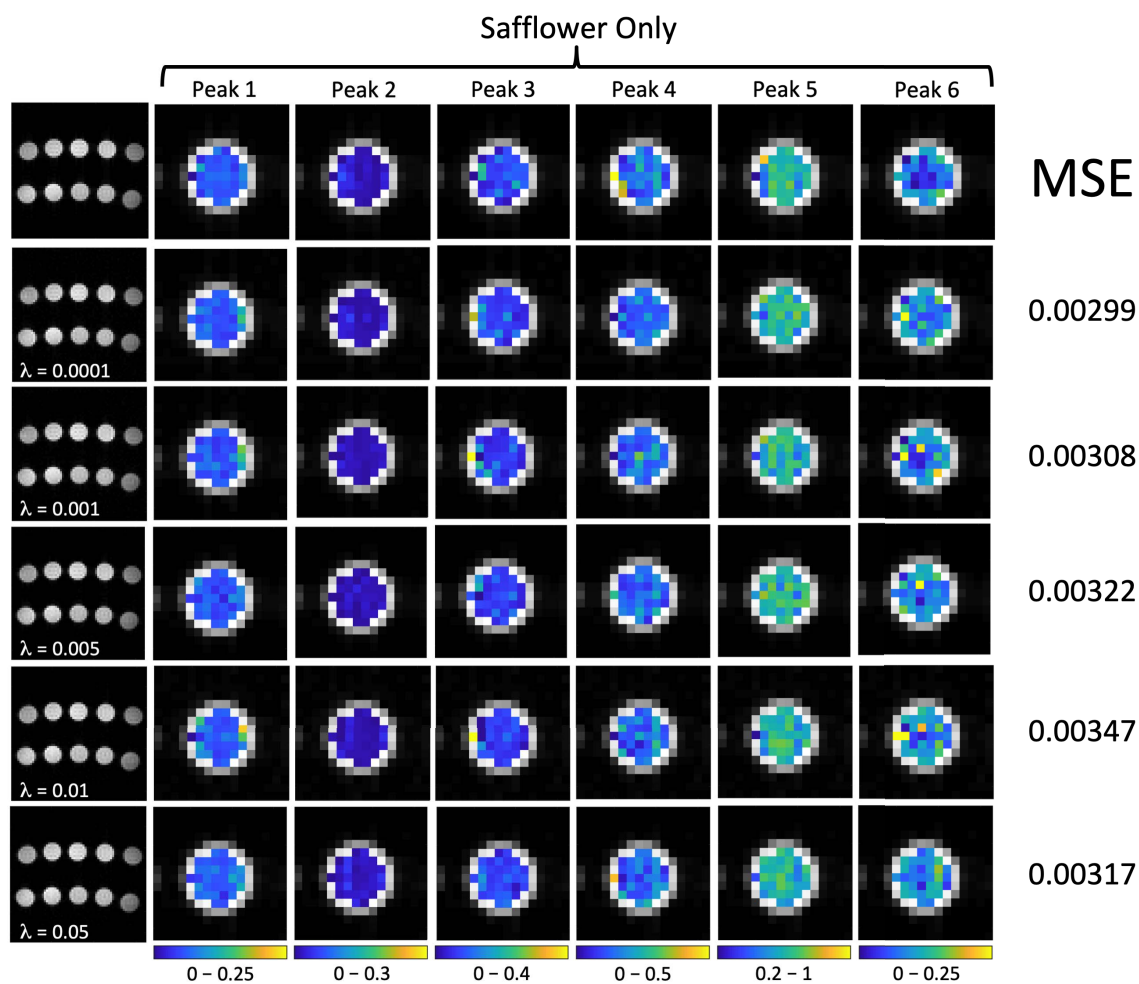


Figure 3.17: (Top) Fully sampled clinical 2D SE-SPI of the pure oil tubes (top row, from left to right are the soybean, sesame, safflower, peanut, and flax oil tubes) and soybean oil emulsions (bottom row, from left to right are 0%, 5%, 10%, 15%, and 20% soybean oil), along with maps of relative peak amplitudes for the safflower tube. Remaining rows are those generated from retrospectively accelerated scans ($R = 3$) with varying regularization parameters ($\lambda = 0.0001, 0.001, 0.005, 0.01, 0.05$). Remaining BCS parameters used are as given in Table 3.4.

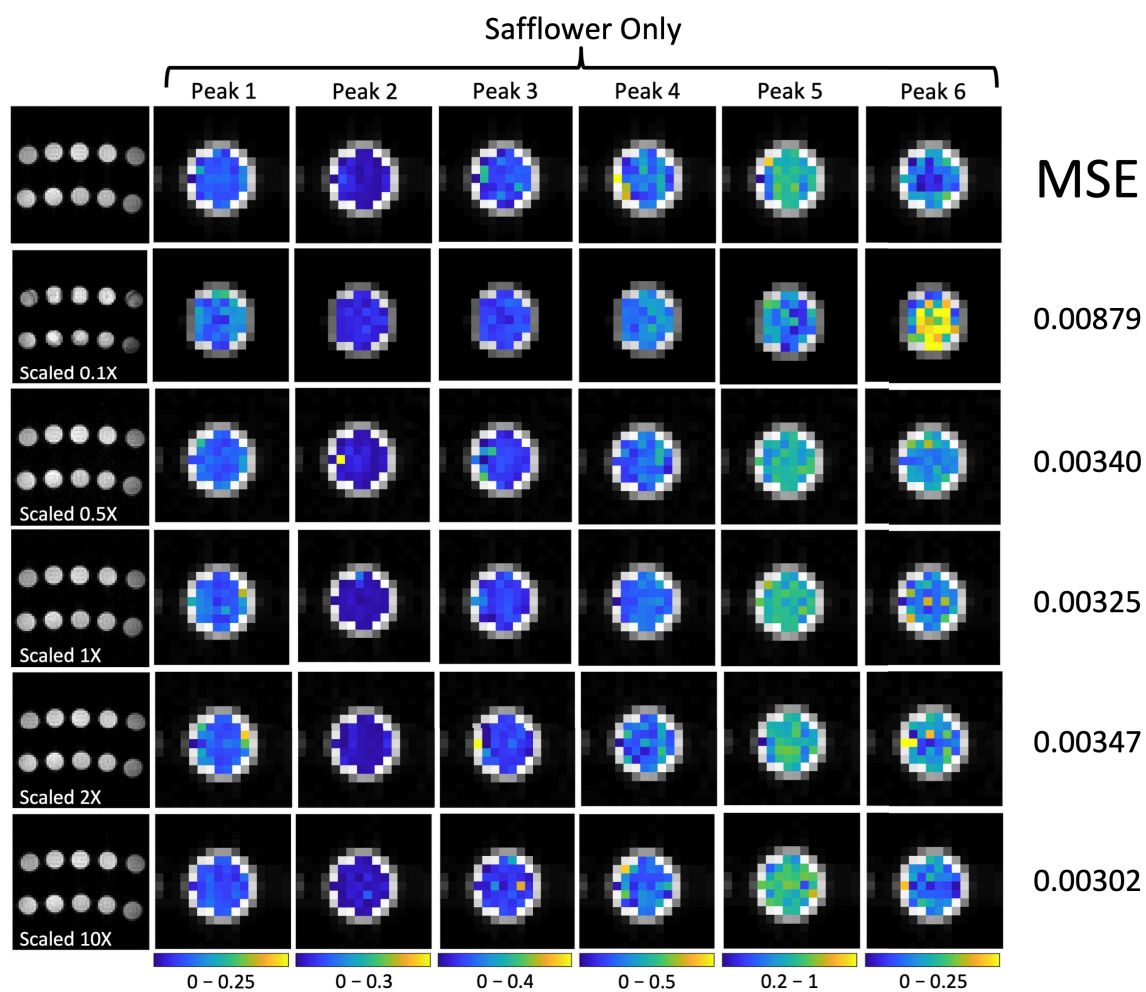


Figure 3.18: (Top) Fully sampled clinical 2D SE-SPI of the pure oil tubes (top row, from left to right are the soybean, sesame, safflower, peanut, and flax oil tubes) and soybean oil emulsions (bottom row, from left to right are 0%, 5%, 10%, 15%, and 20% soybean oil), along with maps of relative peak amplitudes for the safflower tube. Remaining rows are those generated from retrospectively accelerated scans ($R = 3$) with varying scaling factors ($s = 0.1, 0.5, 1, 2, 10$). Remaining BCS parameters used are as given in Table 3.4.

3.6 Discussion

3.6.1 Choice of Parameters: Spectral Analysis

For this work, spectra were processed using an HSVD-based binning algorithm. As the assumed number of components, N , in this decomposition can influence spectral quantification, it is important to consider what number is most appropriate for the application of interest [75]. While this work was concerned with six main fat peaks and the water peak, when applicable, more components are required in order to accurately model the spectrum. For one, additional fat peaks are present, such as those located from 4.0 – 4.3 ppm, as shown in Figures 4.2 and 4.6. While these peaks are not considered for this work, no such prior knowledge can be input into the HSVD, and so must be taken into account in choosing N . Furthermore, variations in B_0 cause these MRS signals to deviate from the Lorentzian form assumed in Equation 2.22, meaning certain peaks may be modelled with more than one component [76]. As such, $10 \leq N \leq 30$ components were considered for this work.

In the case of the preclinical soybean oil emulsions, results presented in Figure 3.7, assuming too few components resulted in many of the smaller fat peaks being missed entirely ($N < 20$), or introduced more intrasession variability ($20 \leq N \leq 23$), likely a result of inadequate modelling of these small fat peaks, as shown in Figure 3.5A. However, assuming too many components ($N > 25$) allowed more noise to be included in the model, also a source of intrasession variability. Assuming 25 HSVD components appears appropriate for this application. Without the presence of the water peak, as was the case for the pure oil tubes, fewer components ($N \approx 14$) were required to accurately model the spectrum, and including more components simply included more noise in the model, as shown by the clinical pure oil results in Figure 3.8. However, given that no prior knowledge of FF was assumed for *in vivo* applications, 25 components were assumed in analyzing the preclinical data, regardless of fat fraction. On the other hand, as phantom experiments with the clinical system were limited to the pure oil tubes, 14 components were assumed in this case. For future applications analyzing spectra containing a water signal, more components will likely be required.

3.6.2 Choice of Parameters: Compressed Sensing Reconstruction

SE-SPI, being an inherently slow imaging technique, was accelerated in this work using BCS. As with typical CS implementations, the choice of regularization parameter, λ , affects the performance of this reconstruction. Namely, larger values of λ reduce the degree of noise in the recovered images, but may also result in the loss of low contrast features [57, 58]. This noise reduction with increasing λ is apparent from the preclinical results in Figure 3.13; MSE was minimized by using $\lambda = 0.01$. Clinical results, on the other hand, showed little dependence on the regularization parameter, as shown in Figure 3.17. In general, the clinical results seemed less dependent on reconstruction parameters, likely due to the smaller acceleration factor ($R = 3$ as opposed to $R = 5.5$), as well as the fact that they were limited to the pure oil tubes.

In addition to the regularization parameter, BCS introduces another reconstruction parameter, that being the number of basis functions, r . Assuming too few basis functions has been shown to result in inadequate modelling of signal, but since they are estimated from the data itself, the number of basis functions is inherently limited by the amount of data collected. Studies using BCS for acceleration of cardiac imaging have shown that reconstruction errors generally decrease with increasing numbers of basis functions, stabilizing at around $r = 20$ [57]. However, given the difference in temporal behaviour of signal for this work, varying numbers of basis functions ($r = 25, 30, 35, 40, 45$) were investigated. Visually, the relative fat peak amplitudes did not seem to be largely affected by changing the number of basis functions in this range as shown for the preclinical and clinical phantom studies in Figures 3.12 and 3.16, respectively. Since $r = 35$ minimized the MSE for the preclinical results, 35 basis functions were used for this work.

Two last parameters were investigated for this work, the first being the number of iterations used in optimizing the minimization problem posed in Equation 2.21. Although not apparent from the relative fat peak amplitude maps in Figures 3.11 and 3.15, increasing the number of iterations from 15 to 30 generally reduced the MSE. However, reconstructions using 50 iterations commonly encountered errors; thus, $n_{iter} = 30$ was chosen for this work.

The scale of the input data, Y , was also observed to impact reconstruction quality. As portrayed by the preclinical results in Figure 3.14, using larger scaling factors

resulted in noisy images, while reconstructions done with smaller scaling factors had the potential to miss low contrast features, exemplified by the $s = 0.5$ case in Figure 3.14. These results are what would be expected of CS reconstructions performed with too small or too large a regularization parameter, respectively, and may be explained using Equation 2.21; essentially, upscaling of the undersampled k-space data, Y , can reduce the relative weighting of λ , and vice versa. Nonetheless, since a scaling factor of 2 clearly minimized the MSE relative to the fully sampled preclinical scan, $s = 2$ was chosen for this work. As with the aforementioned reconstruction parameters, the clinical scans shown in Figure 3.18 were not visibly affected by changes in scale, except in the case of very small scaling factors.

It should be noted that these phantom setups were limited in the number of oils present and that samples were contained within discrete tubes, a more ‘sparse’ set-up, both temporally and spatially, than *in vivo* applications. Nonetheless, these results do demonstrate the unreliability of certain combinations of reconstruction parameters. In the most extreme example shown, that scaled by a factor of $s = 0.5$ in Figure 3.14, it can be seen that all of the smaller fat peaks are missed in the soybean oil emulsions, and the entirety of the fat signal attributed to the largest peak, methylene (Peak 5).

Chapter 4

Phantom Validation

4.1 Methods

Having finalized the post processing pipeline, the agreement between PRESS measurements and those made using SE-SPI was assessed for the pure oil tubes, and, for the preclinical experiments, the soybean oil tubes of varying fat fraction. While measures of fat composition are the focus of this work, the fat fractions of the set of soybean oil tubes are an important measure of aliasing in the CS SE-SPI results.

With the preclinical system, five fully sampled 2D SE-SPIs of each oil tube set (either the five soybean oil tubes of varying fat fraction or the five pure oil tubes) were acquired, taking 13.5 minutes each. With the clinical system, four fully sampled 2D SE-SPIs of the pure oil tube set were acquired using the multichannel head coil. Since PRESS acquisition parameters could not be matched to those intended for clinical SE-SPI acquisition, the SE-SPIs were acquired using $TR/TE = 250/29$ ms, $BW = 4$ kHz, $FOV = 20 \times 20 \times 1$ cm, a 64×64 matrix, and 512 points acquired at each readout. For comparison with preclinical results, three SE-SPIs were acquired with acquisition parameters matched to those intended for clinical implementation.

In all cases, the fat fraction, fat peak amplitudes, and fat composition metrics UI , UIs , and PUI as measured using SE-SPI were averaged over voxels falling within the PRESS volume. SE-SPI agreement was assessed for fully sampled scans, as well as retrospectively accelerated and BCS reconstructed data. The retrospective under-sampling factors used were $R = 5.5$ and $R = 3$ for data acquired with the preclinical and clinical systems, respectively.

All statistical comparisons were made using Welch’s t-test, also referred to as an unequal variances t-test, with $p < 0.05$ considered significant. Welch’s t-test was chosen over the conventional t-test as it has been shown to be more robust to Type I errors (false positives) for small sample sizes with unequal variances, unequal sample sizes, and/or certain degrees of skewness from a normal distribution. However, it is

important to note that Welch's t-test has less statistical power than the conventional t-test in these cases, corresponding to an increased likelihood of Type II errors (false negatives) [77].

4.2 Results

Fat fraction results for the preclinical soybean oil emulsions are shown in Figure 4.1. CS SE-SPI FF measurements of the 5% and 100% soybean tubes appeared to be slightly affected by uncorrected aliasing, as indicated by the respective increase and decrease in FF compared to PRESS and fully sampled SE-SPI measurements, but not to a large degree. The remaining tubes were unaffected.

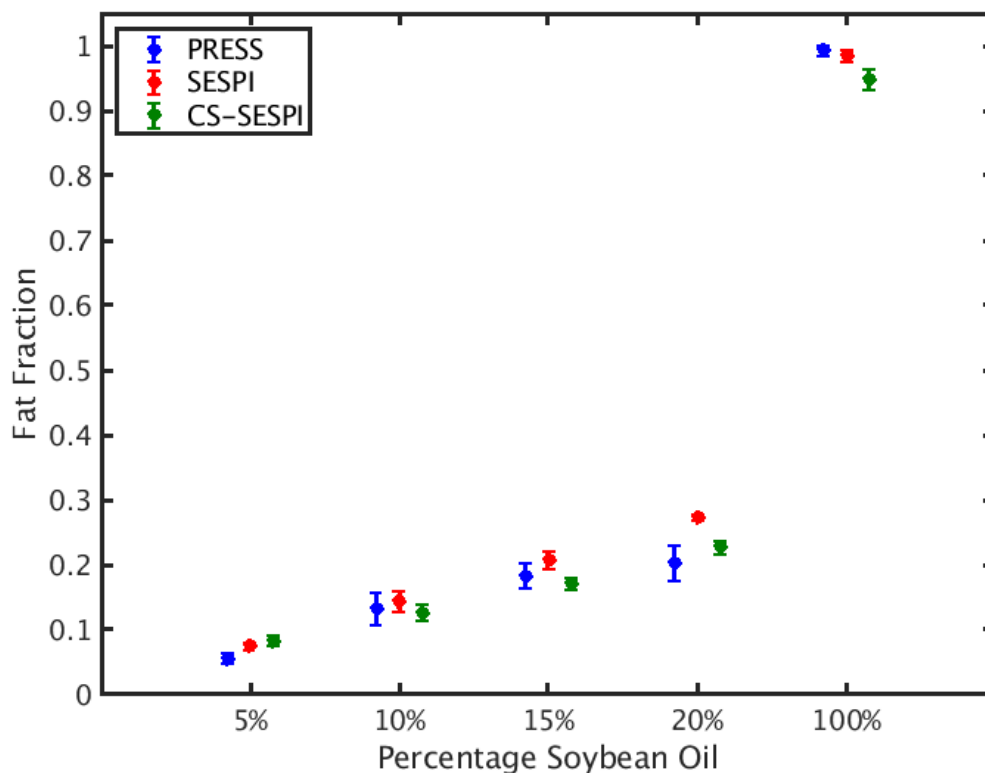


Figure 4.1: Fat fractions (mean \pm 95% CI over five scans) for the 5%, 10%, 15%, 20%, and 100% soybean oil tubes as measured using PRESS, fully sampled SE-SPI, and retrospectively accelerated ($R = 5.5$) CS SE-SPI on the preclinical system.

Shown in Figure 4.2 are the relative fat peak amplitudes calculated from 5 scans of this soybean oil phantom, along with raw spectra acquired from the 100% soybean oil

tube. Given that raw spectra were unphased prior to the HSVD-based fitting, these spectra were chosen to provide a good visualization of the fat peaks of interest, and are not necessarily representative. The effect of residual aliasing in retrospectively accelerated CS SE-SPI results was clear from the presence of a water peak in the spectrum in Figure 4.2A. A smaller water peak was also present in the fully sampled SE-SPI spectrum, likely a result of intervoxel contamination, as there should be no aliasing in this case. In general, CS SE-SPI measures of these peak amplitudes agreed with PRESS.

Shown in Figure 4.3 are the corresponding indices, UI, UIs, and PUI, as calculated using Equations 2.13, 2.14, and 2.15, respectively, averaged over five scans of the soybean oil phantom (SE-SPI ROIs were limited to the region covered by the PRESS voxel). Also shown are lipid composition maps derived from one of the SE-SPIs. With smaller fat fractions there was a clear increase in variation in these fat composition metrics, as expected based on the increase in variation in fat peak amplitudes.

Given in Figure 4.4 are the same indices for 5 scans of the pure oil phantom with the preclinical system, processed assuming $N = 25$ components. As was the case for soybean oil, PRESS measurements of lipid composition were, in general, in agreement with CS SE-SPI results, with the notable exception of UI for the flax oil tube. This underestimation was a result of the underestimation of Peak 1 and overestimation of Peak 5 as seen from Figure 4.5B. Nonetheless, trends in fat composition appeared consistent across the techniques. Furthermore, differences in lipid composition were observed in a single scan, as shown by the fat maps also given in Figure 4.4. These fat composition measures were fairly homogeneous within a single tube, aside from voxels for which the necessary fat peaks for computation of these indices (e.g. Peak 2 for PUI) were not identified during spectral decomposition.

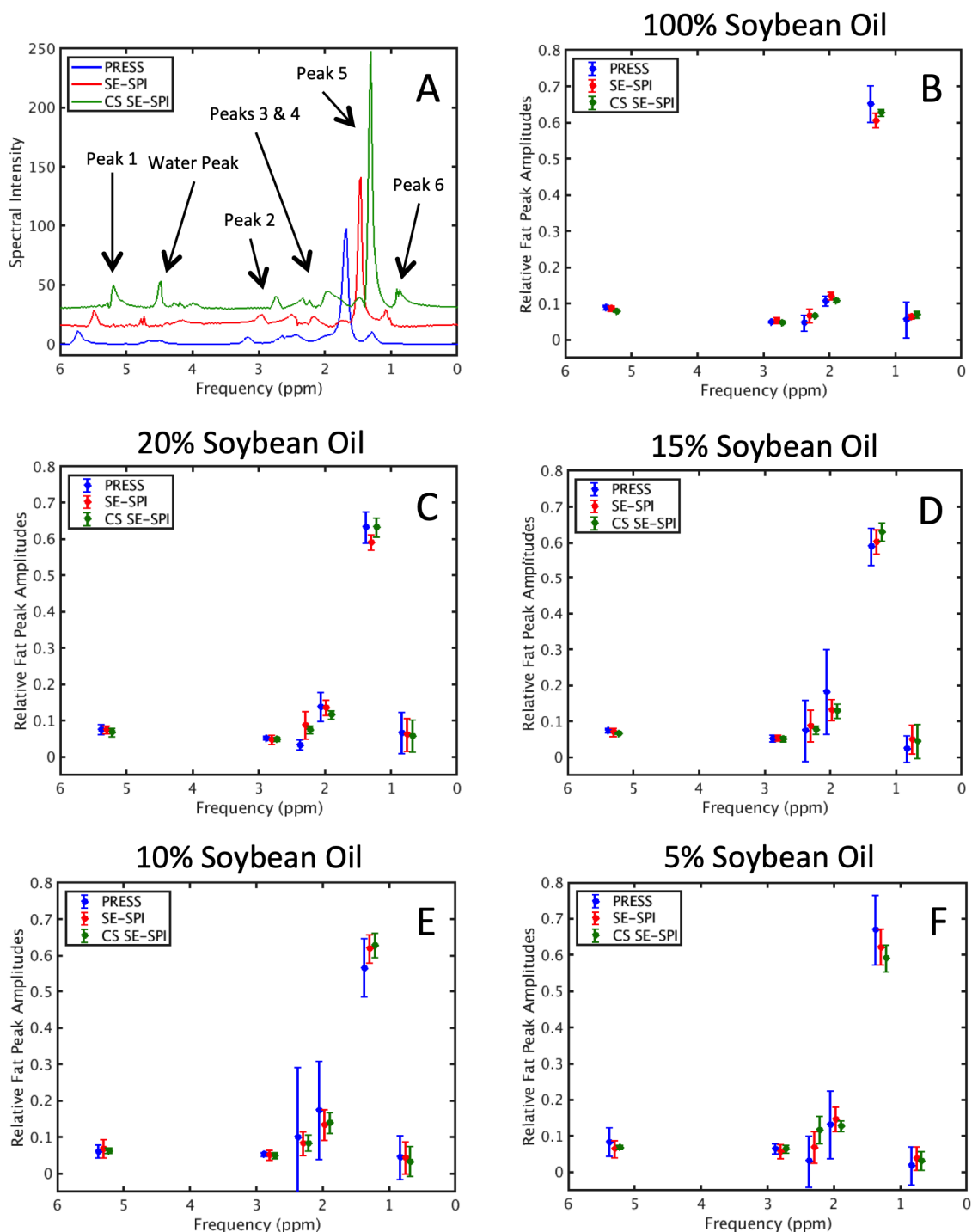


Figure 4.2: (A) 100% soybean spectra acquired using preclinical PRESS, SE-SPI (showing results for a single voxel), and retrospectively accelerated ($R = 5.5$) CS SE-SPI, offset for clarity. (B-F) Relative peak amplitudes of the six fat peaks (mean \pm 95% CI over five scans, plotted at their corresponding frequencies, offset for clarity) for the soybean oil tubes of varying fat fraction as measured using preclinical PRESS, fully sampled SE-SPI, and retrospectively accelerated ($R = 5.5$) CS SE-SPI.

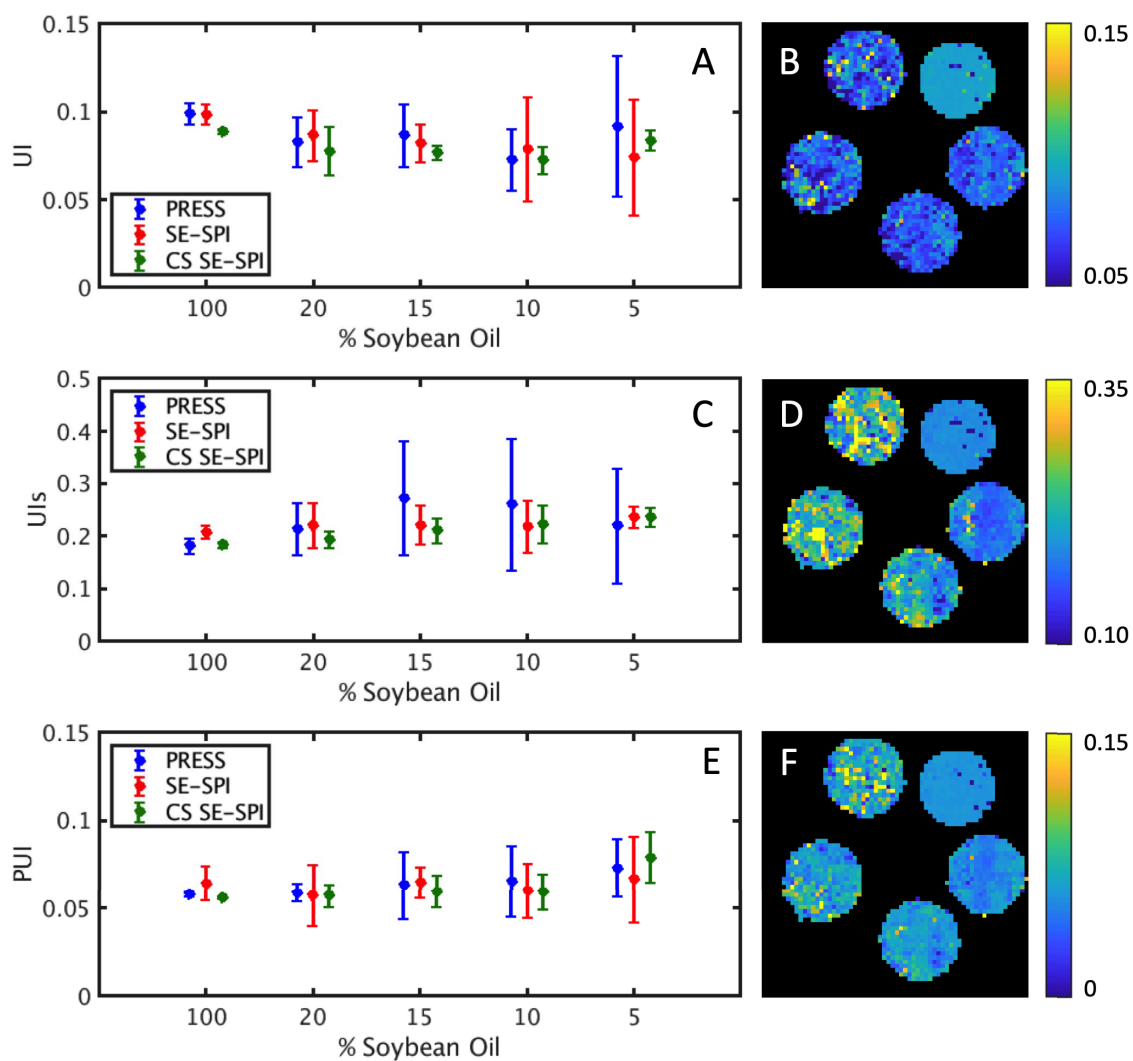


Figure 4.3: (A, C, E) Unsaturation (UI), surrogate unsaturation (UIs), and polyunsaturation (PUI) indices (mean \pm 95% CI over five scans) for the 100%, 20%, 15%, 10%, and 5% soybean oil tubes as measured using preclinical PRESS, fully sampled SE-SPI, and retrospectively accelerated ($R = 5.5$) CS SE-SPI. (B, D, F) Maps of UI, UIs, and PUI, respectively, for one retrospectively accelerated preclinical CS SE-SPI of the soybean oil phantom. Clockwise, starting from the top right, are the 100%, 20%, 15%, 10%, and 5% soybean oil tubes.

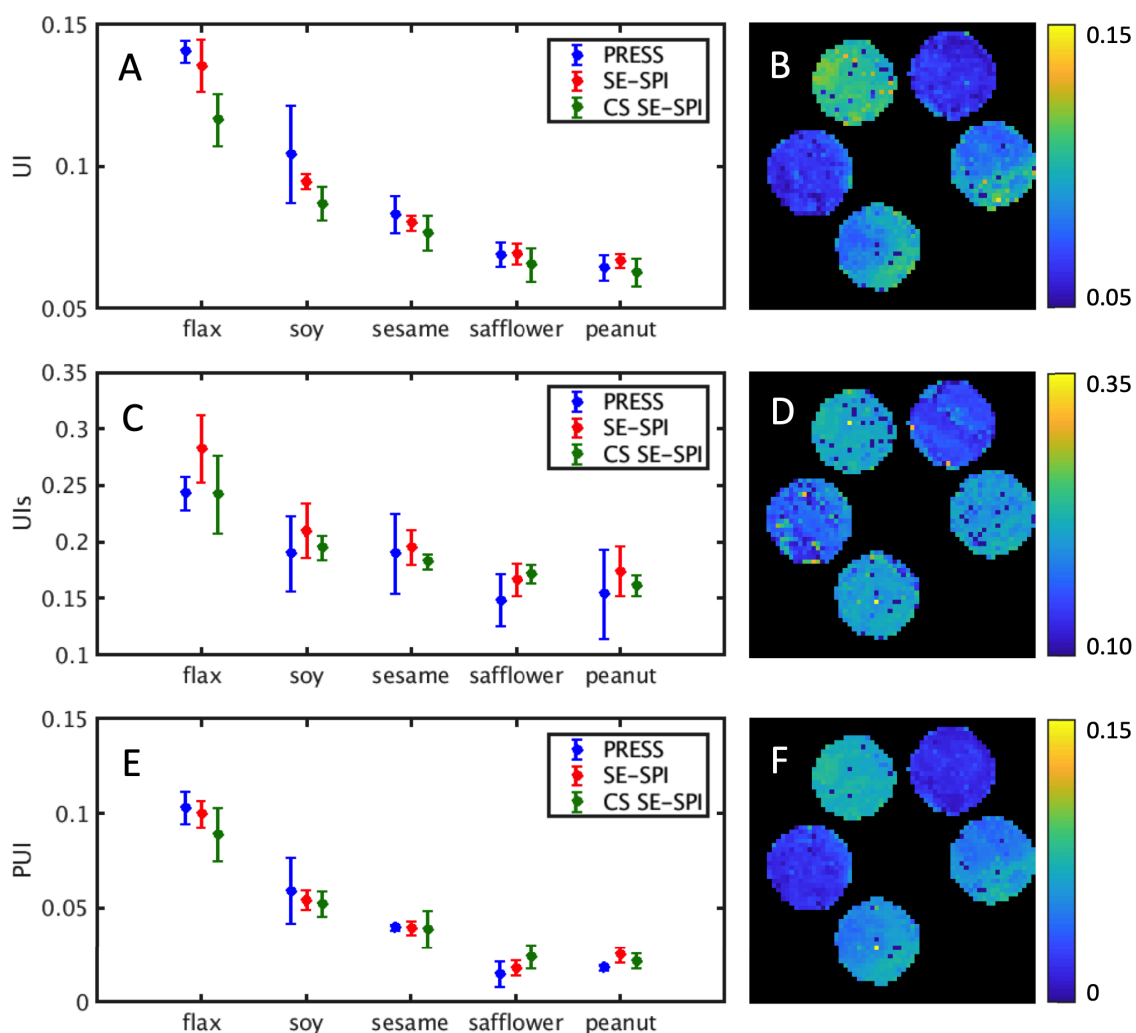


Figure 4.4: (A, C, E) Unsaturation (UI), surrogate unsaturation (UIs), and polyunsaturation (PUI) indices (mean \pm 95% CI over five scans) for the flax, soybean, sesame, safflower, and peanut oil tubes as measured using preclinical PRESS, fully sampled SE-SPI, and retrospectively accelerated ($R = 5.5$) CS SE-SPI. (B, D, F) Maps of UI, UIs, and PUI, respectively, for one retrospectively accelerated preclinical CS SE-SPI of the pure oil phantom. Clockwise, starting from the top left, are the flax, peanut, sesame, soy, and safflower oil tubes.

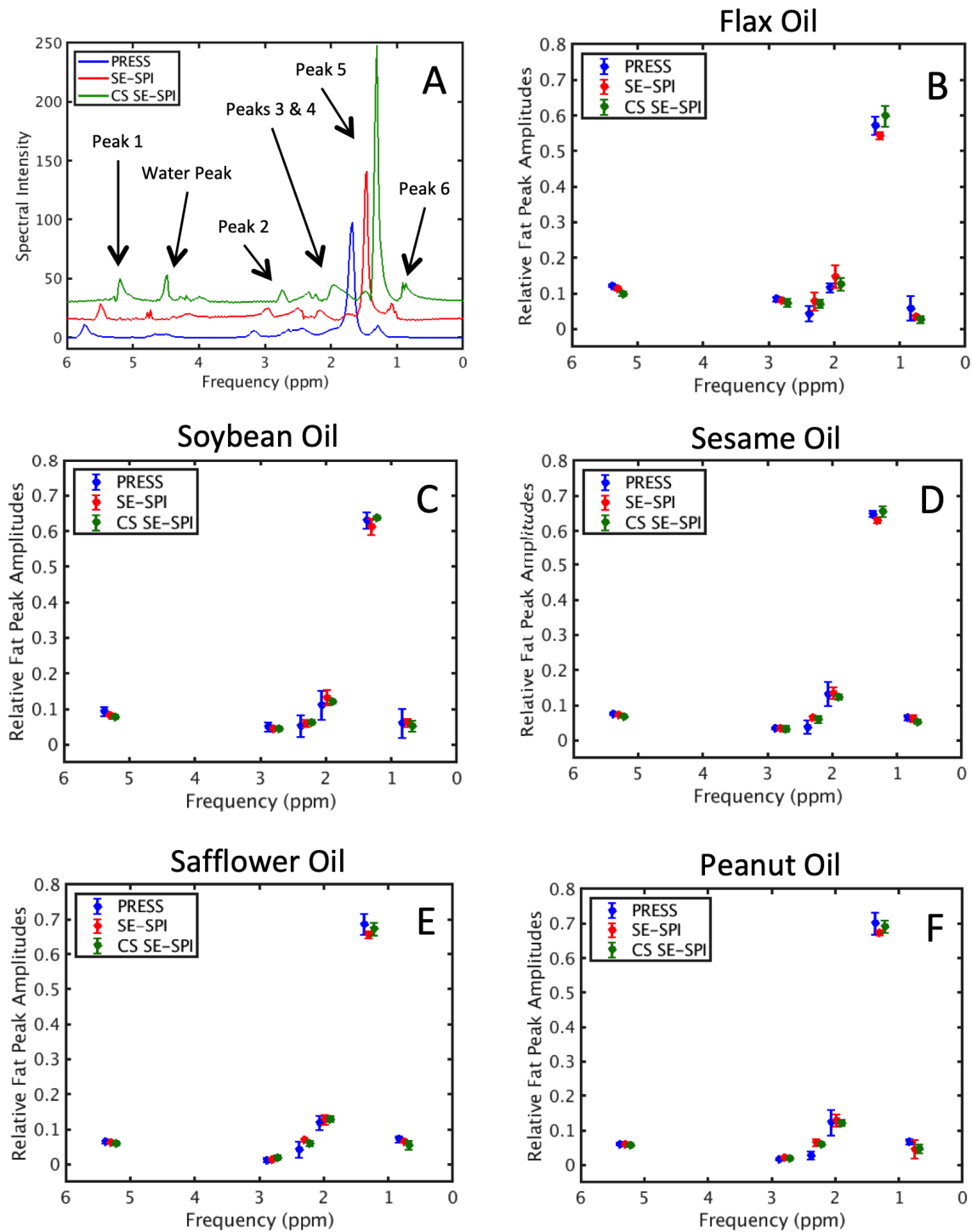


Figure 4.5: (A) 100% soybean spectra acquired using preclinical PRESS, SE-SPI (showing results for a single voxel), and retrospectively accelerated ($R = 5.5$) CS SE-SPI, offset for clarity. (B-F) Relative peak amplitudes of the six fat peaks (mean \pm 95% CI over 5 scans, plotted at their corresponding frequencies, offset for clarity) for the pure oil tubes as measured using preclinical PRESS, fully sampled SE-SPI, and retrospectively accelerated ($R = 5.5$) CS SE-SPI.

Given in Tables 4.1, 4.2, and 4.3 are the results of Welch’s t-test comparing the unsaturation indices of the five oils using PRESS, fully sampled SE-SPI, and CS-SESPI, respectively. Using PRESS, significant differences (defined as $p < 0.05/4$ using the Bonferroni correction for multiple comparisons) were observed between all of the oils except when comparing peanut to safflower, and soy to sesame. This was also the case for UI calculated using SE-SPI, both fully sampled and accelerated, except that in these cases the differences in UI between the soy and sesame were significant.

Table 4.1: Preclinical results of Welch’s t-test comparing the unsaturation indices (UI) of the various pure oil tubes, as measured using PRESS.

	Flax	Soy	Sesame	Safflower	Peanut
Flax	NA	$p = 0.003$	$p < 0.001$	$p < 0.001$	$p < 0.001$
Soy	NA	NA	$p = 0.022$	$p = 0.004$	$p = 0.002$
Sesame	NA	NA	NA	$p = 0.002$	$p < 0.001$
Safflower	NA	NA	NA	NA	$p = 0.072$
Peanut	NA	NA	NA	NA	NA

Table 4.2: Preclinical results of Welch’s t-test comparing the unsaturation indices (UI) of the various pure oil tubes, as measured using fully sampled SE-SPI.

	Flax	Soy	Sesame	Safflower	Peanut
Flax	NA	$p < 0.001$	$p < 0.001$	$p < 0.001$	$p < 0.001$
Soy	NA	NA	$p < 0.001$	$p < 0.001$	$p < 0.001$
Sesame	NA	NA	NA	$p < 0.001$	$p < 0.001$
Safflower	NA	NA	NA	NA	$p = 0.172$
Peanut	NA	NA	NA	NA	NA

Given in Tables 4.4, 4.5, and 4.6 are the results of Welch’s t-test comparing the surrogate unsaturation indices of the five oils using PRESS, fully sampled SE-SPI, and CS-SESPI, respectively. Using PRESS, the UIs of flax oil was significantly higher than that of all other oil types tested. The same was true for SE-SPI, and for CS SE-SPI with the exception of soybean oil (difference not significant). In some cases SE-SPI and CS SE-SPI measured significant differences between oils where PRESS did not.

Table 4.3: Preclinical results of Welch’s t-test comparing the unsaturation indices (UI) of the various pure oil tubes, as measured using retrospectively accelerated ($R = 5.5$) CS SE-SPI.

	Flax	Soy	Sesame	Safflower	Peanut
Flax	NA	$p < 0.001$	$p < 0.001$	$p < 0.001$	$p < 0.001$
Soy	NA	NA	$p = 0.010$	$p < 0.001$	$p < 0.001$
Sesame	NA	NA	NA	$p = 0.006$	$p = 0.001$
Safflower	NA	NA	NA	NA	$p = 0.346$
Peanut	NA	NA	NA	NA	NA

Table 4.4: Preclinical results of Welch’s t-test comparing the surrogate unsaturation indices (UIs) of the various pure oil tubes, as measured using PRESS.

	Flax	Soy	Sesame	Safflower	Peanut
Flax	NA	$p = 0.008$	$p = 0.010$	$p < 0.001$	$p = 0.002$
Soy	NA	NA	$p = 0.992$	$p = 0.025$	$p = 0.092$
Sesame	NA	NA	NA	$p = 0.030$	$p = 0.100$
Safflower	NA	NA	NA	NA	$p = 0.741$
Peanut	NA	NA	NA	NA	NA

Table 4.5: Preclinical results of Welch’s t-test comparing the surrogate unsaturation indices (UIs) of the various pure oil tubes, as measured using fully sampled SE-SPI.

	Flax	Soy	Sesame	Safflower	Peanut
Flax	NA	$p < 0.001$	$p < 0.001$	$p < 0.001$	$p < 0.001$
Soy	NA	NA	$p = 0.207$	$p = 0.004$	$p = 0.017$
Sesame	NA	NA	NA	$p = 0.005$	$p = 0.066$
Safflower	NA	NA	NA	NA	$p = 0.449$
Peanut	NA	NA	NA	NA	NA

Given in Tables 4.7, 4.8, and 4.9 are the results of Welch’s t-test comparing the polyunsaturation indices of the five oils using PRESS, fully sampled SE-SPI, and CS-SE-SPI, respectively. As was the case with UI, significant differences were observed between all of the oils using PRESS except when comparing peanut to safflower and soy to sesame. This was also the case for CS SE-SPI. Fully sampled SE-SPI observed a significant difference between all oil types.

Table 4.6: Preclinical results of Welch’s t-test comparing the surrogate unsaturation indices (UIs) of the various pure oil tubes, as measured using retrospectively accelerated ($R = 5.5$) CS SE-SPI.

	Flax	Soy	Sesame	Safflower	Peanut
Flax	NA	$p = 0.016$	$p = \mathbf{0.008}$	$p = \mathbf{0.004}$	$p = \mathbf{0.002}$
Soy	NA	NA	$p = 0.030$	$p = \mathbf{0.002}$	$p < \mathbf{0.001}$
Sesame	NA	NA	NA	$p = 0.024$	$p = \mathbf{0.001}$
Safflower	NA	NA	NA	NA	$p = 0.045$
Peanut	NA	NA	NA	NA	NA

Table 4.7: Preclinical results of Welch’s t-test comparing the polyunsaturation indices (PUI) of the various pure oil tubes, as measured using PRESS.

	Flax	Soy	Sesame	Safflower	Peanut
Flax	NA	$p < \mathbf{0.001}$	$p < \mathbf{0.001}$	$p < \mathbf{0.001}$	$p < \mathbf{0.001}$
Soy	NA	NA	$p = 0.035$	$p = \mathbf{0.001}$	$p = \mathbf{0.003}$
Sesame	NA	NA	NA	$p < \mathbf{0.001}$	$p < \mathbf{0.001}$
Safflower	NA	NA	NA	NA	$p = 0.242$
Peanut	NA	NA	NA	NA	NA

Table 4.8: Preclinical results of Welch’s t-test comparing the polyunsaturation indices (PUI) of the various pure oil tubes, as measured using fully sampled SE-SPI.

	Flax	Soy	Sesame	Safflower	Peanut
Flax	NA	$p < \mathbf{0.001}$	$p < \mathbf{0.001}$	$p < \mathbf{0.001}$	$p < \mathbf{0.001}$
Soy	NA	NA	$p < \mathbf{0.001}$	$p < \mathbf{0.001}$	$p < \mathbf{0.001}$
Sesame	NA	NA	NA	$p < \mathbf{0.001}$	$p < \mathbf{0.001}$
Safflower	NA	NA	NA	NA	$p = \mathbf{0.007}$
Peanut	NA	NA	NA	NA	NA

Table 4.9: Preclinical results of Welch’s t-test comparing the polyunsaturation indices (PUI) of the various pure oil tubes, as measured using retrospectively undersampled ($R = 5.5$) CS SE-SPI.

	Flax	Soy	Sesame	Safflower	Peanut
Flax	NA	$p < 0.001$	$p < 0.001$	$p < 0.001$	$p < 0.001$
Soy	NA	NA	$p = 0.018$	$p < 0.001$	$p < 0.001$
Sesame	NA	NA	NA	$p = 0.012$	$p = 0.007$
Safflower	NA	NA	NA	NA	$p = 0.444$
Peanut	NA	NA	NA	NA	NA

Shown in Figure 4.6 are the relative fat peak amplitudes for the five pure oil tubes calculated from four scans of oil phantoms with the clinical system, along with raw spectra acquired from the 100% soybean oil tube. There was no evidence of aliasing of the water peak in this case; although, it should be noted that the tubes containing soybean oil emulsions were much smaller than those containing the pure oil samples. In many cases, there was an offset between peak amplitude measurements made using SE-SPI and those made using PRESS. For example, the relative amplitude of Peak 5 seems to be consistently under-estimated with SE-SPI compared to PRESS, with this difference made up by some of the smaller fat peaks (e.g. Peak 4). Retrospectively undersampled CS SE-SPI results were, in most cases, in agreement with their fully sampled counterparts.

Shown in Figure 4.7 are the corresponding indices, UI, UIs, and PUI, as calculated from Equations 2.13, 2.14, and 2.15, respectively, along with lipid composition maps derived from one of the CS SE-SPIs. Unlike the preclinical results shown in Figure 4.4, clinical SE-SPI measurements were more variable than those made using PRESS, and fat maps for the individual scan shown are less homogeneous than those acquired with the preclinical system. In many cases there was an offset between fatty acid composition measurements made using PRESS compared to those made using SE-SPI, especially in the case of the surrogate unsaturation index, UIs, as expected based on the relative fat peak amplitudes in Figure 4.6.

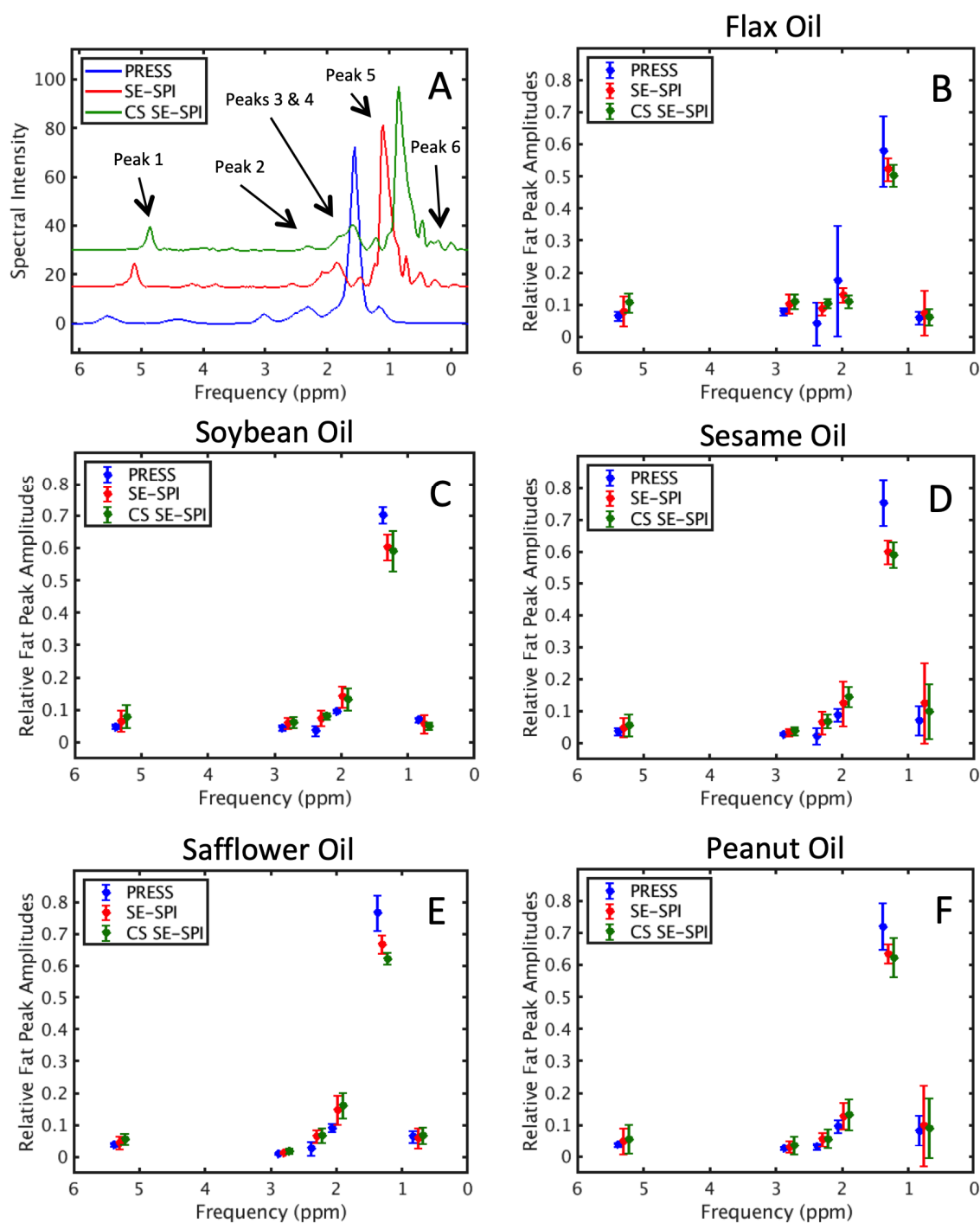


Figure 4.6: (A) 100% soybean spectra acquired using clinical PRESS, SE-SPI (showing results for a single voxel), and retrospectively accelerated ($R = 3$) CS SE-SPI, offset for clarity. (B-F) Relative peak amplitudes of the six fat peaks (mean \pm 95% CI over four scans, plotted at their corresponding frequencies, offset for clarity) for the pure oil tubes as measured using clinical PRESS, fully sampled SE-SPI, and retrospectively accelerated ($R = 3$) CS SE-SPI.

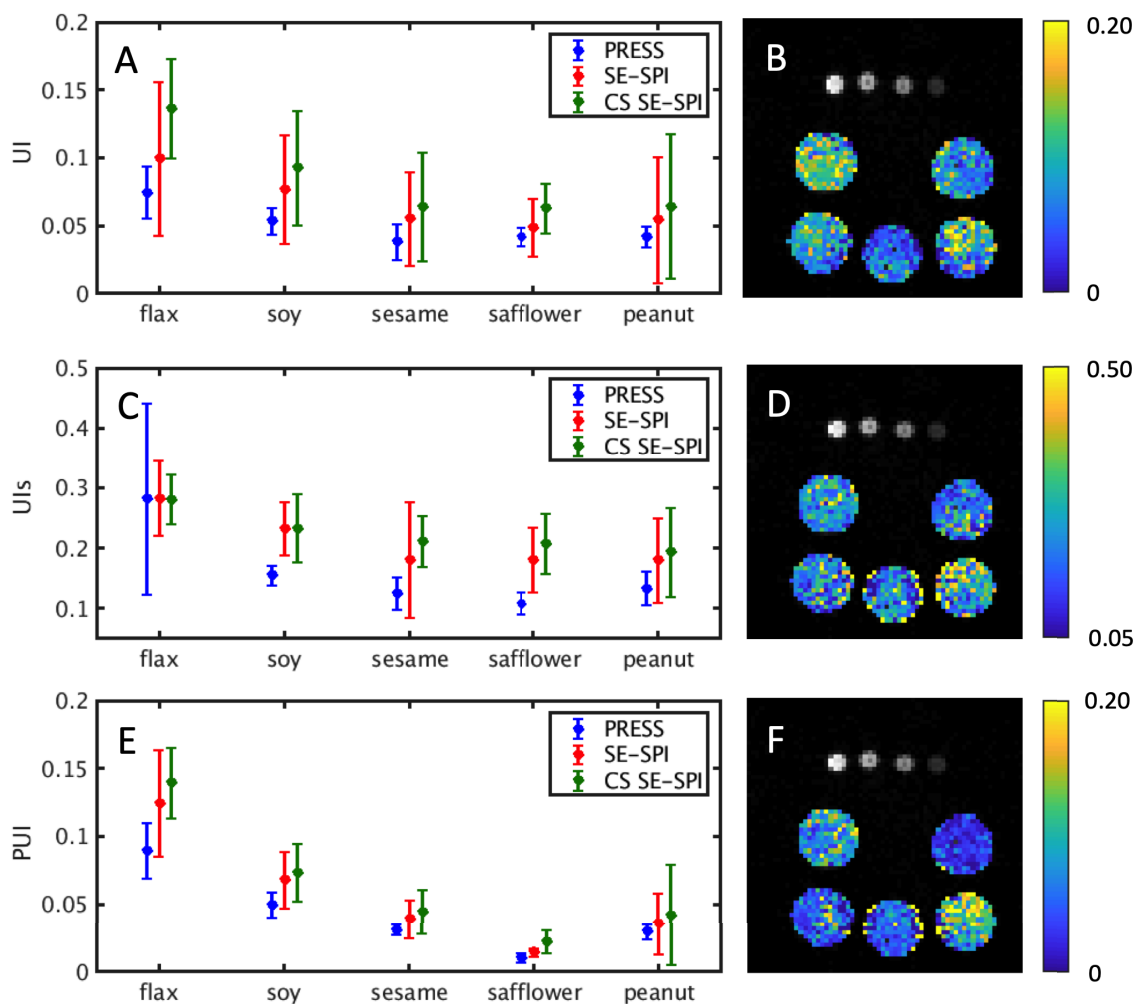


Figure 4.7: (A, C, E) Unsaturation (UI), surrogate unsaturation (UIs), and polyunsaturation (PUI) indices (mean \pm 95% CI over four scans) for the flax, soybean, sesame, safflower, and peanut oil tubes as measured using clinical PRESS, fully sampled SE-SPI, and retrospectively accelerated ($R = 3$) CS SE-SPI. (B, D, F) Maps of UI, UIs, and PUI, respectively, for one retrospectively accelerated clinical CS SE-SPI of the oil phantom. From left to right, top to bottom, are the 5%, 10%, 15%, and 20% soybean oil emulsions (maps not shown), along with pure soybean, safflower, peanut, sesame, and flax oil tubes.

Despite these offsets, the general trend in these fatty acid composition metrics seemed to be consistent between techniques. Given in Tables 4.10, 4.11, and 4.12 are the results of Welch’s t-test comparing the unsaturation indices of the five oils using PRESS, fully sampled SE-SPI, and CS-SESPI, respectively. Using PRESS, flax oil was observed to have significantly higher unsaturation index compared to all other oils except soy. No significant differences were observed with fully sampled SE-SPI. CS SE-SPI could only distinguish flax oil from sesame and safflower.

Table 4.10: Clinical results of Welch’s t-test comparing the unsaturation indices (UI) of the various pure oil tubes, as measured using PRESS.

	Flax	Soy	Sesame	Safflower	Peanut
Flax	NA	$p = 0.031$	$p = 0.004$	$p = 0.008$	$p = 0.008$
Soy	NA	NA	$p = 0.024$	$p = 0.021$	$p = 0.024$
Sesame	NA	NA	NA	$p = 0.485$	$p = 0.478$
Safflower	NA	NA	NA	NA	$p = 0.968$
Peanut	NA	NA	NA	NA	NA

Table 4.11: Clinical results of Welch’s t-test comparing the unsaturation indices (UI) of the various pure oil tubes, as measured using fully sampled SE-SPI.

	Flax	Soy	Sesame	Safflower	Peanut
Flax	NA	$p = 0.337$	$p = 0.089$	$p = 0.059$	$p = 0.101$
Soy	NA	NA	$p = 0.251$	$p = 0.115$	$p = 0.300$
Sesame	NA	NA	NA	$p = 0.636$	$p = 0.971$
Safflower	NA	NA	NA	NA	$p = 0.736$
Peanut	NA	NA	NA	NA	NA

Given in Tables 4.13, 4.14, and 4.15 are the results of Welch’s t-test comparing the surrogate unsaturation indices of the five oils using PRESS, fully sampled SE-SPI, and CS-SESPI, respectively. SE-SPI, both fully sampled and accelerated, showed a significant difference between flax and safflower oils. Additionally, CS SE-SPI was able to distinguish between flax and sesame oils. A similar trend was observed with PRESS, but the large variation in the UIs of flax oil meant many of these comparisons were not significant. On the other hand, PRESS was able to distinguish soybean oil from sesame whereas SE-SPI and CS SE-SPI could not.

Table 4.12: Clinical results of Welch’s t-test comparing the unsaturation indices (UI) of the various pure oil tubes, as measured using retrospectively accelerated ($R = 3$) CS SE-SPI.

	Flax	Soy	Sesame	Safflower	Peanut
Flax	NA	$p = 0.048$	$p = 0.005$	$p = 0.003$	$p = 0.015$
Soy	NA	NA	$p = 0.166$	$p = 0.107$	$p = 0.235$
Sesame	NA	NA	NA	$p = 0.949$	$p = 0.985$
Safflower	NA	NA	NA	NA	$p = 0.943$
Peanut	NA	NA	NA	NA	NA

Table 4.13: Clinical results of Welch’s t-test comparing the surrogate unsaturation indices (UIs) of the various pure oil tubes, as measured using PRESS.

	Flax	Soy	Sesame	Safflower	Peanut
Flax	NA	$p = 0.090$	$p = 0.050$	$p = 0.040$	$p = 0.057$
Soy	NA	NA	$p = 0.030$	$p < 0.001$	$p = 0.085$
Sesame	NA	NA	NA	$p = 0.159$	$p = 0.541$
Safflower	NA	NA	NA	NA	$p = 0.062$
Peanut	NA	NA	NA	NA	NA

Table 4.14: Clinical results of Welch’s t-test comparing the surrogate unsaturation indices (UIs) of the various pure oil tubes, as measured using fully sampled SE-SPI.

	Flax	Soy	Sesame	Safflower	Peanut
Flax	NA	$p = 0.088$	$p = 0.035$	$p = 0.008$	$p = 0.014$
Soy	NA	NA	$p = 0.192$	$p = 0.060$	$p = 0.101$
Sesame	NA	NA	NA	$p = 0.993$	$p = 0.988$
Safflower	NA	NA	NA	NA	$p = 0.975$
Peanut	NA	NA	NA	NA	NA

Given in Tables 4.16, 4.17, and 4.18 are the results of Welch’s t-test comparing the polyunsaturation indices of the five oils using PRESS, fully sampled SE-SPI, and CS-SESPI, respectively. All three techniques showed flax oil as having a significantly larger PUI as compared to all other oil types. In fact PRESS was able to distinguish between all oil types except in the case of comparing sesame to peanut oil. SE-SPI

measurements, both fully sampled and accelerated, showed similar trends, but in many cases these trends were not significant.

Table 4.15: Clinical results of Welch’s t-test comparing the surrogate unsaturation indices (UIs) of the various pure oil tubes, as measured using retrospectively accelerated ($R = 3$) CS SE-SPI.

	Flax	Soy	Sesame	Safflower	Peanut
Flax	NA	$p = 0.079$	$p = 0.009$	$p = 0.012$	$p = 0.024$
Soy	NA	NA	$p = 0.360$	$p = 0.325$	$p = 0.225$
Sesame	NA	NA	NA	$p = 0.875$	$p = 0.537$
Safflower	NA	NA	NA	NA	$p = 0.629$
Peanut	NA	NA	NA	NA	NA

Table 4.16: Clinical results of Welch’s t-test comparing the polyunsaturation indices (PUI) of the various pure oil tubes, as measured using PRESS.

	Flax	Soy	Sesame	Safflower	Peanut
Flax	NA	$p = 0.004$	$p = 0.002$	$p < 0.001$	$p = 0.002$
Soy	NA	NA	$p = 0.004$	$p < 0.001$	$p = 0.002$
Sesame	NA	NA	NA	$p < 0.001$	$p = 0.474$
Safflower	NA	NA	NA	NA	$p < 0.001$
Peanut	NA	NA	NA	NA	NA

Table 4.17: Clinical results of Welch’s t-test comparing the polyunsaturation indices (PUI) of the various pure oil tubes, as measured using fully sampled SE-SPI.

	Flax	Soy	Sesame	Safflower	Peanut
Flax	NA	$p = 0.002$	$p = 0.004$	$p = 0.003$	$p = 0.002$
Soy	NA	NA	$p = 0.013$	$p = 0.003$	$p = 0.016$
Sesame	NA	NA	NA	$p = 0.010$	$p = 0.723$
Safflower	NA	NA	NA	NA	$p = 0.057$
Peanut	NA	NA	NA	NA	NA

Table 4.18: Clinical results of Welch’s t-test comparing the polyunsaturation indices (PUI) of the various pure oil tubes, as measured using retrospectively undersampled ($R = 3$) CS SE-SPI.

	Flax	Soy	Sesame	Safflower	Peanut
Flax	NA	$p < \mathbf{0.001}$	$p < \mathbf{0.001}$	$p < \mathbf{0.001}$	$p < \mathbf{0.001}$
Soy	NA	NA	$p = 0.015$	$p = \mathbf{0.002}$	$p = 0.067$
Sesame	NA	NA	NA	$p = 0.015$	$p = 0.854$
Safflower	NA	NA	NA	NA	$p = 0.188$
Peanut	NA	NA	NA	NA	NA

4.3 Discussion

Having chosen appropriate parameters for the BCS reconstruction and HSVD-based spectral decomposition, SE-SPI based quantification, including both fat fraction and fatty acid composition, could be assessed. While measures of lipid composition are the focus of this work, the measured fat fractions of the preclinical soybean oil tube setup are an important measure of aliasing in the CS SE-SPI results. On average, the fat fraction of the phantom set was 30% soybean oil. Thus, uncorrected aliasing of signal in the CS SE-SPI would, on average, result in an increase in fat signal in the soybean oil emulsions, and a decrease in fat signal in the 100% soybean oil tube. This is important to keep in mind when assessing CS SE-SPI fat composition measurements for these lower fat fraction tubes, which could appear to perform better in the presence of aliasing given the amplification of the fat signal. On a side note, it should be reiterated that, while the fat fractions in Figure 4.1 do seem to align somewhat with the percentage amounts of soybean oil, this is coincidental. As discussed in Section 3.3, the fat fractions presented here are not proton density measures, and will be affected by acquisition parameters, the degree to which they are affected depending on the relaxation properties of the sample. As such, fat fractions should not be compared to their expected PDFF, but rather to our ‘gold standard’ PRESS measurements. While some degree of residual aliasing was observed in CS SE-SPI compared to PRESS results, shown in Figure 4.1, it was not considered to be of concern in assessing fatty acid composition results.

The relative fat peak amplitudes of the preclinical soybean oil emulsions measured with SE-SPI showed good agreement with PRESS results. Importantly, smaller peaks did not seem to be underestimated or lost in the CS process, which has the potential to remove low contrast features as a result of the sparsity constraint. This agreement held for smaller fat fractions, although variation increased as a result of the reduced SNR. In most cases, PRESS measurements were more variable than their fully sampled SE-SPI counterparts, likely a result of the larger relative voxel size allowing more shim-induced line broadening. Furthermore, CS SE-SPI results were often less variable than those from fully sampled scans, likely a result of enforcing sparsity in the data, as noise that would be present even in the fully sampled scans is likely not sparse [55]. The reduction in variation in a single scan can be seen in the CS reconstructed fat maps in Figures 3.11-3.14. Unsurprisingly, many of the same trends were observed in the lipid composition metrics derived from these relative peak amplitudes.

While important that these measures of lipid composition are consistent for varying fat fractions, it is also important that differences in lipid composition can be observed. Given that only one oil type (soybean) was present in the scans used to generate the results in Figures 4.2 and 4.3, it is possible that the BCS algorithm, which learns the basis functions from the data itself, assigned a higher weight to spectral basis functions fitting of soybean oil composition. Similarly, it might be expected, in a scan containing oils of varying composition, that basis functions describing spectra of more predominant features could be favoured while those present to a lesser degree are suppressed, complicating the differentiation of different oils.

The fatty acid composition of the pure oil tubes, as measured using CS SE-SPI, showed similar trends to that observed with PRESS, using both the preclinical and clinical systems. For the preclinical results, all significant differences in UI between oils as quantified using PRESS were also observed with SE-SPI, both fully sampled and accelerated. In the case of UIs, while the general trend in lipid composition seems similar for all three techniques, as shown in Figure 4.4, the large variation in PRESS measurements, and that of flax oil for CS SE-SPI, meant many of these trends were not significant. In the case of PUI, all trends were identical, except that fatty acid composition as measured using fully sampled SE-SPI showed a significant differences

when comparing sesame to soybean oil and safflower to peanut oil and whereas CS SE-SPI and PRESS did not. Looking at Figure 4.5F, the difference between safflower and peanut oil observed with SE-SPI seems to have been a result of underestimating the relative amplitude of the methylene peak (Peak 5). In fact, this was a common trend in fully sampled SE-SPI measurements across all of the pure oil samples. As this did not occur in the CS SE-SPI measurements, this offset does not seem to be introduced by the nature of the sequence. One possible explanation for this trend could be bias in the spectral decomposition step, caused, for example, by increased noise in the fully sampled SE-SPI spectra that is removed in the CS process; however, further investigation is required. Whatever the underlying cause, it may also be causing the overestimation of fat fraction with fully sampled SE-SPI in Figure 4.1, especially apparent in the 20% soybean oil emulsion tube. Nonetheless, the CS results are most relevant for this work. All trends in lipid composition observed with PRESS were also observed with SE-SPI, even after retrospective acceleration, and while there existed cases in which CS SE-SPI observed significant differences that PRESS did not, this may have been a result of the large variation in PRESS measurements.

It is worth noting that, as discussed in the Methods section, a retrospective undersampling factor of $R = 5.5$ was chosen for this preclinical analysis in order to match that observed in the mouse study. However, it should be reiterated that the phantom scans used to obtain these results are 2D. Higher dimensional datasets are more compressible, meaning their sparse representations will provide a more accurate model of the true signal [43]. As such, it may be the case that these results would improve for 3D applications of the same undersampling factor.

For the clinical results, trends in fatty acid composition were also similar across techniques. However, in this case large variations in SE-SPI measures of fatty acid composition metrics, both for the fully sampled and retrospectively accelerated scans as Shown in Figure 4.7, meant many of these trends were not significant. As was the case for preclinical PRESS measurements, this large variation may be a result of difficulties shimming the phantom. For clinical PRESS acquisitions, higher order shimming was performed in order to improve B_0 homogeneity across the voxel. However, applying similar higher order shimming procedures to the larger imaging volumes used with a spectroscopic imaging techniques such as SE-SPI will likely not

achieve the same degree of homogeneity [34, 78]. Even so, where trends observed with SE-SPI were significant, they were often in agreement with PRESS results.

There also appeared to be some slight bias between clinical PRESS and SE-SPI lipid composition measurements, with SE-SPI consistently overestimating each metric in comparison to PRESS, especially apparent for UIs in Figure 4.7. Interestingly, comparing clinical SE-SPI measurements to those made on the preclinical system, as shown in Supplementary Figure 4.8, shows little evidence of bias, implying that shown in Figure 4.7 may have been introduced by the clinical PRESS sequence.

Nonetheless, for this work, as stated in Hypothesis A, fatty acid composition measures are said to agree for two techniques if they show the same trends across oils, as determined using Welch's t-test. By this definition preclinical PRESS and CS SE-SPI measurements can be said to agree. However, the clinical implementation of CS SE-SPI did not have the same sensitivity as PRESS, seemingly a result of the large variation in fatty acid composition metrics. This definition of agreement was chosen as opposed to more thorough equivalence testing, the two-one-sided t-tests (TOST) procedure, for example, as these types of equivalence tests often require choosing some threshold of agreement. Since it is not yet known what degree of change in lipid composition will be observed in a clinical setting, choosing such a threshold at this point seemed somewhat arbitrary.

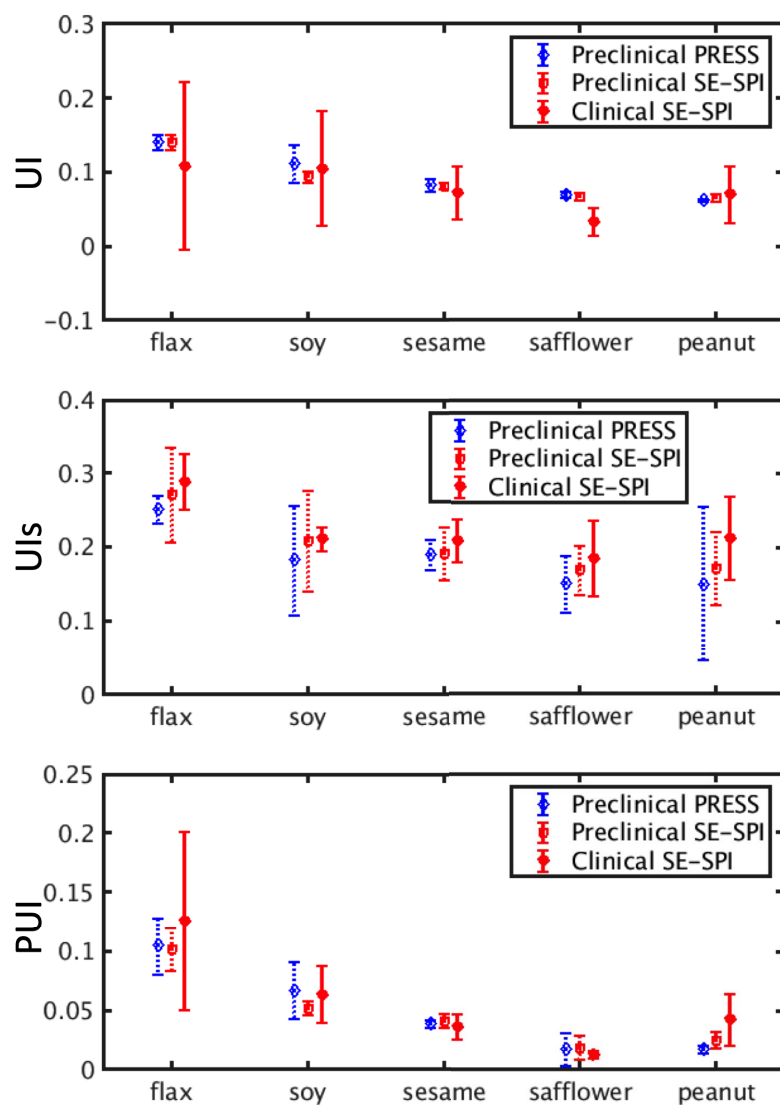


Figure 4.8: Unsaturation (UI), surrogate unsaturation (UIs), and polyunsaturation (PUI) indices (mean \pm 95% CI over 3 scans, clinical SE-SPI scan parameters matched to those used preclinically) for the flax, soybean, sesame, safflower, and peanut oil tubes as measured using fully sampled SE-SPI on the clinical system, alongside pre-clinical PRESS and SE-SPI measurements.

Chapter 5

In vivo Mouse Evaluation

5.1 Methods

5.1.1 Experimental Design

The protocol for this *in vivo* mouse study was approved by the local Animal Care Committee. Sixteen BALB/c mice (Charles River, Wilmington, US) were divided into four groups, one of which received a normal diet and no iron injections, one which received an MCD diet to induce fatty liver and no iron injections, one which received a normal diet and iron injections, and the last of which received both the MCD diet and iron injections. The MCD diet formulation used was Teklad TD.90262 (Envigo, Huntingdon, UK), which results in a sequestering of fat in the liver, as well as liver inflammation, in a relatively short period of time. Intravenous injection of superparamagnetic iron oxide (SPIO) particles (Feraspin XXL from Miltenyi Biotec, Bergisch Gladbach, Germany) was used to simulate iron overload; mice received an approximate dose of 40 $\mu\text{mol}/\text{kg}$, injected into their tail vein the day before each scanning session. Mice receiving a normal diet were scanned on two days, one week apart. Mice receiving the MCD diet were scanned three times, on Days 0, 4, and 11, defining Day 1 as the first day of the diet. One mouse from each group was sacrificed on the second last day of planned scanning (following the first session for normal diet groups, or the Day 4 session for the MCD diet groups). Remaining mice were sacrificed following the final session.

Each scanning session consisted of a balanced steady-state free precession (bSSFP) anatomical image ($256 \times 128 \times 128$ matrix with $1.5 \times 2 \times 2$ mm voxels, $\alpha = 30^\circ$, $TR/TE = 8/4$ ms), 3D undersampled SE-SPI ($R = 4$, scan time of 55 minutes, acquisition parameters matched to those used for preclinical phantom experiments), and an *in vivo* PRESS voxel ($TR/TE = 10000/13$ ms, receiver $BW = 3$ kHz, $5 \times 5 \times 5$ mm voxel, 4096 points acquired at each readout, 25 averages). Mice were anaesthetised

for the entire protocol, and temperature maintained at 37°C . Following the final session, mice were terminated and their livers excised, maintained in a fluorinated hydrocarbon solution. An *ex vivo* PRESS voxel was acquired, positioned such that the signal obtained was that from the entire liver volume ($15 \times 15 \times 15$ mm to $15 \times 15 \times 25$ mm voxel, otherwise identical to that acquired *in vivo*).

5.1.2 Lipid Composition Analysis

Following motion correction, CS SE-SPIs were reconstructed using BCS, with $n_{iter} = 30$ iterations, $r = 35$ basis functions, regularization parameter $\lambda = 0.01$, and scaled by a factor of $s = 2$ as determined with the phantom experiments described in Chapter 3. Spectra obtained from CS SE-SPI and PRESS were processed as described in Section 3.3 assuming $N = 25$ HSVD components for the main HSVD and using the bins given in Table 5.1. The water bin used for *in vivo* experiments was considerably larger than that used for phantoms in order to accommodate peak splitting in PRESS measurements.

Table 5.1: Bins, based on those described in Johnson et al. [23], used in separating the fatty acid functional groups for preclinical mouse experiments. Bins were determined in reference to the water resonance, taken as 4.7 ppm *in vivo*, as expected for temperatures near 39°C [67].

Peak	Frequency Bins (ppm)
Methene (Peak 1)	5.05 – 5.55
Water	3.05 – 6.35
Diallylic (Peak 2)	2.55 – 3.05
α -Methylene to carboxyl (Peak 3)	2.05 – 2.55
Allylic (Peak 4)	1.55 – 2.05
Methylene (Peak 5)	1.05 – 1.55
Methyl (Peak 6)	0.55 – 1.05

In order to correct for differences in T_1 saturation effects, given the difference in TR between SE-SPI and PRESS measurements, the following theoretical correction was applied to fat fractions as measured using SE-SPI:

$$FF = \frac{(1 - \exp[-TR/T_{1,fat}])FF_{TR}}{(1 - \exp[-TR/T_{1,fat}])FF_{TR} + (1 - \exp[-TR/T_{1,water}])FF_{TR}} \quad (5.1)$$

where FF is the TR corrected fat fraction, FF_{TR} the uncorrected fat fraction, $T_{1,fat}$ and $T_{1,water}$ the longitudinal relaxation times of fat and water, respectively. This correction was based on the expected steady state signal, as derived in Section A.1. T_1 values chosen were 300 ms and 1 s for fat and water, respectively, in order to best fit paired PRESS data acquired in mice with long (10 s) and short (200 ms) TR .

Mouse liver contours were drawn using the bSSFP anatomical in VivoQuant (In-vicro, Boston, US). In many cases, the SE-SPI imaging volume did not overlap well with the PRESS voxel, as shown in Figure 5.1, as PRESS voxel placement prioritized overlap with the liver as opposed to overlap with the SE-SPI volume. Additionally, the SNR of CS SE-SPI data in slices near the edge of the imaging volume was poor, further complicating comparison in these cases of limited overlap. Thus, the ROI used for CS SE-SPI analysis was limited to the portion of liver volume imaged with adequate signal (greater than the mean CS SE-SPI signal intensity, see Figure 5.1).

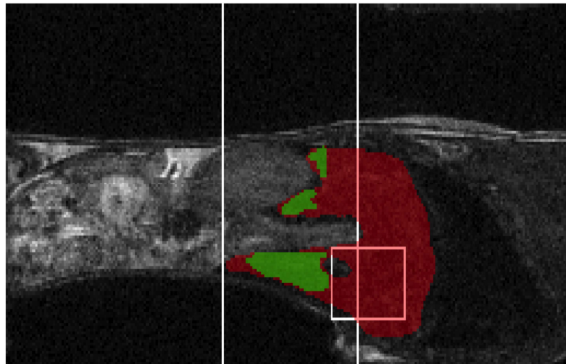


Figure 5.1: Sagittal slice of the bSSFP anatomical. The larger white outline indicates the SE-SPI volume, and the smaller outline the PRESS voxel. The liver contour is shown in red. Shown in green is the ROI used for SE-SPI analysis; i.e. liver tissue having adequate SE-SPI signal intensity.

One *in vivo* PRESS spectra was omitted from analysis due to lack of overlap with the contoured liver volume (a mouse on Day 0 of the MCD diet, no iron injection). For the same mouse, in the same session, the CS SE-SPI dataset was omitted due to a lack of liver tissue with adequate signal intensity. Furthermore, spectra for which necessary fat peaks (e.g. Peak 2 for PUI) were not identified were also omitted from the analysis, as this was often a result of errors in the spectral decomposition as opposed to true absence of a fat peak. In the case of PRESS, this datapoint was

omitted entirely. For CS SE-SPI, UI , UI_s , and PUI were averaged¹ over spectra in the liver volume for which the necessary fat peaks were identified.

As opposed to intramouse comparisons, complicated both by lack of overlap and the difference in TR, among other things, PRESS and CS SE-SPI results were analyzed at the group level. As was the case for preclinical experiments, statistical comparisons were made using Welch's t-test.

5.2 Results

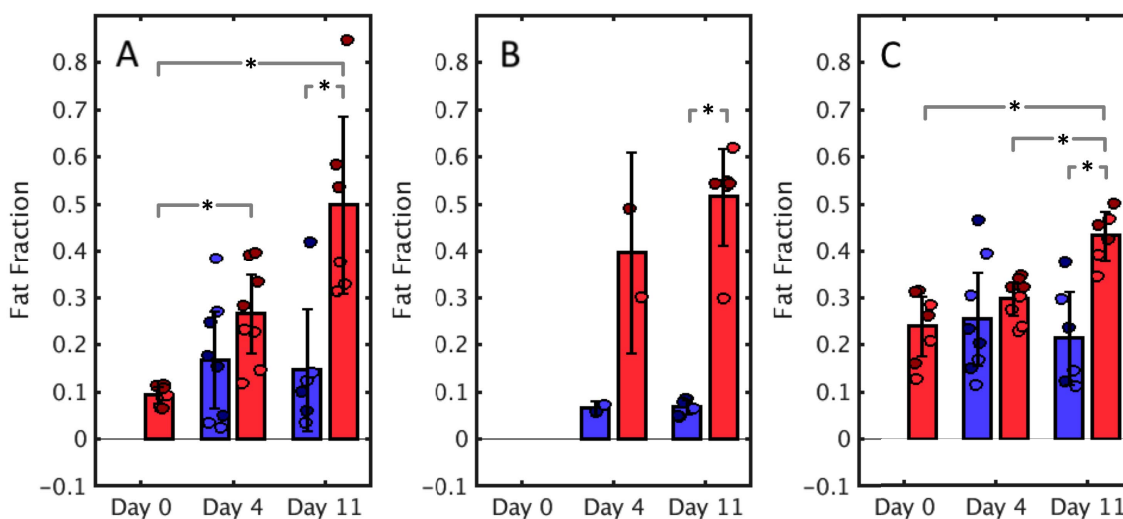


Figure 5.2: Fat fraction as calculated using *in vivo* PRESS spectra (A), *ex vivo* PRESS spectra (B), and CS SE-SPI (C). Bar plots and error bars indicate the mean and 95% CI over the control diet groups, in blue, and the MCD diet groups, in red, on Days 0, 4, and 11 (Day 1 being the start of the diet). Scatter plots show results for individual mice, darkened points are those mice which received iron injection.

Given in Figure 5.2 are the fat fraction results (TR corrected in the case of CS SE-SPI) of the mouse study. The results for the control diet group are displayed alongside those for the MCD diet group on Days 4 and 11 to allow visualization of expected trends (MCD diet was started on Day 1, so no difference is expected on Day 0). Statistically significant differences ($p < 0.05$ using Welch's t-test, corrected with the Bonferroni correction) are indicated between the MCD diet and control groups for each day, and between days for each group. Statistical testing was not performed for

¹Averaging of fat composition indices was not weighted by FF .

groups containing fewer than 3 datapoints (e.g. *ex vivo* PRESS data from Day 4). All between group comparisons were consistent with both *in vivo* and *ex vivo* PRESS and CS SE-SPI. While the CS SE-SPI fat fraction measurements did not vary temporally to the same degree as those measured with *in vivo* PRESS, the latter measurements varied more within groups, potentially caused by some systematic bias whereby the fat fraction measured for MCD mice having received iron injection was consistently higher than that for MCD mice without this iron overload.

Given in Figures 5.3 and 5.4 are the UI, UIs, and PUI as measured using *in vivo* PRESS and *ex vivo* PRESS, respectively. No trends in fat composition were observed using either technique. In fact, PRESS results in general were very scattered. Shown in Figure 5.5 are some examples of spectra acquired using *in vivo* PRESS, *ex vivo* PRESS, and CS SE-SPI. The quality of *in vivo* PRESS spectra was generally poor, with increased linewidths and peak splitting compared to *ex vivo* PRESS spectra. While peak splitting was not observed in the large majority of *ex vivo* PRESS measurements, in many cases linewidths were larger than those observed with CS SE-SPI.

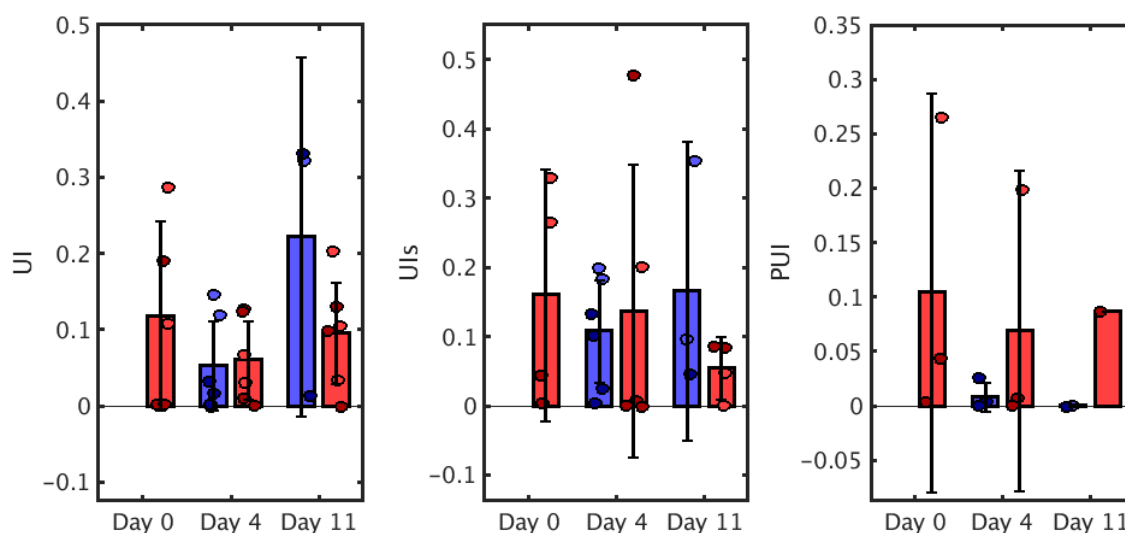


Figure 5.3: Unsaturation (UI), surrogate unsaturation (UIs), and polyunsaturation (PUI) indices as calculated from *in vivo* PRESS spectra. Bar plots and error bars indicate the mean and 95% CI over the control diet groups, in blue, and the MCD diet groups, in red, on Days 0, 4, and 11 (Day 1 being the start of the diet). Scatter plots show results for individual mice, darkened points are those mice which received iron injection.

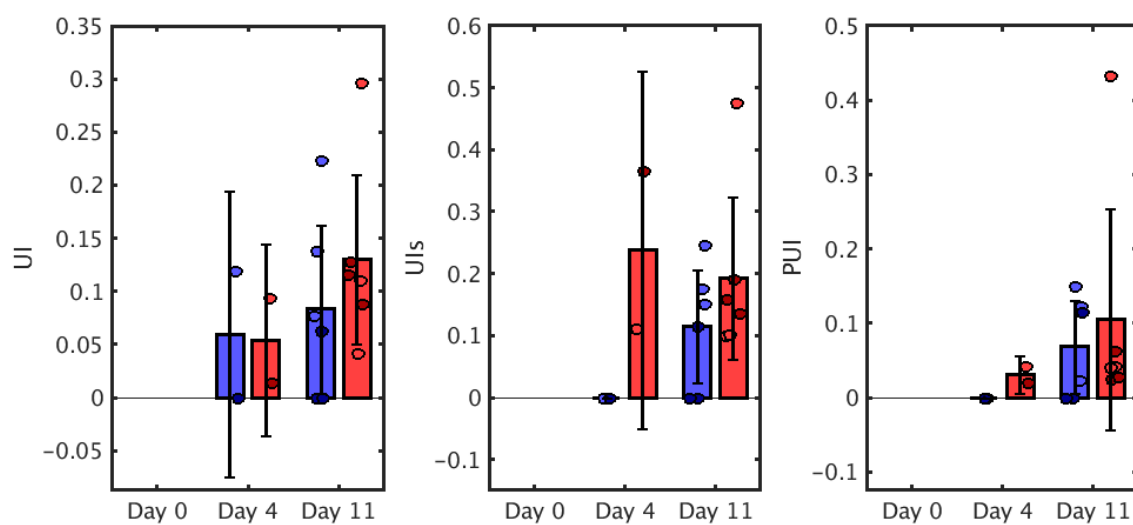


Figure 5.4: Unsaturation (UI), surrogate unsaturation (UIs), and polyunsaturation (PUI) indices as calculated from *ex vivo* PRESS spectra. Bar plots and error bars indicate the mean and 95% CI over the control diet groups, in blue, and the MCD diet groups, in red, on Days 0, 4, and 11 (Day 1 being the start of the diet). Scatter plots show results for individual mice, darkened points are those mice which received iron injection.

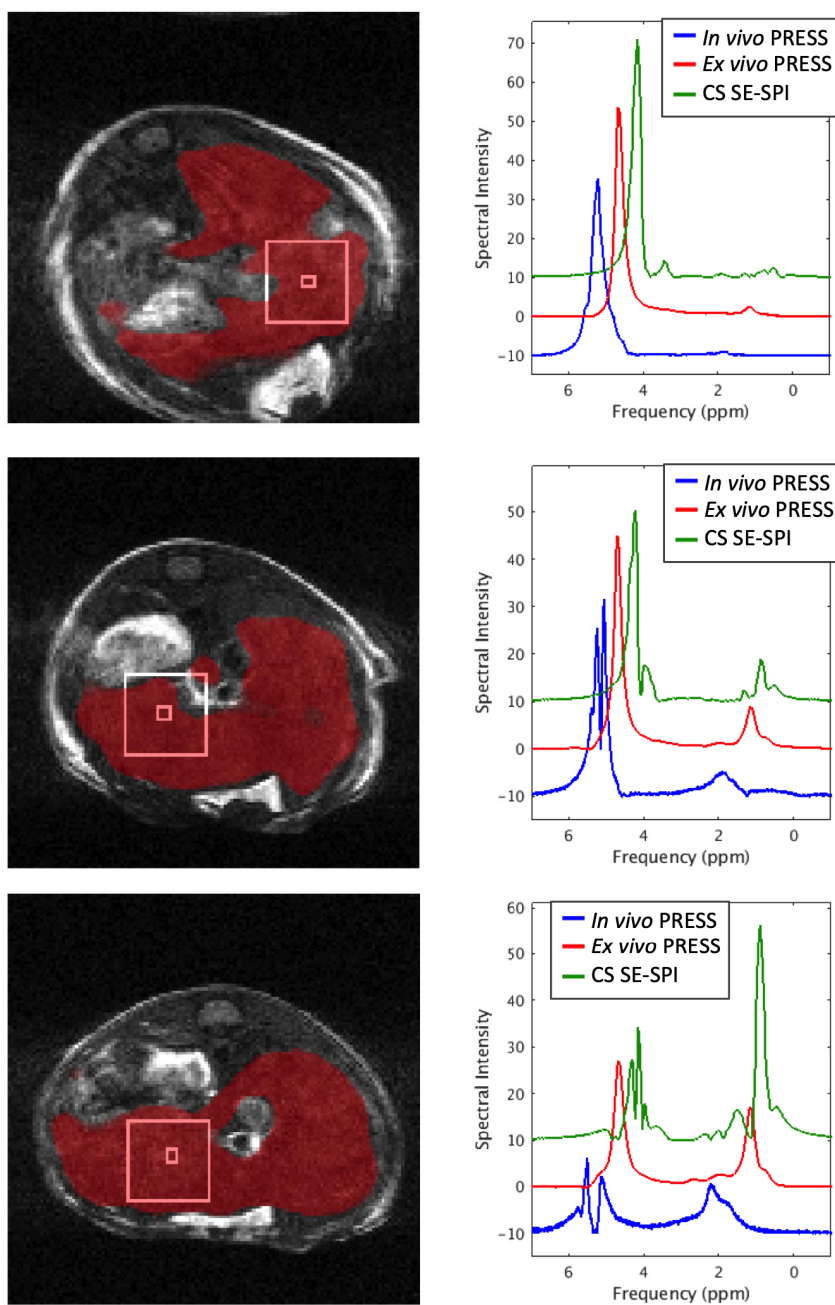


Figure 5.5: Raw spectra (unphased, absolute values shown), shown for *in vivo* PRESS, *ex vivo* PRESS, and a single CS SE-SPI voxel, offset for clarity, alongside anatomical images with liver contour shown in red. *In vivo* PRESS voxels are indicated by the large square outline, and the CS SE-SPI voxel displayed indicated by the small square outline; *ex vivo* PRESS spectra were acquired covering the entire liver. (Top) A mouse in the normal diet group, without iron injection. (Middle) A mouse after 11 days on the MCD diet, without iron injection. (Bottom) A mouse after 11 days on the MCD diet, with iron injection.

Given in Figure 5.6 are the UI, UIs, and PUI as measured using CS SE-SPI. Statistically significant differences, between groups on each day and between days for each group, are indicated. No trends were observed in UI or PUI, but there was a significant decrease in the surrogate unsaturation index, UIs.

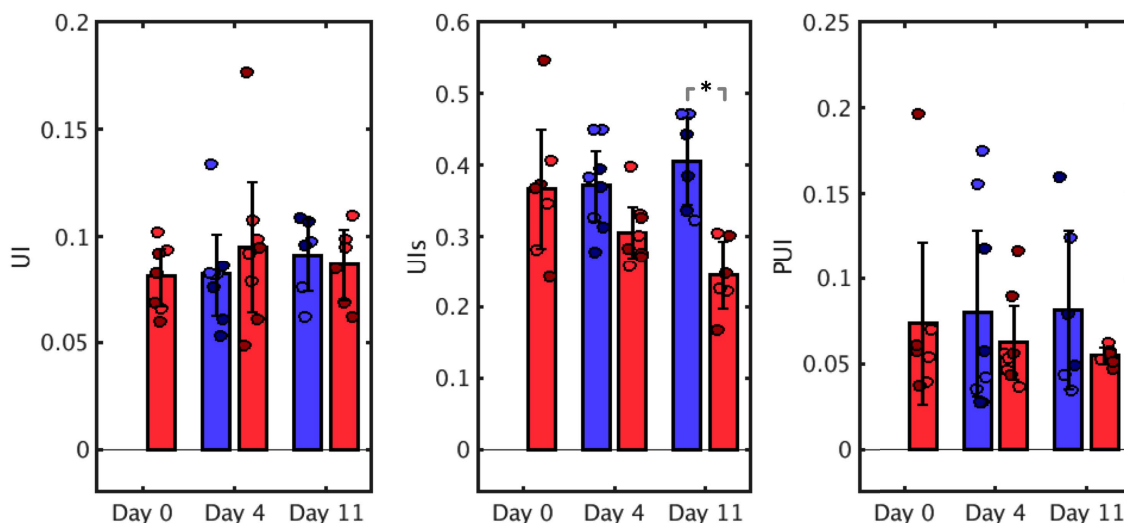


Figure 5.6: Unsaturation (UI), surrogate unsaturation (UIs), and polyunsaturation (PUI) indices as calculated from CS SE-SPI. Bar plots and error bars indicate the mean and 95% CI over the control diet groups, in blue, and the MCD diet groups, in red, on Days 0, 4, and 11 (Day 1 being the start of the diet). Scatter plots show results for individual mice, darkened points are those mice which received iron injection.

Importantly, for individual scans no correlation was observed between fat fraction and fat composition metrics. For UI, only 1/35 scans showed moderate correlation (Spearman's correlation coefficient of -0.5) with fat fraction, remaining scans showed weak to no correlation (correlation coefficients between -0.3 and 0.3). For UIs, all scans showed weak to no correlation with fat fraction. This provides confidence that the observed changes in UIs are not a result of fat fraction related bias in the spectral decomposition, and that UIs as a biomarker provides new information in addition to fat fraction. For PUI, only 8/35 scans showed moderate (correlation coefficients of 0.4 (one scan) and -0.4 (seven scans)) with fat fraction. Shown in Figure 5.7 are maps of fat fraction and UIs in one of the MCD mice with iron injection; there is a clear increase in fat fraction and decrease in UIs from Day 1 to Day 11. Furthermore, there is no apparent pixelwise correlation between fat fraction and UIs in the maps presented.

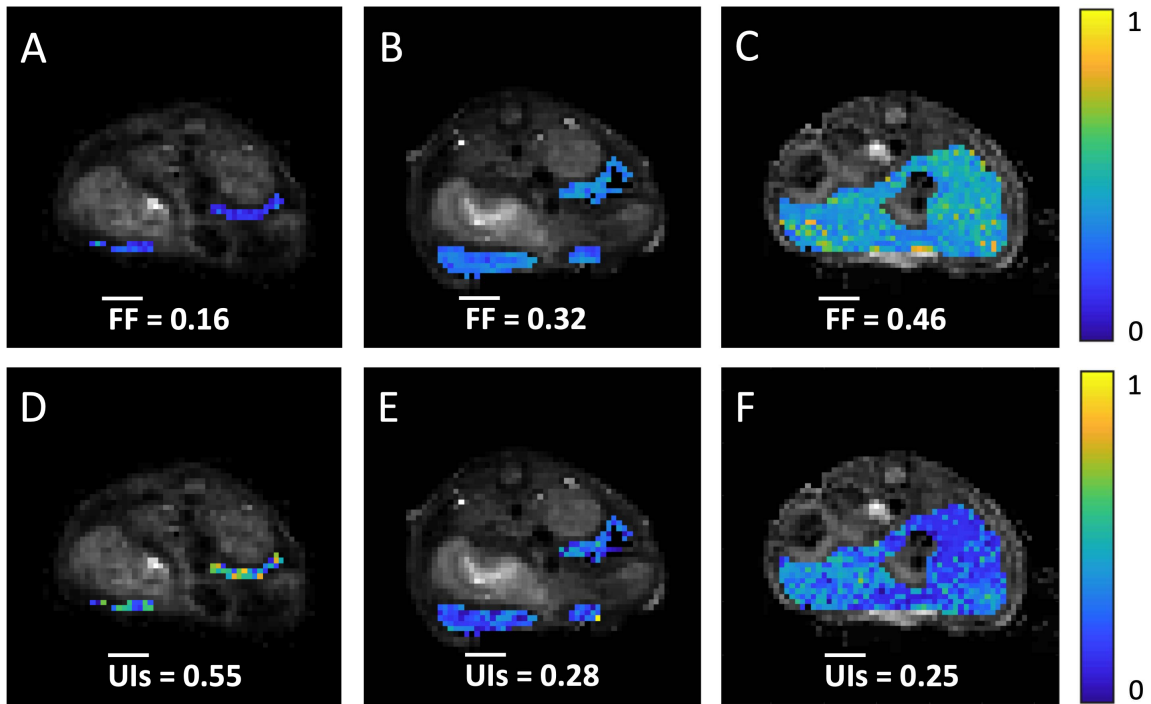


Figure 5.7: (A,B,C) Fat fraction maps (TR corrected) for an MCD mouse, with iron injection, on Days 0, 4, and 11 (Day 1 being the start of the diet), respectively. Average fat fractions over the liver volumes imaged are indicated. (D,E,F) Maps of surrogate unsaturation index, UIs, for the same mouse. Average values of UIs over the liver volumes imaged, omitting voxels for which necessary fat peaks could not be identified, are indicated.

5.3 Discussion

The quality of *in vivo* PRESS spectra was generally poor, with increased linewidths and peak splitting compared to *ex vivo* PRESS spectra, likely a result of the lack of respiratory compensation. While peak splitting was not observed in the large majority of *ex vivo* PRESS measurements, in many cases linewidths were larger than those observed with CS SE-SPI, likely a result of the larger relative voxel size (see Figure 5.8). Additionally, the shorter TR used for CS SE-SPI measurements had a water-suppressing effect which did not occur with PRESS. While not necessarily indicated by the individual CS SE-SPI spectra in Figure 5.5 and the fat fraction results in Figure 5.2 (corrected for T_1 saturation effects), the true fat peak amplitudes as measured using CS SE-SPI were larger, relative to the water peak, than their PRESS counterparts. As seen in Figure 5.5, individual fat peaks were generally more

difficult to visualize in PRESS spectra as compared to those obtained with CS SE-SPI, especially for lower fat fractions in the control group. In addition to this reduced SNR, the spectral decomposition (in particular the number of HSVD components assumed) was optimized for $TR = 200$ ms, potentially resulting in an increase in fitting errors with PRESS as compared to CS SE-SPI.

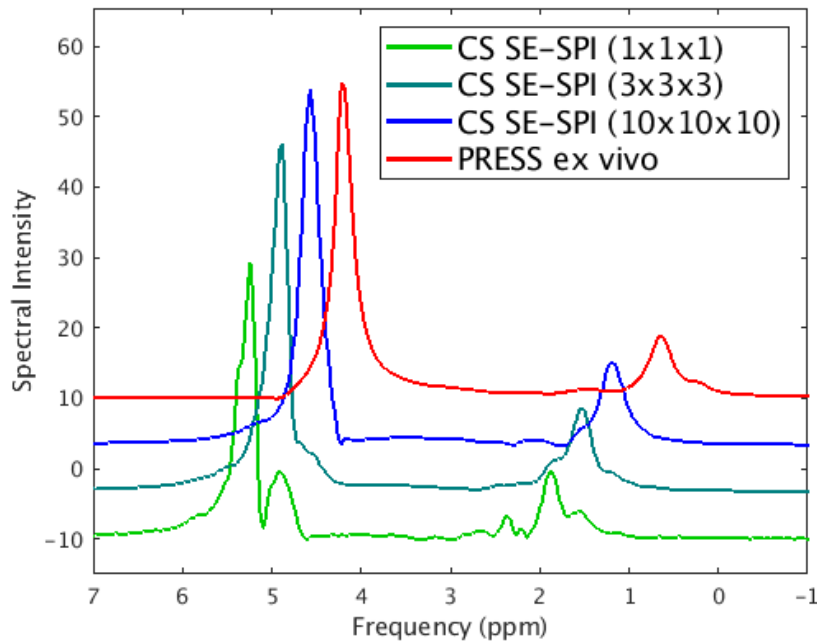


Figure 5.8: Raw spectra (unphased, absolute values shown) for a single *in vivo* CS SE-SPI voxel, as well as those averaged over $3 \times 3 \times 3$ and $10 \times 10 \times 10$ (approximate size of the *in vivo* PRESS voxels) sub-volumes. An *ex vivo* PRESS spectrum is also shown for comparison.

These comments should not be taken as a general statement on the quality of PRESS as compared to CS SE-SPI. Many of the difficulties experienced with PRESS may be remediated to some degree by changing the scan parameters such as TR , acquiring spectra with a more advanced, multichannel RF arrays (improving SNR), compensating for respiratory motion (done by breath hold in a clinical setting, although in this case there may be inconsistencies in the breath hold used for voxel planning and that used for acquiring the spectrum [79]), and making use of higher order shimming. However, these factors did prompt the decision to compare the CS SE-SPI measurements of fat composition with literature as opposed to the PRESS results obtained in this study.

CS SE-SPI results showed a significant decrease in UIs, with no significant change in UI or PUI. While it would be expected to see similar behaviours in UI and UIs, the lack of trend in UI may be a result of assuming prior knowledge in the spectral analysis. As discussed in Section 3.3, large signal components assigned to the methene bin were omitted. However, this required defining a maximum amplitude for the methene peak relative to that of methylene. While this assumption limited UI as a metric of lipid composition, it was required in order to accommodate for peak splitting, especially for *in vivo* PRESS spectra, emphasizing the utility of the surrogate unsaturation index proposed by Johnson et al. [23].

The observed decrease in the surrogate unsaturation index, equivalent to an increase in the relative amount of SFAs, is consistent with results in the literature for mice on this particular MCD diet. A study by Li et al. [29] also investigated the fat sequestration in the liver in terms of fatty acid components, namely SFAs and MUFAs. The group observed, using gas chromatography, a significant increase in the relative amount of SFAs in mice on the MCD diet for 6 weeks, as compared to the control group, with no significant change in the relative amount of MUFAs.

Given a significant increase in the relative amount of SFAs with no change in MUFAs [29], it could be implied that this difference is made up by a decrease in the relative amount of PUFAs. However, no corresponding trend was observed in PUI in this study. Although, UIs is derived from the relative amplitudes of allylic (Peak 2) and diallylic (Peak 4) peaks, as described by Equation 2.14, while PUI is derived solely from the relative amplitude of the diallylic peak, as described by Equation 2.15. While PUFAs are solely responsible for the signal of the diallylic peak, both MUFAs and PUFAs contribute to the signal of the allylic peak (Peak 4), which is generally larger than the diallylic peak (Peak 2), as seen from Figures 4.2 and 4.5. As a result, it may be the case that this additional signal contribution resulted in an observable decrease in UIs, while a decrease in PUI was too small to be observed. Notably, PUI was the most difficult index to visualize with CS SE-SPI, with the largest fraction of voxels omitted from analysis due to difficulty identifying the relevant fat peak (Peak 2).

It should be reiterated that, while the CS SE-SPI fat fraction results are corrected

for T_1 saturation effects, the same is not true of the fat composition measures. Differences in T_1 and T_2 for the fatty acid functional groups [47, 70] will introduce signal weightings in UI, UIs, and PUI that are dependant on scan parameters such as TR and TE . Thus, the indices presented here should be taken as relative measures, not proton density metrics. It is also important to note that, while a decrease in the relative amount of UFAs was observed here and is in agreement with another study of mice on this diet, these results should not be generalized. While the MCD diet was used here to induce fatty livers in mice, and is often used in other applications to study more progressive liver disease, including NASH and fibrosis [80], it is not a true model of human NAFLD, and changes in fat composition may differ from human cases. In fact, changes in fat composition differ for different MCD diets used in animal models of the disease. MCD diets using fructose alone as the carbohydrate source result in a larger increase in the amount SFAs relative to MUFAs as compared to MCD diets using glucose as the carbohydrate source [30].

Nonetheless, these results show that CS SE-SPI can be used to observe changes in lipid composition in an *in vivo* model of NAFLD, even in the presence of iron, as shown in Figure 5.7. Although similar changes were not observed with PRESS, the consistency of the results shown here with those in the literature for mice on an identical MCD diet provides additional confidence in the reliability of this CS SE-SPI technique. While clinical PRESS acquisitions will not be affected by many of the issues experienced with this preclinical set-up, they will inherently be limited in spatial coverage compared to CS SE-SPI, and their larger effective voxel sizes will likely still result in line broadening.

Chapter 6

Conclusions and Future Directions

The work presented in this thesis demonstrates the viability of SE-SPI for lipid composition mapping in NAFLD. Being a purely phase encoded sequence, SE-SPI is an inherently slow imaging technique, limiting its clinical application. However, given the relaxation properties of liver fat, further complicated by high iron concentrations that can accompany liver disease, SE-SPI is preferred over faster spectroscopic imaging techniques which may not be as well-suited for application in NAFLD. Instead, SE-SPI scans were accelerated using compressed sensing, allowing accurate fatty acid composition measurements from randomly undersampled k-space data in a relatively short amount of time. The use of random undersampling also suited the retrospective motion correction used in conjunction with a free-breathing acquisition for *in vivo* applications of CS SE-SPI.

Having chosen appropriate parameters for the BCS reconstruction and spectral decomposition, preclinical phantom results showed CS SE-SPI to be in good agreement with PRESS measurements of fatty acid composition, as proposed in Hypothesis A. CS SE-SPIs of the same pure oil samples on a clinical system also showed similar trends to those observed with PRESS; however, many of these trends were not significant due to the large intersession variability. Importantly, the *in vivo* application of a free-breathing CS SE-SPI sequence in a mouse model of NAFLD showed a significant decrease in the relative amount of UFAs in mice fed an MCD diet, in agreement with literature results as proposed in Hypothesis B. Granted, it should also be noted that the differences in fatty acid composition observed here, both with the oil phantoms and *in vivo* model of liver disease, may not mimic those which occur in clinical cases of NAFLD. A similar analysis of PRESS spectra acquired in this mouse study was complicated by increased linewidths and peaks splitting, and no changes in fatty acid composition were observed. These complications will likely not be as limiting in a clinical setting where breath-holds can account for respiratory motion to some degree

and higher order shimming can improve B_0 homogeneity. However, they did limit the comparison of *in vivo* fatty acid composition measurements between CS SE-SPI and PRESS for this study, as did placement issues.

This work constitutes an important precursor to the implementation of CS SE-SPI in clinical cases of NAFLD. Although, work remains to be done investigating which BCS reconstruction and spectral decomposition parameters are most appropriate in acquiring this fatty acid composition information in the presence of a water peak, as was done preclinically using the soybean oil emulsions. Additionally, it has yet to be determined whether a 2D or 3D CS SE-SPI sequence would be most appropriate for this clinical implementation. While a 3D implementation would provide improved spatial coverage of the liver, it would also require a higher degree of acceleration in order to achieve clinically feasible scan times, which could adversely affect fatty acid composition measurements. Furthermore, it should be noted that the $64 \times 64 \times 16$ 3D matrix used for preclinical acquisitions in this work (taking 55 minutes when 4X undersampled) is not feasible in a clinical setting due to time constraints. 64×64 2D and $40 \times 40 \times 8$ 3D CS SE-SPI sequences, both accelerated to a 10 minute scan time, are being assessed for this clinical application. While scan time may be partially reduced by lowering scan resolution, the effect of this increased voxel size on spectral quality must also be considered.

Lastly, while CS SE-SPI provides spatially resolved maps of fatty acid composition information, for the purposes of this work lipid composition indices were averaged over liver. It may be the case that the spatial distribution of fat composition in the liver could provide additional information in characterizing disease progression. One approach to investigating this theory would be to make use of deep learning, specifically convolutional neural networks (CNNs). CNNs have the potential to automatically extract important features from the data (whether it be fat composition maps or the full spectroscopic imaging dataset) using a training set of images with known NAFLD stage and grade, meaning no prior knowledge of what features are important is required. Such a neural network could also make use of additional diagnostic tests, MRE scans, for example, to explore whether a combination of tests could provide a more robust measure of liver disease progression non-invasively.

Nonetheless, with its improved spatial coverage CS SE-SPI has the potential to

provide a more complete measure of fatty acid composition than MRS techniques used previously in studies of fat composition in NAFLD. As such, it would allow a more thorough investigation as to the potential of this lipid composition information as a biomarker of NAFLD. In particular, the hope is that this fatty acid composition information, along with that information provided by other diagnostic techniques, will allow for a more reliable predictor of liver disease progression than that currently available through non-invasive diagnostic tests. Such information would be especially valuable considering NAFLD is more easily treated in its early stages, and given the degree to which NAFLD affects the population.

Appendix A

Derivations

A.1 Fat Fraction Correction for TR (Equation 5.1)

The signal fat fraction, FF , will be given by:

$$FF = \frac{S_F}{S_F + S_W} \quad (\text{A.1})$$

where S_F and S_W are the relative signal weightings for fat and water, respectively. Define the equivalent water fraction as $WF = (1 - FF)$. Differences in T_1 between fat and water introduce differences in signal weighting by a factor of [81]:

$$M_{\perp} \propto (1 - \exp[-TR/T_1]) \quad (\text{A.2})$$

Thus, the signal fat fraction, now expressed as FF_{TR} , can be expressed in terms of the corrected fat fraction, FF_{∞} , i.e. the fat fraction that would be measured with an infinite TR ,¹ as follows:

$$FF_{TR} = \frac{FF_{\infty}(1 - \exp[-TR/T_{1,fat}])}{FF_{\infty}(1 - \exp[-TR/T_{1,fat}]) + (1 - FF_{\infty})(1 - \exp[-TR/T_{1,water}])} \quad (\text{A.3})$$

where $T_{1,fat}$ and $T_{1,water}$ are the longitudinal relaxation times of fat and water, respectively. Rearranging this equation for the TR corrected fat fraction gives:

$$FF_{\infty} = \frac{(1 - \exp[-TR/T_{1,fat}])FF_{TR}}{(1 - \exp[-TR/T_{1,fat}])FF_{TR} + (1 - \exp[-TR/T_{1,water}])FF_{TR}} \quad (\text{A.4})$$

¹Or $TR \gg T_1$, for practical purposes.

Bibliography

- [1] E. Lebovics and J. Rubin, “Non-alcoholic fatty liver disease (NAFLD): why you should care, when you should worry, what you should do,” *Diabetes Metab Res Rev*, vol. 27, pp. 419–424, 2011.
- [2] S. Caldwell, Y. Ikura, D. Dias, K. Isomoto, A. Yabu, C. Moskaluk, P. Pramoojago, W. Simmons, H. Scruggs, N. Rosenbaum, T. Wilkinson, P. Toms, C. Argo, A. Al-Osaimi, and J. Redick, “Hepatocellular ballooning in NASH,” *J Hepatol*, vol. 53, pp. 719–723, 2010.
- [3] P. Angulo, “GI Epidemiology: nonalcoholic fatty liver disease,” *Aliment Pharmacol Ther*, vol. 25, pp. 883–889, 2007.
- [4] G. Farrell, A. McCullough, and C. Day, *Non-Alcoholic Fatty Liver Disease: A Practical Guide*. Wiley, 2013.
- [5] T. Okanoue, A. Umemura, K. Yasui, and Y. Itoh, “Nonalcoholic fatty liver disease and nonalcoholic steatohepatitis in Japan,” *J Gastroenterol Hepatol*, vol. 26, pp. 153–162, 2011.
- [6] M. Rinella, “Nonalcoholic fatty liver disease: A systematic review,” *JAMA*, vol. 313, pp. 2263–2273, 2015.
- [7] D. Kleiner, E. Brunt, M. Van Natta, C. Behling, M. Contos, O. Cummings, L. Ferrell, Y. Liu, M. Torbenson, A. Unalp-Arida, M. Yeh, A. McCullough, and A. Sanyal, “Design and validation of a histological scoring system for nonalcoholic fatty liver disease,” *Hepatology*, vol. 41, pp. 1313–1321, 2005.
- [8] J. Chen, J. Talwalkar, M. Yin, K. Glaser, S. Sanderson, and R. Ehman, “Early detection of nonalcoholic steatohepatitis in patients with nonalcoholic fatty liver disease by using MR elastography,” *Radiology*, vol. 259, pp. 749–756, 2011.
- [9] L. Adams, S. Sanderson, K. Lindor, and P. Angulo, “The histological course of nonalcoholic fatty liver disease: a longitudinal study of 103 patients with sequential liver biopsies,” *Hepatology*, vol. 42, pp. 132–138, 2005.
- [10] P. Angulo, “Nonalcoholic fatty liver disease,” *N Engl J Med*, vol. 346, pp. 1221–1231, 2002.
- [11] O. Hamer, D. Aguirre, G. Casola, J. Lavine, M. Woenckhaus, and C. Sirlin, “Fatty liver: Imaging patterns and pitfalls,” *RadioGraphics*, pp. 1637–1653, 2006.

- [12] V. Ratziu, F. Charlotte, A. Heurtier, S. Gombert, P. Giral, E. Bruckert, A. Grimaldi, F. Capron, and T. Poynard, "Sampling variability of liver biopsy in nonalcoholic fatty liver disease," *Gastroenterology*, vol. 128, pp. 1898–1906, 2005.
- [13] S. Starr and D. Raines, "Cirrhosis: Diagnosis, management, and prevention," *Am Fam Physician*, vol. 85, pp. 1353–1359, 2011.
- [14] S. Venkatesh and R. Ehman, "Magnetic resonance elastography of liver," *Magn Reson Imaging Clin N Am*, vol. 22, pp. 433–446, 2014.
- [15] T. Lefebvre, G. Gilbert, C. Wartelle-Bladou, G. Sebastiani, H. Castel, B. Nguyen, D. Olivie, and A. Tang, "Intravoxel incoherent motion diffusion-weighted MRI for assessing necroinflammation in patients with chronic liver disease," in *Conf Proc ISMRM Annual Meeting*, 2018:0521.
- [16] C. Li, X. Luo, W. Dou, Y. Peng, J. Wu, and J. Ye, "Stretched exponential diffusion-weighted imaging model in quantitative diagnosis of nonalcoholic fatty liver disease: a rabbit model study," in *Conf Proc ISMRM Annual Meeting*, 2019:1781.
- [17] X. Luo, C. Li, W. Dou, Y. Peng, and J. Ye, "Diffusion kurtosis imaging in quantitative diagnosis of nonalcoholic fatty liver disease: a rabbit model study," in *Conf Proc ISMRM Annual Meeting*, 2019:0354.
- [18] A. Gharib, M. Han, E. Meissner, D. Kleiner, X. Zhao, M. McLaughlin, L. Matthews, B. Rizvi, K. Abd-Elmoniem, R. Sinkus, E. Levy, C. Koh, R. Myers, G. Subramanian, S. Kottlil, T. Heller, J. Kovacs, and C. Morse, "Magnetic resonance elastography shear wave velocity correlates with liver fibrosis and hepatic venous pressure gradient in adults with advanced liver disease," *Biomed Res Int*, vol. 2017, p. 2067479, 2017.
- [19] S. Serai and T. Trout, "Can MR elastography be used to measure liver stiffness in patients with iron overload," *Abdom Radiol*, vol. 44, pp. 104–109, 2019.
- [20] L. Britton, V. Subramaniam, and D. Crawford, "Iron and non-alcoholic fatty liver disease," *World J Gastroenterol*, vol. 22, pp. 8112–8122, 2016.
- [21] S. Serai, J. Dillman, and A. Trout, "Spin-echo echo-planar imaging MR elastography versus gradient-echo MR elastography for assessment of liver stiffness in children and young adults suspected of having liver disease," *Radiology*, vol. 282, pp. 761–770, 2017.
- [22] A. Elizondo, J. Araya, R. Rodrigo, J. Poniachik, A. Csendes, F. Maluenda, J. Diaz, C. Signorini, C. Sgherri, M. Comporti, and L. Videla, "Polyunsaturated fatty acid pattern in liver and erythrocyte phospholipids from obese patients," *Obesity*, vol. 15, pp. 24–31, 2007.

- [23] N. Johnson, D. W. Walton, T. Sachinwalla, C. H. Thompson, K. Smith, P. Ruell, S. Stannard, and J. George, “Noninvasive assessment of hepatic lipid composition: Advancing understanding and management of fatty liver disorders,” *Hepatology*, vol. 47, pp. 1513–1523, May 2008.
- [24] J. van Werven, T. Schreuder, A. Nederveen, C. Lavini, P. Jansen, and J. Stoker, “Hepatic unsaturated fatty acids in patients with non-alcoholic fatty liver disease assessed by 3.0 T MR spectroscopy,” *Eur Radiol*, vol. 75, pp. e102–e107, 2010.
- [25] L. Videla, R. Rodrigo, J. Araya, and J. Poniachik, “Oxidative stress and depletion of hepatic long-chain polyunsaturated fatty acids may contribute to nonalcoholic fatty liver disease,” *Free Radic Biol Med*, vol. 37, pp. 1499–1507, 2004.
- [26] E. Scorletti and C. Byrne, “Omega-3 fatty acids, hepatic lipid metabolism, and nonalcoholic fatty liver disease,” *Annu Rev Nutr*, vol. 33, pp. 231–248, 2013.
- [27] J. Yang, M. Fernandez-Galilea, L. Martinez-Fernandez, P. Gonzalez-Muniesa, A. Perez-Chavez, J. Martinez, and M. Moreno-Aliaga, “Oxidative stress and non-alcoholic fatty liver disease: Effects of omega-3 fatty acid supplementation,” *Nutrients*, vol. 11, p. 872, 2019.
- [28] I. Corbin, E. Furth, S. Pickup, E. Siegelman, and E. Delikatny, “*In vivo* assessment of hepatic triglycerides in murine non-alcoholic fatty liver disease using magnetic resonance spectroscopy,” *Biochim Biophys Acta*, vol. 1791, pp. 757–763, 2009.
- [29] Z. Li, M. Berk, T. McIntyre, and A. Feldstein, “Hepatic lipid partitioning and liver damage in nonalcoholic fatty liver disease: Role of Stearoyl-CoA Desaturase,” *Journal of Biological Chemistry*, vol. 284, pp. 5637–5644, 2009.
- [30] M. Pickens, H. Ogata, R. Soon, J. Grenert, , and J. Maher, “Dietary fructose exacerbates hepatocellular injury when incorporated into a methionine-choline-deficient diet,” *Liver International*, vol. 30, pp. 1229–1239, 2010.
- [31] M. Stankovic, D. Mladenovic, I. Duricic, S. Sobajic, J. Timic, B. Jorgacevic, V. Aleksic, D. Vucevic, R. Jesic-Vukicevic, and T. Radosavljevica, “Time-dependent changes and association between liver free fatty acids, serum lipid profile and histological features in mice model of nonalcoholic fatty liver disease,” *Arch Med Res*, vol. 45, pp. 116–124, 2014.
- [32] Y. Takahashi, Y. Soejima, and T. Fukusato, “Animal models of nonalcoholic fatty liver disease/nonalcoholic steatohepatitis,” *World J Gastroenterol*, vol. 18, pp. 2300–2308, 2012.
- [33] M. Van Herck, L. Vonghia, and S. Francque, “Animal models of nonalcoholic fatty liver disease: A starter’s guide,” *Nutrients*, vol. 9, 2017.

- [34] S. Keevil, "Spatial localization in nuclear magnetic resonance spectroscopy," *Phys Med Biol*, vol. 51, pp. R579–R636, 2006.
- [35] E. Brunt, C. Janney, A. Di Bisceglie, B. Neuschwander-Tetri, and B. Bacon, "Nonalcoholic steatohepatitis: A proposal for grading and staging the histological lesions," *Am J Gastroenterol*, vol. 94, pp. 2467–2474, 1999.
- [36] S. Chitturi, M. Weltman, G. Farrell, D. McDonald, C. Liddle, D. Samarasinghe, R. Lin, S. Abeygunasekera, and J. George, "HFE mutations, hepatic iron, and fibrosis: ethnic-specific association of NASH with C282Y but not with fibrotic severity," *Hepatology*, vol. 36, pp. 142–149, 2002.
- [37] S. Hu, M. Lustig, A. Chen, J. Crane, A. Kerr, D. Kelley, R. Hurd, J. Kurhanewicz, S. Nelson, J. Pauly, and D. Vigneron, "Compressed sensing for resolution enhancement of hyperpolarized ^{13}C flyback 3D-MRSI," *J Magn Reson*, vol. 192, pp. 258–264, March 2008.
- [38] T. Kampf, A. Fischer, T. Basse-Lusebrink, G. Ladewig, F. Breuer, S. G. P. Jakob, and W. Bauer, "Application of compressed sensing to in vivo 3D ^{19}F CSI," *J Magn Reson*, vol. 207, pp. 262–273, 2010.
- [39] S. Geethanath, H. Baek, S. Ganji, Y. Ding, E. Maher, R. Sims, C. Choi, M. Lewis, and V. Kodibagkar, "Compressive sensing could accelerate ^1H MR metabolic imaging in the clinic," *Radiology*, vol. 262, pp. 985–944, 2012.
- [40] L. J., "On the theory of the magnetic influence on spectra; and on the radiation from moving ions," *Phil Mag*, vol. 44, pp. 503–512, 1987.
- [41] J. Keeler, *Understanding NMR spectroscopy*. Wiley, 2010.
- [42] G. Galiana, "Spatial encoding & k-space," in *Conf Proc ISMRM Annual Meeting*, 2019.
- [43] M. Lustig, D. Donoho, J. Santos, and J. Pauly, "Compressed sensing MRI," *IEEE Signal Process Mag*, vol. 25, pp. 72–82, March 2008.
- [44] U. Klose, "Measurement sequences for single voxel proton MR spectroscopy," *Eur J Radiol*, vol. 67, pp. 194–201, 2008.
- [45] D. Yeung, J. Griffith, G. Antonio, F. Lee, J. Woo, and P. Leung, "Osteoporosis is associated with increased marrow fat content and decreased marrow fat unsaturation: A proton MR spectroscopy study," *J Magn Reson Imaging*, vol. 22, pp. 279–285, 2005.
- [46] M. Guillen and A. Ruiz, "Rapid simultaneous determination by proton NMR of unsaturation and composition of acyl groups in vegetable oils," *Eur J Lipid Sci Technol*, vol. 105, pp. 688–696, 2003.

- [47] G. Hamilton, T. Yokoo, M. Bydder, T. Cruite, M. Schroeder, C. Sirlin, and M. Middleton, “In vivo characterization of the liver fat ^1H MR spectrum,” *NMR Biomed*, vol. 24, pp. 784–790, 2011.
- [48] J. Berglund, H. Ahlström, and J. Kullberg, “Model-based mapping of fat unsaturation and chain length by chemical shift imaging: Phantom validation and in vivo feasibility,” *Magn Reson Med*, vol. 38, pp. 1815–1827, 2012.
- [49] M. Bernstein, K. King, and X. Zhou, *Handbook of MRI Pulse Sequences*. Elsevier, 2004.
- [50] C. Moonen, M. von Kienlin, P. van Zijl, J. Cohen, J. Gillen, P. Daly, and G. Wolf, “Comparison of single-shot localization methods (STEAM and PRESS) for *in vivo* proton NMR spectroscopy,” *NMR Biomed*, vol. 2, pp. 201–208, 1989.
- [51] F. Traber, W. Block, R. Lamerichs, J. Gieseke, and H. Schild, “ ^1h metabolite relaxation times at 3.0 Tesla: Measurements of T1 and T2 values in normal brain and determination of regional differences in transverse relaxation,” *J Magn Reson Imaging*, vol. 19, pp. 537–545, 2004.
- [52] K. Pruessmann, M. Weiger, M. Scheidegger, and P. Boesiger, “SENSE: sensitivity encoding for fast MRI,” *Magn Reson Med*, vol. 42, pp. 952–962, 1999.
- [53] M. Griswold, P. Jakob, R. Heidemann, M. Nittka, V. Jellus, J. Wang, B. Kiefer, and A. Haase, “Generalized autocalibrating partially parallel acquisitions (GRAPPA),” *Magn Reson Med*, vol. 47, pp. 1202–1210, 2002.
- [54] H. J. D. Franson, and N. Seiberlich, “Recent advances in parallel imaging for MRI,” *Prog Nucl Magn Reson Spectrosc*, vol. 2017, pp. 71–95, 2017.
- [55] M. Davenport, M. Duarte, Y. Eldar, and G. Kutyniok, “Introduction to compressed sensing,” in *Compressed Sensing: Theory and Applications* (Y. Eldar and G. Kutyniok, eds.), Cambridge University Press, 2012.
- [56] M. Lustig, D. Donoho, and J. Pauly, “Sparse MRI: The application of compressed sensing for rapid MR imaging,” *Magn Res Med*, vol. 58, pp. 1182–1195, 2007.
- [57] S. Lingala and M. Jacob, “Blind compressive sensing dynamic MRI,” *IEEE T Med Imaging*, vol. 32, pp. 1132–1145, 2013.
- [58] T. Akasaka, K. Fujimoto, T. Yamamoto, T. Okada, Y. Fushumi, A. Yamamoto, T. Tanaka, and K. Togashi, “Optimization of regularization parameters in compressed sensing of magnetic resonance angiography: Can statistical image metrics mimic radiologists’ perception?,” *PLoS one*, vol. 11, 2015.
- [59] S. Bhave, S. Lingala, and M. Jacob, “A variable splitting based algorithm for fast multi-coil blind compressed sensing MRI reconstruction,” in *Conf Proc IEEE Eng Med Biol Soc*, pp. 2400–2403, 2014.

- [60] L. Vanhamme, T. Sundin, P. Van Hecke, and S. Van Huffel, "MR spectroscopy quantitation: a review of time domain methods," *NMR in Biomed*, vol. 14, pp. 233–246, 2001.
- [61] S. Mierisova and M. Ala-Korpela, "MR spectroscopy quantitation: a review of frequency domain methods," *NMR in Biomed*, vol. 14, pp. 247–259, 2001.
- [62] T. Laudadio, N. Mastronardi, L. Vanhamme, P. Van Hecke, and S. Van Huffel, "Improved Lanczos algorithms for blackbox MRS data quantitation," *J Magn Reson*, vol. 157, pp. 292–297, 2002.
- [63] R. de Beer, D. van Ormondt, and W. Pijnappel, "Quantification of 1D and 2D magnetic resonance time domain signals," *Pure Appl Chem*, vol. 64, pp. 815–823, 1992.
- [64] J. Liu and D. Saloner, "Accelerated MRI with circular cartesian undersampling (CIRCUS): a variable density cartesian sampling strategy for compressed sensing and parallel imaging," *Quant Imag Med Surg*, vol. 4, pp. 57–67, 2014.
- [65] S. Winkelmann, T. Schaeffter, T. Koehler, H. Eggers, and O. Doessel, "An optimal radial profile order based on the golden ratio for time-resolved MRI," *IEEE T Med Imaging*, vol. 26, pp. 68–76, 2007.
- [66] J. Rioux, M. Hewlett, C. Davis, C. Bowen, K. Brewer, S. Clarke, and S. Beyea, "Quantification of fatty acid composition with free-breathing MR spectroscopic imaging and compressed sensing," *Submitted to NMR Biomed (Manuscript NBM-19-0107)*, 2019.
- [67] M. Bydder, G. Hamilton, L. de Rochefort, A. Desai, E. Heba, R. Loomba, J. Schwimmer, N. Szevenyi, and C. Sirlin, "Sources of systematic error in proton density fat fraction (PDFFF) quantification in the liver evaluated from magnitude images with different numbers of echoes," *NMR Biomed*, vol. 31, p. e3843, 2018.
- [68] P. Chi, W. Dou, and J. Constans, "A post-processing approach of HLSVD used for automatic quantitative analysis of multi-voxel magnetic resonance spectra," in *Conf Proc IEEE Int Conf Bioinform Biomed*, pp. 1–4, 2011.
- [69] S. Reeder, I. Cruite, G. Hamilton, and C. Sirlin, "Quantitative assessment of liver fat with magnetic resonance imaging and spectroscopy," *J Magn Reson Imaging*, vol. 34, pp. 729–749, 2011.
- [70] J. Ren, I. Dimitrov, A. Sherry, and C. Malloy, "Composition of adipose tissue and marrow fat in humans by ^1H NMR at 7 Tesla," *J Lipid Res*, vol. 49, pp. 2055–2062, 2008.

- [71] E. Hall, M. Stephenson, P. D, and P. Morris, "Methodology for improved detection of low concentration metabolites in MRS: Optimised combination of signals from multi-element coil arrays," *Neuroimage*, vol. 86, pp. 35–42, 2014.
- [72] M. Brown, "Time-domain combination of MR spectroscopy data acquired using phased-array coils," *Magn Reson Med*, vol. 52, pp. 1207–1213, 2004.
- [73] N. Martini, M. Santarelli, G. Giovannetti, M. Milanesi, D. De Marchi, and L. Positano, V and Landini, "Noise correlations and SNR in phased-array MRS," *NMR Biomed*, vol. 23, pp. 66–73, 2009.
- [74] M. Uecker, F. Ong, J. Tamir, D. Bahri, P. Virtue, J. Cheng, T. Zhang, and M. Lustig, "Berkeley advanced reconstruction toolbox," in *Conf Proc ISMRM Annual Meeting*, 2015:2486.
- [75] E. Cabanes, S. Confort-Gouny, Y. Le Fur, G. Simond, and P. Cozzone, "Optimization of residual water signal removal by HLSVD on simulated short echo time proton MR spectra of the human brain," *J Magn Reson*, vol. 150, pp. 116–125, 1999.
- [76] I. Marshall, J. Higinbotham, S. Bruce, and A. Freise, "Use of Voigt lineshape for quantification of in vivo ^1H spectra," *Magn Res Med*, vol. 37, pp. 651–657, 1997.
- [77] J. de Winter, "Using the Student's t-test with extremely small sample sizes," *Pract Assess Res Eval*, vol. 18, 2013.
- [78] A. Skoch, P. Jiru, and J. Bunke, "Spectroscopic imaging: basic principles," *Eur J Radiol*, vol. 67, pp. 230–239, 2008.
- [79] R. Song, A. Tipirneni, P. Johnson, R. Loeffler, and C. Hillenbrand, "Evaluation of respiratory liver and kidney movements for MRI navigator gating," *J Magn Reson Imaging*, vol. 33, pp. 143–148, 2011.
- [80] K. Yamaguchi, L. Yang, S. McCall, J. Huang, X. Yu, S. Pandey, S. Bhanot, B. Monia, Y. Li, and A. Diehl, "Inhibiting triglyceride synthesis improves hepatic steatosis but exacerbates liver damage and fibrosis in obese mice with non-alcoholic steatohepatitis," *Hepatology*, vol. 45, pp. 1366–1374, 2007.
- [81] E. Haacke, R. Brown, M. Thompson, and R. Venkatesan, *Magnetic Resonance Imaging: Physical Principles and Sequence Design*. Wiley, 1999.